Seismic Imaging of Fault Zones

A synthetic workflow to study the impact of faults on seismic images

by

Charlotte Delphine Botter

Thesis submitted in fulfilment of
the requirements for degree of
PHILOSOPHIAE DOCTOR
(PhD)

Faculty of Science and Technology

Department of Petroleum Engineering

2016

University of Stavanger
N-4036 Stavanger
NORWAY
www.uis.no

ISBN: 978-82-7644-648-7

ISSN: 1890-1387

PhD thesis no. 293

Preface

This thesis is submitted in fulfilment of the requirements for the degree of *Philosophiae Doctor* (PhD) at the University of Stavanger (UiS), Norway. The work was carried out between January 2012 and March 2016 while I was enrolled in a PhD program in the Department of Petroleum Engineering, Faculty of Science and Technology, at UiS. My PhD was funded by the Research Council of Norway through the project "Seismic Imaging of Fault Zones" (NFR-PETROMAKS project no. 210425/E30). My main supervisor is Dr. Nestor Cardozo (UiS) and my co-supervisors are Drs. Isabelle Lecomte (NORSAR), Stuart Hardy (ICREA and University of Barcelona) and Alejandro Escalona (UiS). Collaboration was also established with Drs. Gaynor Paton (ffA Geosciences) and Atle Rotevatn (University of Bergen). One year of my PhD was devoted to teaching "Well logging" at the bachelor level for three large classes in the Department of Petroleum Engineering (UiS). These teaching duties were funded by the Department of Petroleum Engineering. During my PhD, I have been a representative of the PhD candidates at UiS through the UiS Doctoral Community (UiSDC), as a board member in 2013 and as president in 2014. I also have organised the Department PhD seminar since 2014.

This research has resulted in one published article and two manuscripts submitted a couple of months before the dissertation's submission. I have presented my work at several conferences. This thesis is structured as scientific paper-based and consists of two chapters. The first chapter introduces the general problem, motivation, objectives, methodology, results, and conclusions. The second chapter is the collection of the three papers forming the main body of the thesis. The appendices provide supplementary material and conference abstracts.

Charlotte Botter
Stavanger, March 18th 2016

Abstract

Although typically interpreted as 2D surfaces, faults are 3D narrow zones of highly and heterogeneously strained rocks with petrophysical properties differing from the host rock. Fault zones have been extensively studied in outcrop, but in the subsurface they have barely been explored, mainly because they have low signal-to-noise ratio on seismic, are often at the limit of seismic resolution, and are rarely drilled and cored. To evaluate the potential of seismic data for imaging fault structure and properties, we introduce a forward seismic modelling workflow consisting of four steps: fault modelling, elastic properties definition, seismic modelling, and seismic interpretation. This workflow is applied to normal faulting in siliciclastic sequences.

In the first paper, we implement the workflow using a methodology consisting of a discrete element model (DEM) of faulting, empirical relations to modify the initial acoustic properties of the model based on volumetric strain, a ray-based algorithm simulating pre-stack depth migration (PSDM) results, and interpretation and correlation of the seismic and input properties. This methodology is applied in 2D to a large-scale (100 m displacement) normal fault in a sandstone-shale sequence at reservoir depths, for two DEM particle-size resolutions, one finer than the other. Both simulations produce realistic fault geometries and strain fields, with the finer particle-size model displaying narrower fault zones and fault linkage at later stages. Seismic imaging and resolution of these two models are highly influenced by illumination direction and wave frequency. At high wave frequencies, there is a direct correlation between seismic amplitude variations and the input acoustic properties after faulting.

The second paper uses the same methodology, but in 3D for a normal fault with large displacement in a sandstone-shale sequence for two cases, one with constant fault displacement and another with linearly variable displacement along strike. High frequencies on seismic images show the impact of the fault on the offset and distortion of the reflectors. In the variable fault-slip model, the fault has less impact as the displacement decreases, and the fault tipline can be interpreted. We extract fault geobodies using an adapted attribute-based workflow. The geobody for the constant fault displacement model

corresponds to an inner high-deformation area within the fault zone, while in the variable fault-slip model the geobody captures better the entire fault zone.

Finally in the third paper, we illustrate the workflow using an outcrop-based simulated fluid flow model from the Delicate Arch Ramp (Utah), to study the impact of relay ramps and their fluid composition on seismic data. Changes in porosity in the fault damage zones are visible in the oil-saturated model at the beginning of the simulation, whereas the water-oil contacts have stronger impact on seismic at later stages. We extract volumes corresponding to the two faults and the relay ramp from the three seismic cubes with an adapted tuning of the attribute-based workflow. By varying input and imaging parameters, we also show reservoir and acquisition conditions that affect the resolution of the relay ramp seismic image.

Through this interdisciplinary research, we show the potential of seismic data for specific fault characterisation, as well as the tuning of acquisition and processing parameters, and interpretation routines required to map faults and their associated deformation. This research has major implications for hydrocarbon exploration and production, storage of subsurface waste, and hydrogeological and geothermal systems.

Acknowledgments

I would like to express my greatest gratitude to my supervisor Dr Nestor Cardozo for all the help, guidance and support during the four years of my PhD. Thank you for always having time to meet, discuss and review my work. Also, I really appreciate the social environment you created, particularly with dinners at your place with your wife Ann Elisabeth Laksfoss Hansen. Thanks to all my co-supervisors Drs Isabelle Lecomte, Stuart Hardy and Alejandro Escalona, and co-authors Drs Gaynor Paton and Atle Rotevatn, for the many discussions, feedback and help that guided me through my research. You have been a great source of inspiration and intellectual stimulation.

I would like to thank all my colleagues at the Department of Petroleum Engineering, and mainly everyone from the Petroleum Geoscience Engineering (PGE) group, for providing a very good work environment. Special thanks to Andreas Habel for always providing quick solutions to IT problems, to Lisa Jean Bingham for being a great coordinator within the PGE, and to Jim Brown for proofreading my thesis. Since I started my PhD, I have interacted with many people from other groups who were enthusiastic to learn about my research, in particular Drs Skule Strand, Aly Hamouda and Merete Vadla Madland. Special thanks to my dear friends from the PGE group, with whom I shared an office at some point, Thanusha Naidoo, Sanne Lorentzen, Wenxia Wang and Dora Marín, for the daily interaction and debates, and to all the PhD candidates at the department for all the lunches and discussions. Thanks to all the members of the UiS Doctoral Community (UiSDC) who became my close friends during my two years on the board, Drs Izaskun Muruzábal-Lecumberri and Kristian Thorsen, Martin Vogt Juhler, Aya Kusumawardhani and Hanne Egenæs Staurseth.

Thanks to all my friends who made Stavanger a good place to live. And last but not least, thanks to my parents Joan Younès and Marc Botter, to my sisters Margaux, Rafaëlle, Marion and Alexia, to my grand-parents Liliane Younès and René Botter, to Sylvie Botter and to the rest of my family, for all the love and support.

Table of contents

List of Figures

List of Tables

List of Papers

Paper 1:

From mechanical modeling to seismic imaging of faults: a synthetic workflow to study the impact of faults on seismic.
Botter, Charlotte; Cardozo, Nestor; Hardy, Stuart; Lecomte, Isabelle & Escalona, Alejandro
2014, *Marine and Petroleum Geology*, **57**, 187-207
doi: http://dx.doi.org/10.1016/j.marpetgeo.2014.05.013.

Paper 2:

Seismic characterisation of fault damage in 3D using mechanical and seismic modelling.
Botter, Charlotte; Cardozo, Nestor; Hardy, Stuart; Lecomte, Isabelle; Paton, Gaynor & Escalona, Alejandro
Submitted to Marine and Petroleum Geology, January 2016.
(First submitted in May 2015 to AAPG bulletin)

Paper 3:

The impact of faulting and fluid flow on seismic images of a relay ramp.
Botter, Charlotte; Cardozo, Nestor; Lecomte, Isabelle; Rotevatn, Atle & Paton, Gaynor
Submitted to Petroleum Geoscience, thematic set on fault and top seals, February 2016.

Conference extended abstracts

Extended abstract 1:

Botter, Charlotte; Cardozo, Nestor; Hardy, Stuart; Lecomte, Isabelle & Escalona, Alejandro
Mechanical modelling and seismic imaging of fault zones.
*EAGE Fault and Top Seals Conference, Montpellier **2012**; 2012/10/01-03.*
Accepted for oral presentation

Extended abstract 2:

Botter, Charlotte; Cardozo, Nestor; Hardy, Stuart; Lecomte, Isabelle; Escalona, Alejandro; Cooke, Nicholas & Paton, Gaynor
From Geomechanical Modelling to Seismic Imaging of 3D Faults.
*Conference proceedings. 76th EAGE Conference & Exhibition. EAGE **2014***
ISBN 978-90-73834-89-7.
Accepted for oral presentation

Extended abstract 3:

Botter, Charlotte; Cardozo, Nestor; Lecomte, Isabelle; Rotevatn, Atle & Paton, Gaynor
The effect of fluid flow in relay ramps on seismic images.
*EAGE Fault and Top Seals Conference, Almerìa **2015**; 2015/09/20-24.*
Accepted for oral presentation
Received Award for Best Young Presenter
Information published on *geoforskning.no* and in two paper journals: *GEO Energy & Ressurser 18. Årgang nr 7, 2015* and *First Break Volume 3, Issue 12, December 2015*

Conference oral presentations

Lofotenseminaret i petroleumsgeofysikk 2012:

Botter, Charlotte; Cardozo, Nestor; Hardy, Stuart; Lecomte, Isabelle & Escalona, Alejandro

Mechanical modelling and seismic imaging of fault zones.

*Lofotenseminaret i petroleumsgeofysikk **2012**; 2012/08/15-17*

Tectonic Studies Group Annual Conference 2014:

Cardozo, Nestor; Botter, Charlotte; Hardy, Stuart; Lecomte, Isabelle; Escalona, Alejandro.

From mechanical modelling to seismic imaging of faults.

*Tectonic Studies Group-Annual Conference **2014**; 2014/01/06-08*

AAPG International Conference & Exhibition 2014:

Botter, Charlotte; Cardozo, Nestor; Hardy, Stuart; Lecomte, Isabelle; Escalona, Alejandro ; Cooke, Nicholas & Paton, Gaynor

From geomechanical modelling to seismic imaging of 3D faults.

*AAPG International Conference & Exhibition **2014**; 2014/09/14-17*

NGF Vinterkonferansen 2015:

Botter, Charlotte; Cardozo, Nestor; Hardy, Stuart; Lecomte, Isabelle; Escalona, Alejandro & Paton, Gaynor

From geomechanical modelling to seismic imaging of 3D faults.

*NGF Vinterkonferansen **2015**; 2015/01/12-14*

Petroleum Research School of Norway (NFiP) PhD Seminar 2015:

Botter, Charlotte; Cardozo, Nestor; Lecomte, Isabelle; Rotevatn, Atle & Paton, Gaynor

The effect of fluid flow in relay ramps on seismic images.

*Annual (NFiP) PhD Seminar November 26th, **2015**.*

Force Geophysical Lunch & Learn Seminar 2016:

Botter, Charlotte; Cardozo, Nestor; Lecomte, Isabelle; Hardy, Stuart; Paton, Gaynor; Escalona, Alejandro & Rotevatn, Atle

Seismic imaging of fault zones.

*Geophysical Lunch & Learn seminar, FORCE – March 3rd, **2016**.*

Abbreviations

FEM – Finite-element method

FD – Finite-difference

DEM – Discrete element method

PSDM – Pre-stack depth migration

PSF – Point spread function

V_P – P-wave velocity

V_S – Shear-wave velocity

RMS – Root mean square

Chapter 1

Introduction

1 Introduction

Faults play a key role in reservoirs by compartmentalising them and restricting or enhancing fluid flow. Faults are commonly interpreted as 2D surfaces on seismic data and they are represented as such in reservoir models. In reality though, faults are narrow zones or volumes of highly and heterogeneously strained rocks, with petrophysical properties differing from those of the host rock. Internal fault structure varies throughout reservoirs (Fisher and Jolley, 2007; Jolley et al., 2007; Faulkner et al., 2010 and references therein). Fault structure and distribution of fault properties depend on factors such as host lithology and stratigraphy (Davatzes and Aydin, 2005; Eichhubl et al., 2005; Bastesen and Braathen, 2010), depth of burial at time of faulting (Fisher and Knipe, 2001), initial fault array geometry and structural evolution (Childs et al., 2009), and diagenesis (Solum et al., 2010). Faults deform the surrounding rocks, producing fault-related deformation. The core of the fault accommodates most of the displacement (Caine et al., 1996) and may display one or several slip surfaces, clay smears, lenses, fractures, etc. While the internal structure of the fault core is hardly predictable (e.g. Foxford et al., 1998), the surrounding fault-related deformation decreases more or less in a systematic manner from a maximum at the centre of the fault to zero at the fault damage zone boundaries (e.g. Rotevatn et al., 2007; Brogi, 2008; Schueller et al., 2013). Figure 1a illustrates the complex geometry, internal structure, and related deformation of a fault zone in a siliciclastic sequence of Western Sinai, Egypt.

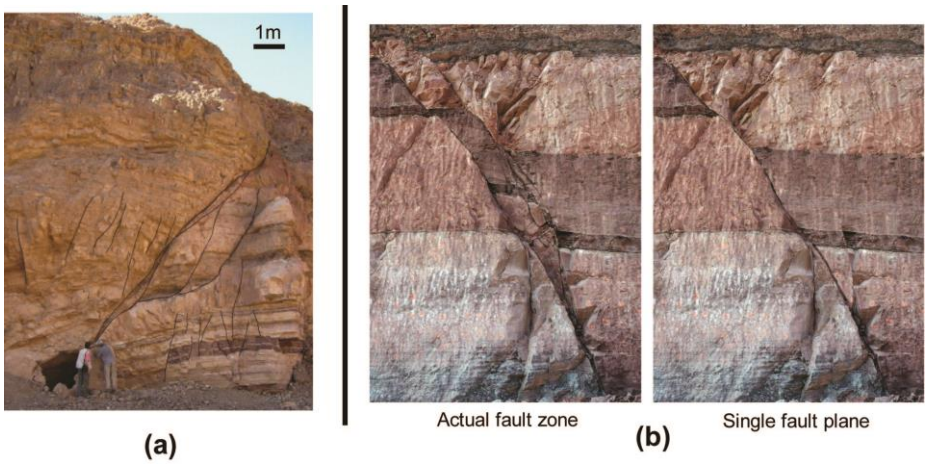

Figure 1: *Examples of fault zones in outcrop. (a) Fault zone in Cambrian sandstones of Western Sinai, Egypt (Photo: Courtesy of Nestor Cardozo). (b) Fault zone in Jurassic sandstones of Utah, USA. Actual fault zone (left) and modified picture with a single fault plane (right). Part b can be representative of a large range of scales going from m to km (pictures are courtesy of Haakon Fossen, http://folk.uib.no/nglhe).*

In addition to influencing reservoir compartmentalisation, internal fault architecture and properties have a strong impact on fluid flow. Figure 1b illustrates the difference between an actual fault in outcrop (Figure 1b left) and its standard 2D seismic interpretation and reservoir model representation (Figure 1b right). The 3D distribution of lithologies and properties inside the fault zone is crucial for defining reservoir connectivity between the hanging wall and footwall. However, this information is lost in the simplified 2D representation. 3D fault structure and internal petrophysical properties are primary controls on fluid flow in faulted reservoirs, determining fault sealing over geologic and production time scales (Faulkner et al., 2010; Pei et al., 2015 and references therein). Several models of fault sealing have been established in order to understand the impact of faults on fluid flow in reservoirs (Manzocchi et al., 2010; Pei et al., 2015). These studies look at fault architecture, lithology and properties within the faults. However, each of these studies focuses on restricted scale ranges, which restrain their use for scaling purposes, i.e., upscaling or downscaling (Pei et al., 2015). A multi-scale approach is crucial to an understanding of the physical and chemical processes

operating in faults. Most of the information we have about faults comes from outcrop studies in 2D (e.g. Eichhubl et al., 2005) and 3D (e.g. Childs et al., 1996; Foxford et al., 1998). However, outcrop data come mostly from faults with small-scale displacement of cm to Dm (Childs et al., 2009) and are limited to specific combinations of lithology and fault displacements (e.g. Wibberley et al., 2008). The relationships derived from this limited dataset are not sufficient to predict fault variability in 3D at larger reservoir scales (Manzocchi et al., 2010; Pei et al., 2015).

Seismic data provide the main way to evaluate faults with hundreds of metres to kilometres of displacement in the subsurface. Well data across faults (e.g. Aarland and Skjerven, 1998) are very rare. Internal fault structure and properties are at the limit of, if not under, seismic resolution. Indeed, for typical depths of investigation of 2-4 km, seismic will hardly capture vertical features less than 12-25 m. The horizontal resolution, which is crucial for evaluating 3D fault architecture, is highly dependent on many factors, including noise. The horizontal uncertainties are higher than the vertical ones, often by a factor of 2 (Sheriff and Geldart, 1995). Thin beds, sub-seismic features and fault zones can therefore interfere and not be well represented in seismic images. Moreover, when the seismic data are handed to the geological interpreter, several processing steps have been applied that might influence the seismic image. Figure 2 shows that within the limits of seismic data resolution, there is room for alternative interpretations, which result in different assessments of reservoir connectivity (Figure 2a). Faulting induces lateral changes in reflector continuity and seismic amplitudes. These poorly illuminated areas are illustrated in Figure 2b, with a fault zone (in green) around the interpreted fault plane (Figure 2b left). A close up shows the complex seismic response of the fault, making difficult to interpret it as a surface (Figure 2b right). Dutzer et al. (2010) and Iacopini and Butler (2011) have approached this problem by defining, respectively, a seismic fault distortion zone and a disturbance geobody, roughly corresponding to the fault damage zone.

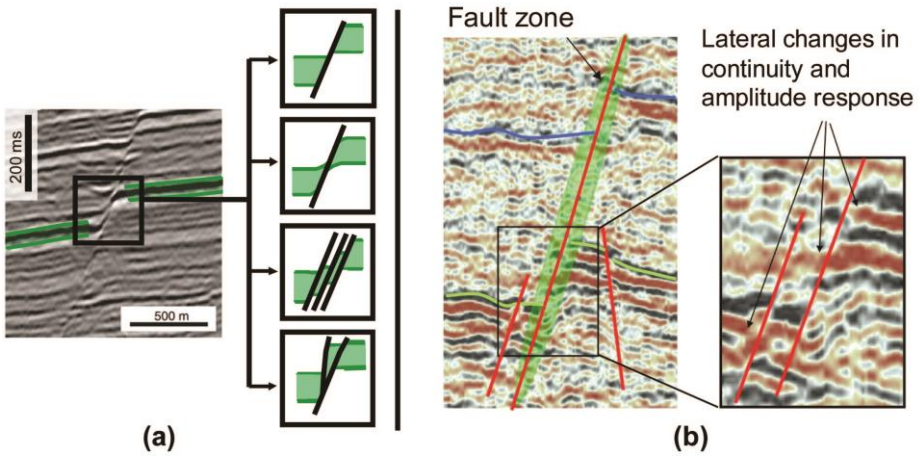

Figure 2: *Examples of fault zones in seismic (a) Seismic section of a fault zone with four possible interpretations affecting the assessment of reservoir connectivity (modified from Wibberley et al., 2008). (b) Interpretation of a fault zone on a seismic section and its lateral variation in amplitude response (modified from Nicolaisen, 2009).*

2 State of the art regarding seismic characterisation of faults

2.1 Characterisation of faults in seismic

Despite the importance of 3D internal fault structure for assessing reservoir connectivity, seismic interpretation hardly takes it into account. Most seismic interpretation studies target the recognition of fault networks and their organisation (e.g. Chehrazi et al., 2013; Zhou et al., 2012). These methods, which are helpful to the building of geomodels based on faults as surfaces, are not adequate for capturing the complexity of fault architecture and associated properties. There are not many examples in the literature examining the potential of seismic data to elucidate fault structure and properties. Townsend et al. (1998) used seismic amplitude anomalies to detect small-scale faulting at the limit of seismic resolution. Koledoye et al. (2003) applied a conceptual

model to decompose the seismic expression of a large resolvable normal fault into segments to quantify shale smearing between each segment. Dutzer et al. (2010) used volume-based seismic attributes to determine fault internal structure and transmissibility. Long and Imber (2010; 2012) mapped the spatial distribution of fault-related deformation using a seismic dip anomaly attribute. Iacopini and Butler (2011) and Iacopini et al. (2012) described the geometry of a complex fold-and-thrust-belt and associated damage zones by combining volume-based seismic attributes and visualisation techniques.

Shallow fault zones and their location have been widely investigated in seismology. Methods using anomalous behaviour of the wavefield, e.g. trapped waves recorded by high-resolution seismic, can identify shallow fault zones (e.g. Ben-Zion and Sammis, 2003; Lewis et al., 2005; Shtivelman et al., 2005). Analysing 'trapped wave' behaviour allows understanding of the response of seismic waves in fault zones. These techniques, however, cannot be applied to standard post-stack seismic data, as the faults are at much greater.

All these studies highlight the potential of seismic data to predict fault structure and properties. However, there is still broad scepticism, partly because faults are at the limit of vertical and horizontal resolution (Figure 2), because standard industry seismic data are not designed to deal properly with the non-specular, back-scattered energy from the fault, and interpreters are more accustomed to looking for fault offsets rather than fault-related deformation.

2.2 Attribute-based techniques

Seismic attribute-based methods and image processing techniques have developed considerably in the last years. These methods have been applied to seismic volumes in order to enhance fault detection and interpretation. A definition of seismic attributes given by Taner (2001) is: "Seismic attributes are all the information obtained from seismic data, either by direct measurements or by logical or experience based reasoning". This means that a given attribute should be sensitive to the geological feature of interest. In the case of faults, the attributes need to be sensitive to structural discontinuities or to the fault-induced property changes. However, seismic attributes can enhance subtle features or noise that may otherwise have been ignored (Marfurt and Alves, 2015). Some attributes have been widely used for specific fault

characterisation, such as dip, azimuth, curvature, semblance and structurally oriented filters (e.g. Bahorich and Farmer, 1995; Chopra et al., 2000; Jackson and Kane, 2012).

Fault-detection attributes can be applied to the interpreted seismic horizons or directly to the entire seismic volume. The attributes applied to horizons are called grid-based attributes and look at the horizon geometrical orientation. Fault identification is therefore dependent on the robustness of the horizon's interpretation (e.g. Hesthammer and Fossen, 1997; Brown et al., 2004). Dip, azimuth and curvature attributes are typical grid-based attributes used for fault characterisation. Dip and azimuth are respectively the angle below the horizontal and the azimuth of a vector along the reflector's dip direction; and curvature quantifies the deviation of reflectors from a plane based on local dip changes (e.g. Bahorich and Farmer, 1995; Chopra et al., 2000; Jackson and Kane, 2012). An alternative method is to compute the attributes directly from the seismic data without including horizon interpretation. These are called volume-based attributes Several methods have been developed to calculate volumetric attributes of dip, azimuth and curvature (e.g. Chopra and Marfurt, 2005; Marfurt, 2006; Chopra and Marfurt, 2007). Attributes that deal with the continuity of seismic reflectors throughout the volume, such as the semblance or coherence, are typically used for fault characterisation. The semblance attribute represents a measure of the coherence, i.e. similarity of traces within the seismic cube, to identify abrupt mismatches in amplitude along the reflectors (e.g. Bahorich and Farmer, 1995; Gersztenkorn and Marfurt, 1999; Höcker and Fehmers, 2002; Fehmers and Höcker, 2003). This attribute can reveal faults with different orientations with respect to the reflectors (Chopra et al., 2000). Applying coherence on seismic data in depth reduces possible pitfalls, provided the velocity model is accurate (Marfurt and Alves, 2015). Structurally oriented filters can be used in combination with other attributes to smooth the seismic data along the structures to improve their visibility (e.g. Perona and Malik, 1990; Weickert, 1998; Chopra and Marfurt, 2005). Spectral decomposition is another technique for identification of small-scale faults. This is an amplitude-based attribute that isolates the signal energy as function of frequency, allowing the imaging and mapping of thin beds and geological discontinuities (e.g. Brown, 2010; Jackson and Kane, 2012).

Seismic expression of complex structures such as faults, however, varies considerably even within the same seismic cube. This leads to workflows consisting of several attributes in order to get optimum results and interpretation. In order to avoid false positive correlations, the attributes should be associated with the physical properties and features of interest (Kalkomey, 1997), i.e. faults, and the combined attributes should be independent of one another (Barnes, 2000). Some examples of these attribute-based workflows are presented in the literature. Dutzer et al. (2010) divide the fault zone into inner and outer zones, and use the attributes of semblance, dip and tensor (a measure of the dominant reflectors direction based on the eigenvalues of the local gradient structural tensor) for the inner zone, and structurally oriented curvature for the outer zone. They evaluate lateral thickness and changes in one selected seismic attribute response. This workflow leads to a better highlight of the fault damage zones, including those at the limit of seismic resolution. Iacopini and Butler (2011) and Iacopini et al. (2012) present a visualisation workflow for the deep-water Niger Delta fold-and-thrust-belt. They use opacity, structural oriented filters and volume attributes like semblance, curvature and spectral decomposition, together with visualisation correlation methods such as volume rendering and blending techniques, to improve image quality from post-stack seismic data. Joergensen and Alaei (2015) use a series of attributes, coherence, tensor and variance (e.g. Chopra and Marfurt, 2007), on high-resolution pre-stack data in order to retrieve geometrically connected faults and fault features that are also observed on smaller-scale outcrops.

3 Motivation and potential techniques

The studies above suggest that there is room for improvement and development of new techniques. This leads us to our first question:

- How can we improve seismic imaging, characterisation and interpretation of faults and their related deformation?

Moreover, besides obtaining a fault volume, the ultimate purpose of fault characterisation is to retrieve the petrophysical properties associated with the fault zone and their relative variations with respect to those of the host rock. This brings us to the second question:

- Can seismic data provide enough information to retrieve rock properties in fault zones? If so, how?

The most common approach is to tie the seismic with well data in order to associate a specific seismic response to given rock properties. However, very few wells across faults are available (drillers avoid faults), the uncertainties are large, and the inversion for rock properties is based on several hypotheses (seismic after all detects contrasts in elastic properties, not properties such as porosity or permeability). Answering the two questions above is the motivation of this thesis. In the next section, I describe techniques that could help in answering these two questions, together with their limitations.

3.1 Use of seismic data

To follow the lead of current studies on seismic fault characterisation, we could develop more advanced techniques and attribute-based methods for mapping fault deformation on real seismic data. The main issue with real seismic data though is quality control, which is not easy to perform. Even if we manage to characterise the fault zones with seismic data, we still lack some knowledge of fault structure and properties to fully validate our interpretation. As mentioned earlier, we could use well data to constrain our interpretation. However, well data are normally far from faults and they are local and sparse. We might obtain a good velocity model around a given well but it can be hard

to extrapolate this model to greater distances, and it could be inaccurate near faults. Without a good velocity model, the illumination of features in depth, especially faults, will be limited. If available, 4D seismic or newly acquired or reprocessed seismic datasets could overcome the limited calibration and lead to a better fault characterisation (Hesthammer and Henden, 2000).

3.2 Use of forward modelling methods

The forward problem tries to match the available data, i.e. the seismic data, by relating the model parameters, i.e. geological fault model and rock properties, to an Earth model, i.e. elastic properties model. Based on this definition, we need to have an accurate fault and elastic properties model in order to run seismic modelling.

3.2.1 Seismic modelling

Seismic forward modelling is the creation of a seismic realisation of a given geological model (e.g. Carcione et al., 2002; Krebes, 2004; Sayers and Chopra, 2009; Alaei, 2012). Applying seismic forward modelling to faults is a good way to improve their characterisation and interpretation, as long as the modelling technique can handle the fault's structural complexity. Seismic forward modelling describes the forward process of propagating waves from sources to scatterers at depth in the subsurface and back to the receivers. Seismic wave propagation, however, can be complicated to replicate near or inside fault zones, usually providing an unreliable seismic image of the fault zone. This zone of poor illumination, called the fault shadow, results from velocity changes due to faulting, and can be overcome by pre-stack depth migration (PSDM) with an accurate velocity model (Fagin, 1996). Moreover, the zones of disturbance observed by Nicolaisen (2009), Dutzer et al. (2010) and Iacopini and Butler (2011) have to be integrated into the generation of seismic images. Several techniques have been developed to solve the equation of motion for seismic waves, such as the reflectivity method, full-wave seismic modelling, and ray-based methods; each one varying in complexity, accuracy, computational time and flexibility.

The most common seismic modelling method in the industry is the 1D convolution or reflectivity method in the time domain, i.e. convolution of a

vertical reflectivity log in time with a wavelet (Robinson and Treitel, 1978). This method is mathematically simple, easily programmed, and fast to run, which explains its popularity (Lecomte et al., 2015). However, 1D convolution can only simulate post-stack time-migrated sections for full-aperture surveys and models without lateral variations. Applying 1D convolution to 2D or 3D models with discontinuities, such as faults, can be misleading, with possible mispositioning of seismic events and total lack of lateral resolution effects (Lecomte et al., 2015). When using models without lateral variation, the obtained zero-offset trace can be representative of a recorded seismogram. However, no lateral resolution effects are considered, even though horizontal variations can influence amplitudes and structural information. 1D time convolution (MacBeth et al., 2005) has been applied to fault models by Couples et al. (2007), although with unrealistically high wave frequency and small trace spacing. This imaging does not entirely capture the lateral variations and complexity of fault zones as they are observed on seismic data (Figure 2); therefore this method is not adequate for our purposes.

The ideal way to generate a complete synthetic seismogram is to solve the full-wave equation. Methods for doing this have the ability to accurately reproduce seismic waves in arbitrary heterogeneous media. Amongst these methods, finite-difference (FD) techniques are the most used and best known. They comprise a range of numerical methods for solving differential equations applied to the seismic wave equation at a discrete set or over a grid to calculate displacement at any point in a geological model (e.g. Alaei, 2012). The main advantage of these techniques is that they are able to produce all existent wave types (reflections, refractions, head waves, etc.) with their correct amplitudes and phases (e.g. Krebes, 2004; Alaei, 2012). The obtained synthetic seismic cubes can be further used for processing tests. Although very complete, this method requires experts to solve the equations and high computer memory, and it is extremely time-consuming. FD acoustic wave-equation realisation (Stockwell and Cohen, 2002) has been applied to geological models of fold-and-thrust belts in 2D, showing that the complexity of the seismic response of these structures is not due to acquisition problems but rather to the need for advanced processing methods (Alaei and Petersen, 2007). Using FD for specific fault characterisation requires close collaboration between the geologist who

understands the faults and the geophysicist who can provide the FD method and further accurate processing of the obtained seismogram.

A good compromise between the simple 1D reflectivity methods and the demanding FD methods are the ray-based approaches. Ray-tracing methods use ray theory to compute seismic wave travel times and amplitudes along ray paths in a heterogeneous medium, following the high frequency approximation of the wave equation. As a high frequency or low wavelength approximation, ray theory cannot be applied accurately to structures within layers thinner than the dominant wavelength. Also the method does not produce the complete wavefield; only specific waveforms chosen by the user can be modelled in the synthetic seismogram (Krebes, 2004; Alaei, 2012). Moreover, ray theory is not accurate near critical offsets, even though some corrections can be made (Krebes, 2004 and references therein). For deep reflectors in horizontally layered media, the reflection angles are generally small so ray theory can be used safely, whereas at shallow depths, it might not be appropriate. However, ray theory is widely used, especially for 2D layered models, because of the relative simplicity of some versions of the method, the fast computational times, and the fact that the ray paths for all the events on synthetic seismograms can be identified from the event travel times. The method is really useful to compute travel times if not always signal amplitude. Some ray-based methods have been developed in order to be able to handle 3D lateral resolution and illumination in PSDM images (Lecomte, 2008; Lecomte et al., 2015). This 3D spatial convolution approach models PSDM point scatter responses and also reflectors (Lecomte et al., 2003), with computational times close to 1D convolution and more accessible than FD methods. This method, relatively easy to learn for geologists, has recently been applied to geological models, including faults (Botter et al., 2014; Lecomte et al., 2015; Mascolo et al., 2015; Wood et al., 2015) showing promising results for 3D fault imaging.

3.2.2 Fault models

Applying seismic modelling requires an input geological model and an elastic properties model that both reproduce reservoir conditions. The geological model should be consistent with reservoir faults at seismic scale and take into account their 3D architecture and petrophysical properties distribution. Such fault models can come from outcrop-based studies, seismic

interpretation, scale analogue models, or numerical kinematic or mechanical models. I will only describe the models most relevant to this thesis: outcrop and seismic-based models, and mechanical models.

3.2.2.1 Outcrop models

A representation of the fault based on outcrop data can produce an accurate model at reservoir conditions. The advantage of such strategy is that one is able to constrain the structural model and some of its properties directly by field mapping. There are examples of large-scale outcrops that have been used for seismic modelling in 2D, such as the carbonate platform and talus deposits in the Maiella Mountains, central Italy (Mascolo et al., 2015). Virtual outcrop models acquired by LiDAR or photogrammetry (e.g. Buckley et al., 2008) provide abundant and detailed information about stratigraphy and structure that can be used as input for seismic modelling (Lecomte et al., 2015). Such models, however, are often pseudo-3D (Lecomte et al., 2015). Wood et al. (2015) built a geocellular model of a high-resolution outcrop model. Even though their model is 3D, it is actually a 2.5D representation of the fault outcrop in a 2D section. They populate their grid using sets of petrophysical properties corresponding to homogeneous sandstone and to the vertical stratigraphy of the Brent Group in the North Sea.

Going from outcrop to reservoir modelling is also an interesting possibility to better constrain the petrophysical properties of the fault model (Rotevatn and Fossen, 2011; Fachri et al., 2013). Reservoir properties can be defined using field measurements of laboratory testing. However, upscaling of these properties to the reservoir model is not trivial. Despite this complication, outcrop-based reservoir models are a powerful way to study fault complexity.

3.2.2.2 Seismic-based geomodels

Another way to obtain a fault model is to build a geomodel based on the interpretation of seismic data. This gridded model can be populated from well logs and core data if available. Seismic modelling of such representation of the subsurface can be run under several acquisition and processing conditions in order to validate and/or improve the geological interpretation. Alaei (2006) and Alaei and Petersen (2007) show examples of seismic

modelling for investigating the validity of seismic interpretations in fold-and-thrust-belts.

3.2.2.3 Mechanical models

The purpose of mechanical modelling is to study the evolution of complex structures that cannot be fully described by analytical techniques. These models are typically non-linear and non-conservative, such that they can only be run forward (Buiter et al., 2006; Gray et al., 2014). The advantage of mechanical models in comparison to outcrop- or seismic-based models is that geometry, kinematics, stress, strain (incremental and total), and to some extent rock properties are known at any stage of the modelled evolution of the structure. Several mechanical techniques have been used to model faults. These can be divided into continuum and discrete element methods.

Continuum methods model the mechanical behaviour of geological materials as a continuous mass. Among these methods, we can cite finite-element, finite-difference, and boundary methods, with finite-element methods (FEMs) being the most adapted to fault modelling (e.g. Gray et al., 2014). FEMs encompass methods for connecting equations over small subdomains of the model, called finite elements, to approximate a more complex equation over the larger model. The finite elements share nodes, edges and surfaces that are defined within the meshed model. At each time-step, the mesh is deformed according to pre-defined boundary conditions, and the propagation is made via a system of equations (reflecting a constitutive model) throughout the mesh until equilibrium is reached. For large deformations, the finite elements can become so distorted that remeshing is needed. Some examples of FEM include simulating the mechanical behaviour of sedimentary layers above basement faults (Niño et al., 1998), simulating the strain distribution within fault-bend folds (Gregg Erickson and Jamison, 1995), modelling fault propagation folds (Cardozo et al., 2003), analysing the influence of far-field compression (Sanz et al., 2007), studying fault propagation (Couples et al., 2007), and comparing basement-involved compressional folds (Zhang et al., 2013; Gray et al., 2014).

Discrete element techniques are adapted from molecular dynamics and utilize particles rather than mesh elements to represent geological materials (e.g. Place and Mora, 1999). Discrete element methods (DEMs) allow large

deformations involving large relative displacements of individual particles without the need for remeshing (Cundall and Strack, 1979; Finch et al., 2004; Egholm et al., 2007; Hardy, 2008, 2011). In addition, they allow localization and the formation and linkage of faults and fractures as a natural part of the numerical scheme. The discrete nature of DEM, however, poses unique challenges. One issue is the computing limitation on the number and size of particles, which for large km-scale models prevents simulating processes at the grain scale. Also, contrary to FEM, it is not possible to specify a priori the stress-strain response of the assemblage. Therefore it is necessary to carry out calibration of particle properties to the emergent rock physical properties (Egholm et al., 2007; Holohan et al., 2011). Discrete element simulations of thrust-related structures have been carried out by Finch et al. (2003), Strayer and Erickson (2004), Cardozo et al. (2005), Hardy and Finch (2006), Benesh et al. (2007), Hardy et al. (2009), Zhang et al. (2013) and Gray et al. (2014). Fault evolution in multilayer m-scale sedimentary sequences has been studied by Schöpfer et al. (2007). Egholm et al. (2008) looked at clay smearing along cm-scale normal faults. Terheege et al. (2013) compared laboratory and DEM clay smear along faults. Abe and Mair (2005) looked at grain fracturing in 3D. All these studies show the DEM as a powerful technique for modelling faulting at different scales including seismic.

3.2.3 Rock elastic properties

Seismic reflections result from contrasts in rock elastic properties defined by seismic wave velocities and densities, which control seismic impedance. These elastic properties are related to lithology, fluids in the pore space, and rock deformation among other things. Relationships between fault-related deformation (as observed in outcrop or monitored in mechanical models through strain) and elastic properties are necessary for forward seismic modelling.

The relationships between stress, strain and elastic properties are reasonably well defined for the purpose of wave propagation where rocks are within the elastic regime (e.g. Mavko et al., 2009). When rocks deform beyond the elastic regime, like during faulting, those relationships are no longer valid. Not many studies have discussed the impact of large strains on rock properties. Hatchell and Bourne (2005) looked at the impact of pressure depletion induced

strain and fracturing on seismic velocities in a reservoir. They showed that cracks, especially horizontal, have a strong influence on P-wave velocity. Holt et al. (2008) studied the impact of small volumetric strains (lower than 1%) on seismic velocities in cm-scale sandstone and shale samples. They showed that cemented sandstone typically exhibit velocities that increase with strain. Skurtveit et al. (2013) showed the same impact of strain on seismic velocities by investigating deformation mechanisms and their impact on ultrasonic velocity during shear-enhanced compaction of poorly lithified, cm-scale sandstone samples (volumetric strains lower than 5%).

Several studies have also measured seismic velocities on selected samples of fault outcrops. Sigernes (2004) measured seismic velocities in cm-scale samples at several distances from the fault core in five normal fault outcrops in siliciclastic rocks. She identified three different scenarios: (1) increasing velocities with distance from the fault, (2) decreasing velocities with distance from the fault and (3) velocities appearing to be independent of distance from the fault. Jeanne et al. (2012) analysed the structure and properties of a 50 m long strike-slip fault zone in limestones, southern France. They showed that P-wave velocity variations decrease from the fault centre to the host rock. However, important variations were measured across the fault zone that strongly correlate to some key parameters such as the uniaxial compressive strength of the fault core, the initial porosity and fracturing degree of the damage zone, and stratigraphy. Healy et al. (2014) studied faulted Oligo-Miocene carbonates in the Mediterranean region to better understand controls on the porosity and seismic velocities. Overall their measurements showed an increase of seismic velocities and decrease of porosity towards the fault core. Development of fault rocks within the fault zone produced a reduction in porosity and increase in seismic velocity.

These studies encompass a large range of lithologies, scales and strains. They broadly illustrate how volumetric strain and fracturing modify seismic velocities. In siliciclastics, compaction (i.e., negative volumetric strain) decreases porosity, thereby increasing density and seismic velocities, while dilation (i.e., positive volumetric strain) and shear or tensile induced fracturing have the opposite effect (Table 1). In carbonates this picture is more complicated because of additional chemical effects. These studies also show high variability of properties within the fault zones (Table 2).

Table 1: *Summary of the impact of strain and fracturing on seismic velocities for siliciclastics. From Hatchell and Bourne (2005), Holt et al. (2008) and Skurtveit et al. (2013).*

	Pore Space	***Density***	***P-wave velocity***
Compaction	**-**	**+**	**+**
Fracturing	**+**	**-**	**-**

Table 2: *Summary of the approximate maximum changes in P-wave velocity (V_P), S-wave velocity (V_S), and porosity (ϕ) in the fault core with respect to the average values of these properties in the protolith, both for siliciclastics and carbonates.*

	Changes of V_P		***Changes of V_S***		***Changes of ϕ***	
Siliciclastics *Sigernes*	Max increase	Max decrease	Max increase	Max decrease	Max decrease	Max increase
	10–40 %	45 %	5–45 %	45 %	5–10 %	10 %
Carbonates *Jeanne et al.*	0 – 50 %		/		0 – 20 %	
Carbonates *Healy et al.*	0 – 50 %		0 – 45 %		10 – 25 %	

4 Objectives and workflow

4.1 Objectives

In order to improve seismic imaging and characterisation of fault structure and properties, the objectives of this thesis are:

- To provide realistic models of faulting comprising fault structure and distribution of fault properties.
- Through empirical relationships, to establish a link between fault-related strain and elastic properties.
- Through seismic modelling, to obtain seismic images of the fault models and run sensitivity analyses on these images.
- To investigate ways to interpret fault architecture and rock properties from the seismic images.

4.2 Workflow

In the three papers making up this thesis, we apply a synthetic workflow encompassing the objectives of the thesis (Figure 3). The workflow is divided into four main steps:

1. Fault modelling at seismic scale.
2. Changes of elastic properties due to fault-related strains.
3. Seismic modelling and sensitivity analyses.
4. Interpretation of the seismic cubes and correlation with the input properties.

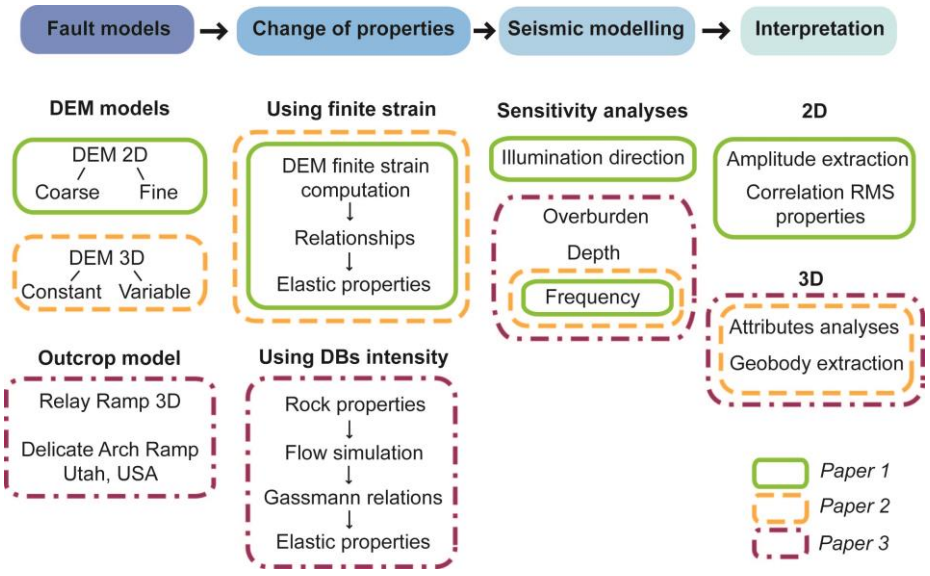

Figure 3: *Workflow applied in the thesis. The first row presents the four steps of the workflow and the columns show the different techniques used to complete these steps. The boxes indicate in which papers the techniques are used.*

Similar workflows have previously been applied to faults. Sigernes (2004) built simple models of normal faults populated with outcrop-based data, and obtained seismic images of these models with acoustic FD. Alaei and Petersen (2007) built a fold-and-thrust-belt model of the Zagros region and populated it with velocity and density models from well logs, check shots and seismic processing methods. They obtained synthetic seismograms using and acoustic FD method in order to test several processing steps. Couples et al. (2007) used FEM to simulate normal faulting, and 1D convolution of the geomechanical model (with acoustic properties modified by finite strain) to produce a seismic image of the fault. Our workflow differs from these previous studies in the methods of implementation of each step, and the specific applications in each paper (Figure 3):

1. To obtain a fault model at seismic scale representing the complexity of fault architecture at reservoir depths, we use a DEM (Hardy et al., 2009) in 2D (paper 1) and in 3D (paper 2), and an outcrop-based reservoir model in paper 3. In papers 1 and 2, we model a large-scale (about 100 m displacement) normal fault in a km size interlayered shale and sandstone sequence. In paper 3, we use a reservoir model based on detailed field mapping of a relay ramp in the Jurassic Entrada sandstone of the Arches National Park, Utah (Rotevatn et al., 2007 and 2009).

2. To compute the elastic properties after faulting, in papers 1 and 2, we modify the initial/base elastic properties (V_P, V_S and density) based on the finite strain of the DEM using a simple empirical relationship. In paper 3, the properties of the sandstone reservoir are modified by the frequency of deformation bands (Rotevatn et al., 2009) and the fluid content during simulated production.

3. The elastic properties are used to construct a reflectivity volume, which is the input for seismic modelling. We use a ray-based PSDM simulator (Lecomte, 2008; Lecomte et al., 2015) in all the papers. This technique allows us to run sensitivity analyses, such as on wave frequency, survey design or background model, to fine-tune acquisition and processing parameters for specific fault characterisation.

4. For 2D seismic images (paper 1), the interpretation consists of extracting the seismic amplitude along reflectors, associating their fluctuations to the input fault architecture. Quantitative correlation is made between the RMS amplitude and the input RMS elastic properties of the corresponding reflector. For 3D seismic cubes (papers 2 and 3), we use an attribute-based interpretation workflow that is able to extract a geobody corresponding to the fault volume. From this geobody, amplitudes values are cross-plotted against input model properties for quantitative correlation.

5 Methodology

The methodology is well explained in the three papers. In this section, the specific DEM implementation, changes of properties due to finite strain, and the PSDM simulator are presented. The reader can refer to the papers for the other techniques, such as the attributes-based fault volume extraction workflow (papers 2 and 3), or the property definition and flow simulation of the Delicate Arch Ramp (papers 3).

5.1 DEM

The particular DEM employed here is a variant of the lattice solid model of Mora and Place (1993), further developed by Hardy and Finch (2005, 2006) and Hardy et al. (2009), where the rock mass is modelled as an assemblage of circular particles in 2D or spherical particles in 3D (Figure 4a). These particles are rigid and have a given radius and density. They interact with elastic, frictional, and gravitational forces (Figure 4). The bulk mechanical behaviour of the assemblage is purely frictional, with no tensile strength (Belheine et al., 2009; Hardy, 2013). For simulations at a few kilometres depth in an upper crust full of discontinuities, a purely frictional failure envelope is an adequate representation of rock behaviour (Hubbert, 1951; Zoback, 2010). Imposed displacement conditions are applied to the boundary particles in order to initiate and propagate faulting in the sequence above (Figure 4a). At each time step, the total forces applied to a particle by its neighbours are used to compute its displacement. The particles are moved to their new positions by integrating their equations of motion using Newtonian physics and a Verlet numerical velocity scheme (Mora and Place, 1993; Figure 4d and e). To bring the model to reservoir depths, I modified the existing algorithm in 2D in order to apply an overburden stress at the top of the assemblage. This is a traction component applied at the centre of the particles, normal to the slope of the top surface. For each particle, the slope defined by its left and right neighbours is calculated, and the overburden traction is applied perpendicular to it. The traction is updated every few time-steps such that it is always normal to the upper surface of the model (Figure 4c). The same methodology is used in biaxial simulations for the calibration of the rock materials. However, in 3D, the update of the

traction direction is more difficult to implement and would drastically slow down the computation. To obtain results in a reasonable time, the overburden traction is applied vertically at the beginning of the simulation and it is not updated afterwards (Figure 4e).

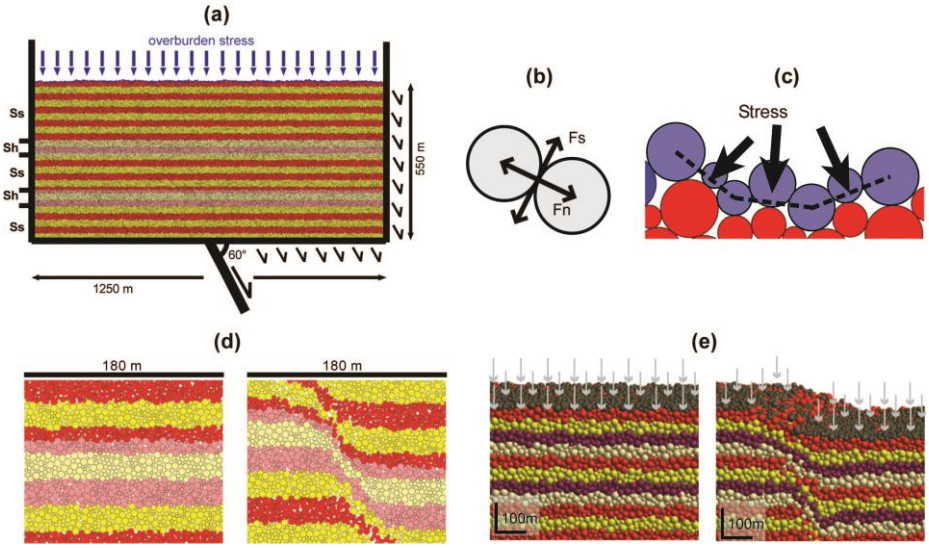

Figure 4: *Example of the DEM used in the workflow: (a) Initial 2D fault model with four different particle radii, sedimentary layering (Ss = sandstone and Sh = shale), and boundary conditions for a 60° dipping normal fault. (b) Normal (Fn) and shear (Fs) forces at particle contacts. (c) Overburden stress applied normal to the top surface in 2D. (d) Zoom of 2D model before (left) and after (right) faulting. (e) Zoom of 3D model before (left) and after (right) faulting. Grey arrows show the overburden tractions.*

The calibration of the assemblage aims to make it behave like a real sedimentary rock at a few kilometres depth. In 2D, we have the possibility to implement collapse and biaxial compression simulations. Such tests are performed on a subportion of the system in order to evaluate multiple sets of values of particle properties within acceptable runtimes (Finch et al., 2004; Hardy et al., 2009; Holohan et al., 2011; paper 1). Collapse simulations allow the measure of the static angle of repose of the material, and biaxial tests at

several confining pressures allow the measure of the failure envelope of the material. The obtained values are compared to the literature for competent sandstone (Zoback, 2010) and more incompetent shale (Horsrud et al., 1998). I did not have the possibility of running these tests in 3D. In order to obtain a reasonable mechanical behaviour of the assemblage at low cost and computational time, we studied the overall bulk behaviour of a homogeneous assemblage under boundary conditions similar to those of the fault model. We use two homogeneous assemblages intended to simulate sandstone and shale-type materials (paper 2). The average dip of the propagating fault was compared to literature values for these materials (dip of normal fault = 45° + friction angle/2).

5.2 Changes of properties due to strain

We use the information in Table 1 and Table 2 to derive empirical relationships between rock properties and fault-related strains. We consider that rock properties are only impacted by compaction/volumetric strain in the DEM as described in Table 1. Shear strain effects, which can be important for fracture-induced porosity (Table 1), are neglected in our model. Initial rock property values in the DEM are taken from the literature for sandstone (Hoek and Brown, 1997; Mavko et al., 2009) and shale (Horsrud et al., 1998; Nygård et al., 2006). We use the computed volumetric strain from the DEM to modify these initial rock properties. The strain is computed using a nearest-neighbour algorithm that divides the DEM model into regular cells and computes the strain from the displacements of particles within a maximum radius from the cell centre (Cardozo and Allmendinger, 2009). Effectively, we upscale the heterogeneous strain in the fault volume to a cell-based strain. Although not a direct measure of the physical processes occurring in the rocks at the grain scale, the computed strain is a proxy of these processes.

We take into account the relative changes in rock properties of Table 2. These measurements show a variation in wave velocity up to 50% in samples from fault zones. However, strong property variations also exist in the host rock samples (Jeanne et al., 2012; Healy et al., 2014). Thus, the changes in Table 2 may not only be due to faulting, but also to the heterogeneities of the protolith and to the fact that laboratory measurements from core samples can

overestimate the values of the rocks in situ (Nes et al., 2000; Holt et al., 2008). Therefore, we estimate that a maximum change of properties due to faulting of ±25 % is reasonable for our model scales and depths. We also take into account that compaction should be less than 100%.

We decide to target the impact of strain on the porosity instead of the density, which also gives us flexibility in defining the rock matrix and fluid densities. The porosity is modified from its initial value according to a linear relation (Figure 5):

$$\phi = \phi_{ini}(0.25\varepsilon_v + 1), \qquad -1 \le \varepsilon_v \le 1 \tag{1}$$

where ϕ is porosity, ϕ_{ini} is initial porosity and ε_v is volumetric strain. Porosity changes are unlikely to vary linearly with strain, however data from Skurtveit et al., 2013, Figure 5) and from Sigernes (2004) show that porosity changes fluctuate less than velocity changes. Although simplistic, a linear relation can be considered as an acceptable approximation. Rock density ρ is then computed from porosity assuming water-saturated conditions:

$$\rho = \rho_g(1-\phi) + \rho_w\phi \tag{2}$$

where ρ_g and ρ_w are grain and fluid densities respectively. V_P follows a sigmoidal relation (Figure 5):

$$V_P = \begin{cases} V_{P_{ini}}(-0.25\varepsilon_v^2 - 0.5\varepsilon_v + 1), & -1 \le \varepsilon_v < 0 \quad (\textit{compaction}) \\ V_{P_{ini}}(0.25\varepsilon_v^2 - 0.5\varepsilon_v + 1), & 0 \le \varepsilon_v \le 1 \quad (\textit{dilation}) \end{cases} \tag{3}$$

where V_{Pini} is the initial P-wave velocity. A sigmoidal shape results in stronger changes in velocities at smaller strains than at larger strains. This is consistent with laboratory measurements showing very large V_P changes at small strains (Holt et al., 2008; Skurtveit et al., 2013) and our hypothesis of maximum relative changes of ±25 %.

Sigernes (2004) and Healy et al. (2014) looked at the correlation between V_P and V_S for siliclastic and carbonate rocks, respectively. They both show linear correlations from the fault core to the host rock. Moreover, Sigernes

(2004) estimated that for sandstone and shale this relation is within the range defined by Han and Castagna's empirical laws. Therefore, we use Han's (1986) relation to compute V_S:

$$V_S = 0.794V_P - 0.787 \qquad (4)$$

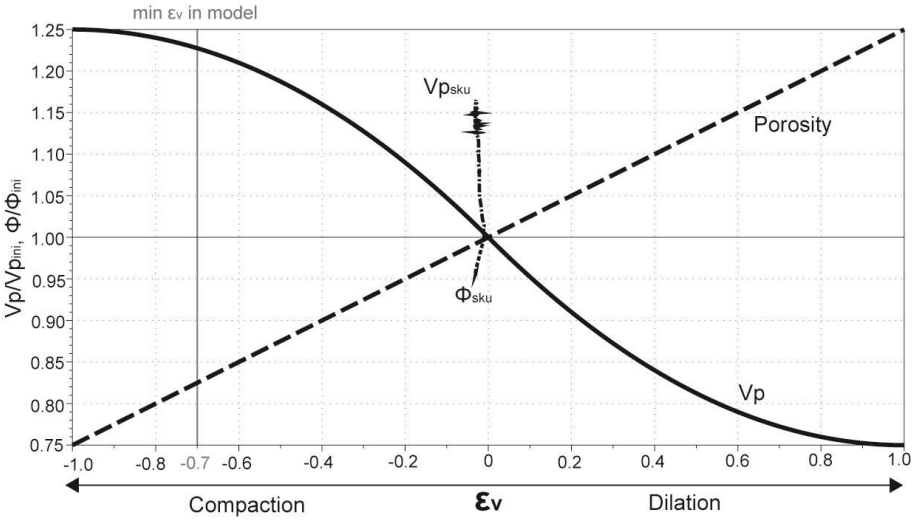

Figure 5: *Assumed changes of porosity ϕ and P-wave velocity V_P with volumetric strain ε_v. ϕ_{ini} and V_{Pini} are porosity and P-wave velocity before faulting. ϕ_{sku} and V_{Psku} are porosity and P-wave velocity from triaxial testing of poorly lithified sandstone at 15 MPa (Skurtveit et al., 2013). Min ε_v is from 2D DEM models (paper 1).*

Equations 1 to 4 allow us to compute the change of rock elastic properties due to fault-related strains. Even if the estimated values are not accurate, they are within a reasonable range. As stated by Hatchell and Bourne (2005) and Couples et al. (2007), a simple relationship between finite strain and acoustic properties, although probably inaccurate, is a reasonable way to assess the impact of faulting on seismic data.

5.3 PSDM simulator

Most seismic data available to interpreters are post-stack time-migrated data. However, the ultimate goal of seismic processing is pre-stack depth-migrated data. The technique we use is a PSDM simulator (Lecomte, 2008; Lecomte et al., 2015) that acts as an image-processing method by distorting the input reflectivity to reproduce the effects of seismic imaging in PSDM mode. This method does not provide the complete modelling of FD methods, but it handles 3D effects in resolution and illumination as functions of various parameters such as velocity model, survey geometry and wavelet, with a computational time close to 1D convolution (Lecomte and Kaschwich, 2008).

The structural input to the PSDM simulator is an incidence angle-dependent reflectivity grid obtained from the elastic properties, V_P, V_S and density of the fault model (Figure 6a). This reflectivity cube is converted to the wavenumber domain by a fast Fourier transform (FFT). In the wavenumber domain, ray-based modelling is used to generate the so-called PSDM filters, which are dependent on survey geometry, frequency content, wave type, and velocity model (Figure 6b). The reflectivity grid is then multiplied to the PSDM filter. Applying an inverse FFT on this product gives the simulated seismic image in the spatial domain (Figure 6c).

To visualize the local imaging capability of the PSDM filter, we can look at the response of a scatterer at a reference point by applying an inverse FFT directly to the filter (Figure 6d). This response in the spatial domain is called a point-spread function (PSF) and can be used as a reference for the vertical and horizontal resolution of the seismic image. Geological features that are not encompassed within the PSF range and dip, such as high-angle faults, will not be visible on seismic and they will be harder to interpret (Figure 6c). Therefore, changing the illumination direction can help to highlight features that would be ignored in standard conditions (e.g. in Figure 6c, Fs is more visible on the footwall illuminated seismic image than on the specular illuminated one).

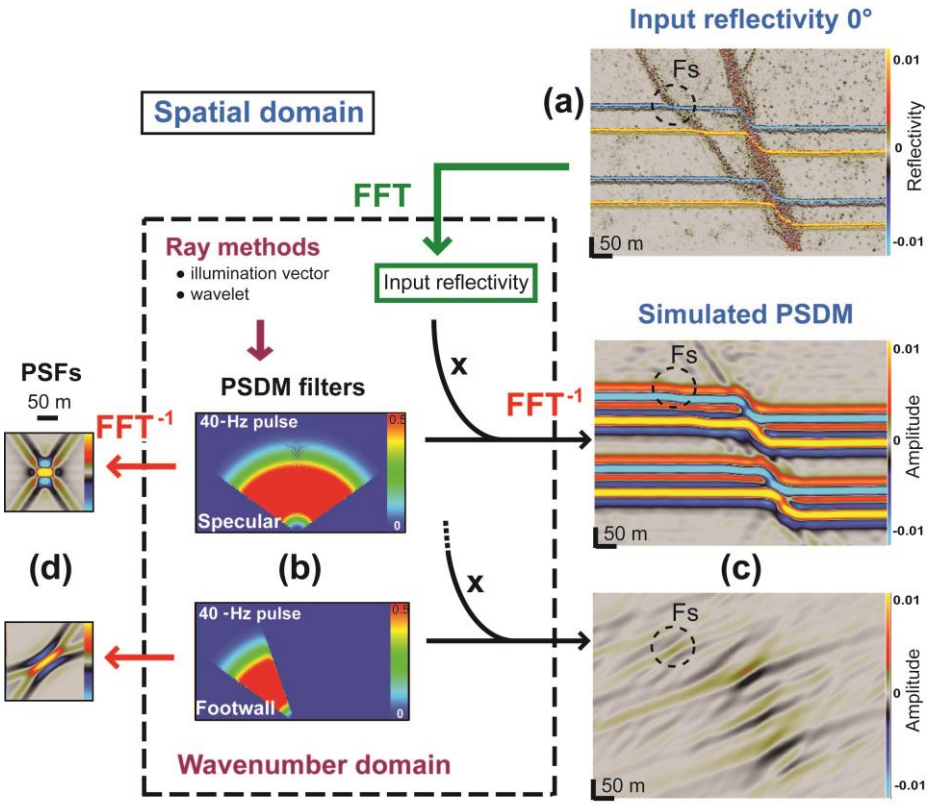

Figure 6: *Illustration of the PSDM simulator (fine model, paper 1). (a) Input reflectivity grid in the spatial domain and conversion to the wavenumber domain using a Fast Fourier Transform (FFT). (b) Calculation of PSDM filter in the wavenumber domain, using ray-based methods for specular (top) and footwall (bottom) illuminations. (c) Application of the PSDM filter to the input reflectivity in the wavenumber domain, plus inverse FFT (FFT^{-1}) on the result, produce the PSDM image. (d) Entire process is equivalent to convolution of the point spread function, or PSF, with the input reflectivity. Fs highlights the location of the smaller fault segment.*

6 Synthesis of the publications

The research has been divided into three main topics, each of them the subject of a publication. This section summarizes these papers.

6.1 Paper 1: DEM 2D

PAPER 1 applies the workflow to a 2D, large-scale (100 m displacement) normal fault model in an interlayered sandstone-shale sequence for two assemblages of similar bulk stress-strain behaviour but different particle size: one with coarser particles (1-3 m) and another with finer particles (0.5-1.5 m). Both simulations produce realistic but different fault geometries and strain fields, with the finer-particle-size model displaying narrower fault zones and fault linkage at later stages. Two reflectivity grids corresponding to the coarse- and fine-particle-size models are constructed applying the simple relationships between change of elastic properties and volumetric strain (Figure 5) to the models. PSDM simulations of the two models for four wave frequencies and three illumination directions, i.e. specular, hanging-wall and footwall illuminations, are presented. Resolution and accuracy of the reflectors increase with wave frequency. Wave frequencies of 20 Hz or more are necessary to image the different fault structures of the coarse and fine models. Hanging-wall illumination highlights directly the fault plane, but footwall illumination is the only one that makes the smaller-displacement fault segment of the fine model detectable (Fs in Figure 6c). We look at the variation of seismic amplitude along interpreted reflectors in the seismic images, and compare the RMS amplitude to the variations of RMS elastic properties along the same paths in the input reflectivity models. At high wave frequencies, there is a direct correlation between seismic amplitude variations and the input acoustic properties.

6.2 Paper 2: DEM 3D

PAPER 2 illustrates the workflow for a 3D large-displacement normal fault in a sandstone-shale sequence for two cases, one with constant fault displacement and another with linearly variable displacement along strike. Seismic cubes of these models for a homogeneous overburden, a full covering

survey and several wave frequencies are generated. High frequencies show the impact of the fault on the offset and distortion of the reflectors. In the variable fault-slip model, the fault has less impact as the displacement decreases, and the fault tipline can be interpreted. We extract the fault geobodies from the 40 Hz seismic cube using three combined seismic attributes: dip, semblance and tensor (Dutzer et al., 2010). The geobody for the constant fault displacement model corresponds to an inner high deformation area within the fault zone, while in the variable fault-slip model the geobody captures better the entire fault zone. Cross-plotting of amplitudes and strains shows that the geobodies contain all range of strains, but almost all high strain values are within the geobodies. This allows a direct comparison between the fault zone identified on the seismic image and the fault volume in the mechanical model.

6.3 Paper 3: Delicate Arch Ramp

PAPER 3 illustrates the workflow for a reservoir case scenario. We use the results of a fluid flow simulation in an outcrop-based model from the Delicate Arch relay ramp, Utah (Rotevatn et al., 2007 and 2009) to study the impact of relay ramps and their fluid composition on seismic data. The petrophysical properties of the high-porosity Jurassic Entrada sandstone are conditioned by the frequency of deformation bands and are used to run a simple water-injector/oil-producer fluid flow simulation. PSDM simulated seismic cubes are generated for several stages of the flow simulation, thus producing 4D seismic. Changes in porosity in the fault damage zones are visible in the oil-saturated model at the beginning of the simulation, whereas the water-oil contacts have stronger impact at later stages. With an adapted tuning of the attribute-based workflow, we are able to extract volumes corresponding to the two faults and the relay ramp from the seismic cubes at several stages of the flow simulation. Additional quantitative analyses in the extracted geobodies were performed to investigate the correlation between the seismic amplitude and the input rock properties (Appendix 1). By varying model parameters, we also show reservoir and acquisition conditions that can affect positively or negatively the resolution of the relay-ramp seismic imaging.

7 Discussion and conclusions

Through the synthetic workflow of this thesis (Figure 3), I studied the impact of fault zone structure and damage on seismic images and their interpretation. In this last section, I will discuss how this research has contributed to improve our knowledge of seismic fault characterisation, as well as to the understanding of its limitations.

7.1 Seismic data for characterisation of faults as volumes

Our work has shown that fault zones and fault-related deformations can be observed and mapped directly from seismic data. Paper 3 highlights that fault damage rather than its displacement is visible on the seismic images of a homogeneous reservoir, even at small fault displacements, as long as faulting induces changes in elastic properties. Jeanne et al. (2012) also found out that even if a fault cannot be detected by a clear offset, it still has a characteristic seismic signature corresponding to low-velocity bodies around the fault core. Healy et al. (2014), however, did not detect significant changes of rock properties within faults in carbonates for displacements lower than 20 m. This can also be observed in paper 2, where the fault tip cannot be identified at small displacements in seismic cross-sections. In a layered sedimentary sequence, even if the offset of reflectors clearly indicates the fault, interpreting it as a 2D surface is too simplistic, as emphasized in Figure 15 of paper 1. Indeed, the fault zone induces diffractions and reflections that allow the mapping of the fault volume (papers 1 to 3).

7.2 From seismic data to geological interpretation

The use of interpretation techniques is essential for a better characterisation of the fault volume. As a first step, careful study of the seismic images in 2D and 3D is necessary to distinguish fault-related features. However, this interpretation becomes speculative when one needs to identify features below seismic resolution, such as the fault tipline (paper 2). Using computer-based

techniques can be a less biased way to interpret the fault architecture, as well as features that are not visible from human investigation. In 2D (paper 1), the RMS amplitude along interpreted reflectors helps to better define fault architecture, such as the smaller fault of the fine model (Figure 14 of paper 1). Papers 2 and 3 show the importance of seismic attribute workflows in 3D seismic cubes, provided that the user is aware of the assumptions behind the attributes, in order to avoid pitfalls in the structural interpretation (Marfurt and Alves, 2015). In addition, to aid the fault volume extraction, a fine tuning of the attributes can highlight either the inner part of the fault, where the highest strains are concentrated (constant fault-slip model in paper 2), or the larger damage zone (variable fault-slip model in paper 2). This has also been discussed by Dutzer et al. (2010). Moreover, helped by the attributes workflow, we are able to delineate the fault tipline in paper 2, and to extract the fault damage as fluids move through the model in paper 3.

Our seismic attributes study is complementary to those Dutzer et al. (2010), Iacopini and Butler (2011) and Iacopini et al. (2012). Dutzer et al. (2010) were able to delineate subseismic faults, thanks to the use of combined attributes, in a high-quality onshore seismic dataset. To retrieve the input geology, they associated the fault disturbance zones extracted from the seismic with an acoustic impedance attribute highlighting shale-to-sandstone contacts. Iacopini et al. (2012) applied a combination of curvature, dip and semblance on a seismic dataset from a deepwater fold-and-thrust-belt and cross-plotted curvature and semblance in order to define and extract fault geobodies corresponding to two types of deformation, the fold back-limbs and the thrusts discontinuities in the fold forelimbs. The application of the fault-volume extraction workflow to our synthetic models is a proof of concept of the attribute-based methods for identifying faults and fault-related deformations. Whilst Dutzer et al. (2010) constrained their acoustic impedance interpretation to well-log V_P data, and Iacopini and Butler (2011) and Iacopini et al. (2012) their extracted geobodies to previous outcrop studies of fold-and-thrust-belts available in literature (e.g. Williams and Chapman, 1983; Butler and McCaffrey, 2004), our workflow can go further by relating the seismic amplitude to the distribution of elastic rock properties or strains within the input fault models. Although the fault geobodies capture all ranges of amplitudes, the fault-enhancement attribute shows that the higher probabilities of getting a fault correspond mostly to the larger strains

(paper 2) or to the larger changes of properties with respect to those of the host rocks (papers 1 and 3; Appendix 1).

7.3 Impact of seismic resolution

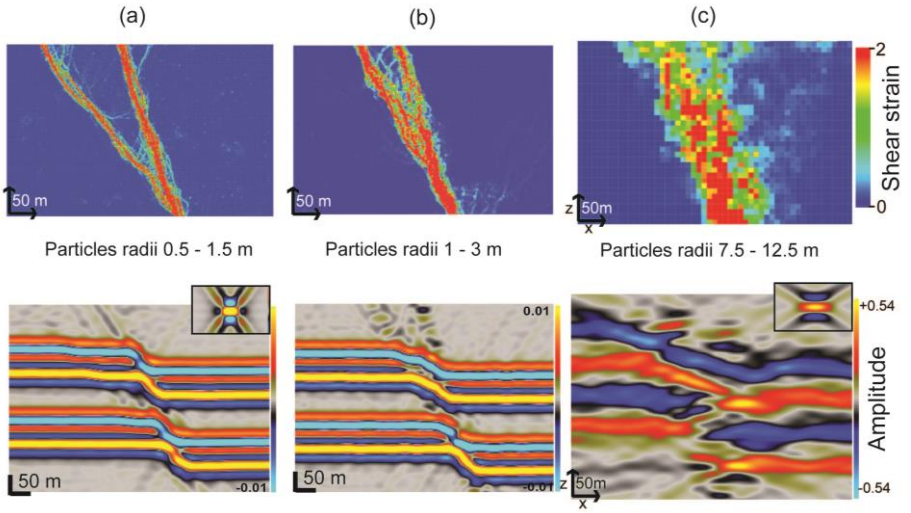

Figure 7: *Impact of particle size on fault architecture. Shear strain (first row) and seismic image at 40 Hz (second row) of (a) the 2D DEM fine fault model, (b) the 2D DEM coarse fault model, and (c) Dip section of 3D DEM constant displacement fault model. The PSFs are displayed in the right top corner of the seismic images.*

Through our workflow, we have shown that the definition and resolution of the fault architecture and distribution of fault-related properties have an important effect on the seismic imprint. In the 2D DEM model, the particle size is the parameter that has the strongest impact on the resultant fault architecture. The assemblage with smaller particles (Figure 7a) displays narrower fault zones, more fault segments and more localised strains than the coarser one (Figure 7b). The finer fault architecture provides fault segments below seismic resolution (e.g. Figure 7a at 40 Hz), which results in less fault zone-related reflection and diffraction than the coarser one (Figure 7b). While we can focus more on fault architecture characterisation in the 2D DEM model (Figure 7a and b), the larger particles of the 3D DEM model do not give that detail, instead,

the seismic image highlights a complex seismic response with the interaction of reflectors in the fault zone (Figure 7c). Even though it is approximate, the detailed description of the distribution of fault properties in the DEM models (papers 1 and 2) provides a realistic seismic response, i.e. reflections and diffractions (Lecomte et al., 2015). Paper 3 also highlights the fact that stronger changes in rock properties (i.e. porosity and permeability) due to faulting give a more significant impact on the seismic image and therefore a better definition of the fault architecture (Figure 12 of paper 3).

Seismic acquisition parameters strongly control the vertical and horizontal resolution of the fault. While vertical seismic resolution can mask thin layers or small displacement faults, the horizontal resolution will affect the interpretation of the fault as a volume. Wave frequency is the parameter that influences the most the resolution through our studies (papers 1 to 3). Papers 1 and 2 show that the lower the frequency, the higher the tendency to interpret the fault as a surface. Indeed, for wave frequencies lower than 20 Hz, the fault lateral extent is below the horizontal resolution of the seismic, i.e. 100 to 200 m according to the PSFs, and all the images look alike as there are no diffractions or other features that can help to define the fault volume. Based on the reflectors offsets, one would interpret the fault as a plane. However, this would be wrong, because the fault volume can still be interpreted. Papers 2 and 3 show that not only the break of reflectors, but also their changes in azimuth and dip around the fault core, where the hanging wall and footwall reflectors interact, are due to fault damage. Figure 8a illustrates that the 150 m wide fault zone can be directly interpreted on the map view of the 10 Hz seismic cube. Figure 8b shows the extracted geobody from the 20 Hz seismic cube at the end of the fluid flow simulation in the Delicate Arch Ramp (paper 3). This geobody is less regular than the one from the 40 Hz seismic cube (Figure 10 in paper 3), but still it indicates approximately the faults even if there are no visible breaks in the reflectors on the seismic section. Even though overestimated, the thickness of the fault zone can also be defined from the width of the RMS amplitude fluctuation in the 2D coarse model (paper 1; Figure 8c). The illumination direction has a strong effect on how faults can be imaged on seismic, especially in 2D (paper 1), and other parameters such as the overburden complexity, or the depth of investigation also greatly influence the resolution and the definition of the fault. With a priori knowledge of the

surrounding geological environment, it is therefore possible to anticipate the seismic signature of the in situ faults and to adequately tune acquisition parameters for a better illumination of their volumes.

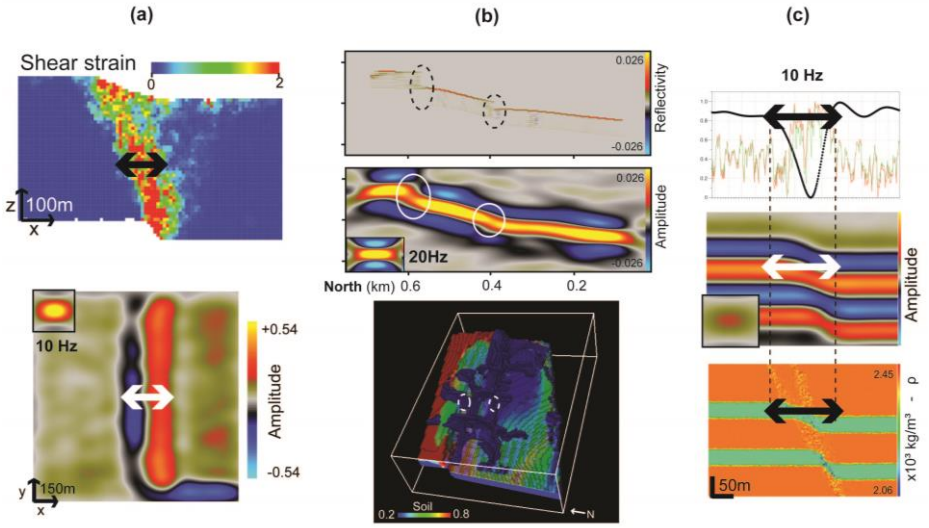

Figure 8: *(a) Example from 3D DEM constant displacement fault model: Shear strain in dip section and depth slice for the 10 Hz cube (paper 2). The arrows indicate the fault thickness. (b) Reflectivity, 20 Hz seismic section, and geobody volume at the end of the flow simulation in the Delicate Arch ramp. The ellipses represent the fault zone. (c) The fault thickness (arrows) in the seismic image at 10 Hz and input density section of the 2D DEM coarse model. The PSFs are displayed on the seismic images.*

7.4 Limitations

One of the weakest steps of our methodology is the one involving the empirical relationships used to compute the changes of elastic properties due to finite strain (Figure 5). Couples et al. (2007) used finite strain as the primary parameter for describing changes of rock properties inside a fault zone. They populated a mechanical FEM model of a normal fault using simple strain-based relationships and managed to illuminate these changes on synthetic seismic. Sigernes (2004) and Alaei and Petersen (2007) made a considerable effort defining accurately the rock elastic properties in fault zones by using outcrop

(Sigernes, 2004) or well-log data (Alaei and Petersen, 2007). However, the distribution of properties within the fault zone used by Sigernes (2004) as input for the seismic modelling was either linear or symmetric around a fault core. Alaei and Petersen (2007) targeted larger scale (tens of km) fault-related folding and did not concentrate on the fault volume definition but rather on the general structure of the fold. Therefore, their synthetic seismograms did not provide specific insights for seismic characterisation of fault zone properties. Our relationships are also approximate but they are a necessary first step for converting fault damage to the distribution of elastic properties for seismic modelling. Future experiments and models on rock physics at very large strains, like those of faulting, will certainly improve our work.

During this work, we have produced several models of faults, but only targeted normal faulting in siliciclastic sequences that are purely frictional. In the DEM models, we are also limited by the particle sizes, which make it difficult to introduce more complex sequences with thinner layers. In the outcrop-based geocellular model, we need to upscale the rock properties and deformations observed in the field to Dm-size cells in order to run the flow simulation. Thus, due to computational and model limitations, we are not able to investigate faulting at very fine grain-size scale. However, our geomechanical and outcrop-based models are still good examples of faults at reservoir conditions, and can be used to test the characterisation of complex fault structures and properties in seismic data.

Although, in our workflow we have an exact knowledge of the input fault geometry and rock properties, we did not test the inversion of the seismic data for these properties. Our cross-plots are proxies for the distribution of rock properties in the fault zone. However, in order to derive from the seismic the fault properties, one would need a better understanding of rock physics at large strains, and probably more information from well data and localised seismic surveys, to run the seismic inversions. We modelled the impact on elastic properties of fluid flow in a relay ramp using simple relationships (Gassmann theory) in paper 3, however cross-fault flow and fluid-induced deformation can affect elastic properties and seismic images in a more complex way (e.g., Mavko et al., 2009; Manzocchi et al., 2010; Pei et al., 2015). Taking into account these effects will certainly result in more realistic forward simulations.

Even though PSDM is the ultimate goal of seismic processing, it might not always be available for seismic data, as it needs an adequate velocity model that can be hard to retrieve in certain conditions. Moreover, many inversion techniques are based on post-stack time-migrated seismic data. With the PSDM simulator, we are therefore limited in the testing of other processing techniques or in reproducing some seismic datasets in complex tectonic setting, such as those of Alaei and Petersen (2007).

7.5 Implications

Despite the limitations above, we have introduced an interdisciplinary workflow that establishes a link between geology, geophysics, rock physics and reservoir engineering. We describe interpretation routines to accurately retrieve fault input architecture and petrophysical properties from seismic data. The success of these routines depends on the interpreter's understanding of the geology and mechanical processes behind faulting and rock properties. Moreover, the workflow can help the geophysicist to handle seismic processing or to run seismic acquisition with the objective of illuminating faults. The methodology also demands that the reservoir engineer, the rock physicist and the petrophysicist find better ways to link the elastic properties to the fault-related deformations, as function of lithology and fluids.

Our methodology is general enough to be applied to several research purposes. By providing ways to better outline fault architecture, we improve the definition of reservoir compartmentalisation. Our workflow can be varied to include several fluid compositions and saturation conditions. This is important for hydrocarbon exploration and production (e.g. Wibberley et al., 2008; Manzocchi et al., 2010; Pei et al., 2015), and storage of subsurface waste (e.g. CO_2; Dockrill and Shipton, 2010; Dutzer et al., 2010; Wilson et al., 2012; Tillner et al., 2013). Seismic characterisation of faults is also important for understanding the flow of hydrothermal fluids in geothermal areas (e.g. Brogi, 2008; Vargemezis, 2014), or the impact of faulting on groundwater flow (Bense et al., 2013).

8 Perspectives – Future work

In order to improve our knowledge of the impact of faulting on elastic properties and seismic images, further sensitivity analyses could be run, in addition to those applied for the porosity and permeability in paper 3. Such analyses would vary V_P more or less significantly while keeping the density constant, or the other way around. Based on these analyses, we could establish realistic ranges of density and seismic velocities that could have an impact on the seismic images at given reservoir conditions.

To widen the application of the workflow, we could investigate fault models in more complex settings, such as fold-and-thrust-belts (e.g. Alaei and Petersen, 2007; Iacopini and Butler, 2011; Iacopini et al., 2012) or salt-controlled faulting. Varying the lithology to include e.g. carbonate rocks, salt or coal, and the geological sequences to target some real exploration areas could help to produce analogue models for specific reservoir characterisation. Moreover studying several stages of fault formation, fault-related folding, and fault reactivation will give new insights for seismic characterisation of reservoir connectivity and better constrains for reservoir models.

Applying this workflow to real production and seismic data, or to real reservoir scenarios is a necessary step for validating our seismic-attribute routines. In order to vary the seismic response of one given structure, FD-based forward seismic modelling could be used. By doing so, we could introduce noise or multiples to the seismic data in order to match acquired seismic data, and to run several processing methods to investigate their impact on the fault image.

Ongoing research by two MSc students at the University of Stavanger applies our workflow to 2D DEM models of salt-related deformation in siliciclastics, in compressional and extensional settings. SEISBARS (Seismic Expression of Fault and Fracture Zones in Barents Sea Petroleum Reservoirs) project (NORRUSS and Norwegian Research Council Grant no. 233646) intends to map the seismic response of a matrix of realistic fault zone models, populated through fault-facies techniques (Qu et al., 2015) in order to establish how specific fault zone features and properties affect the seismic signal, using both the PSDM simulator and FD techniques (Kolyukhin et al., 2015).

9 References

Aarland, R. K., and J. Skjerven, 1998, Fault and fracture characteristics of a major fault zone in the northern North Sea: analysis of 3D seismic and oriented cores in the Brage Field (Block 31/4): p. 209–229.

Abe, S., and K. Mair, 2005, Grain fracture in 3D numerical simulations of granular shear: Geophysical Research Letters, v. 32, no. 5, p. L05305, doi:10.1029/2004GL022123.

Alaei, B., 2006, Seismic depth imaging of complex structures An example from Zagros fold and thrust belt, Iran: PhD dissertation, University of Bergen, 73 p.

Alaei, B., 2012, Seismic Modeling of Complex Geological Structures, Seismic Waves - Research and Analysis, *in* M. Kanao, ed.: InTech, doi:10.5772/1400.

Alaei, B., and S. A. Petersen, 2007, Geological modelling and finite difference forward realization of a regional section from the Zagros fold-and-thrust belt: Petroleum Geoscience, v. 13, no. 3, p. 241–251, doi:10.1144/1354-079306-730.

Bahorich, M., and S. Farmer, 1995, 3-D seismic discontinuity for faults and stratigraphic features: The coherence cube: The Leading Edge, v. 14, no. 10, p. 1053–1058.

Barnes, A. E., 2000, Weighted average seismic attributes: GEOPHYSICS, v. 65, no. 1, p. 275–285, doi:10.1190/1.1444718.

Bastesen, E., and A. Braathen, 2010, Extensional faults in fine grained carbonates – analysis of fault core lithology and thickness–displacement relationships: Journal of Structural Geology, v. 32, no. 11, p. 1609–1628, doi:10.1016/j.jsg.2010.09.008.

Belheine, N., J. P. Plassiard, F. V Donzé, F. Darve, and A. Seridi, 2009, Numerical simulation of drained triaxial test using 3D discrete element modeling: Computers and Geotechnics, v. 36, no. 1-2, p. 320–331, doi:10.1016/j.compgeo.2008.02.003.

Benesh, N. P., A. Plesch, J. H. Shaw, and E. K. Frost, 2007, Investigation of growth fault bend folding using discrete element modeling: Implications

for signatures of active folding above blind thrust faults: Journal of Geophysical Research, v. 112, no. B3, p. B03S04, doi:10.1029/2006JB004466.

Bense, V. F., T. Gleeson, S. E. Loveless, O. Bour, and J. Scibek, 2013, Fault zone hydrogeology: Earth-Science Reviews, v. 127, p. 171–192, doi:10.1016/j.earscirev.2013.09.008.

Ben-Zion, Y., and C. G. Sammis, 2003, Characterization of fault zones: Pure and Applied Geophysics, v. 160, no. 3-4, p. 677–715.

Botter, C., N. Cardozo, S. Hardy, I. Lecomte, and A. Escalona, 2014, From mechanical modeling to seismic imaging of faults: A synthetic workflow to study the impact of faults on seismic: Marine and Petroleum Geology, v. 57, p. 187–207, doi:10.1016/j.marpetgeo.2014.05.013.

Brogi, A., 2008, Fault zone architecture and permeability features in siliceous sedimentary rocks: Insights from the Rapolano geothermal area (Northern Apennines, Italy): Journal of Structural Geology, v. 30, no. 2, p. 237–256, doi:10.1016/j.jsg.2007.10.004.

Brown, A. R., 2010, Interpretation of three-dimensional seismic data, Seventh Edition: AAPG Memoir, and SEG Investigations in Geophysics, v. 42, no. 9.

Buckley, S. J., J. A. Howell, H. D. Enge, and T. H. Kurz, 2008, Terrestrial laser scanning in geology: data acquisition, processing and accuracy considerations: Journal of the Geological Society, v. 165, no. 3, p. 625–638, doi:10.1144/0016-76492007-100.

Buiter, S. J. H., A. Y. Babeyko, S. Ellis, T. V Gerya, B. J. P. Kaus, A. Kellner, G. Schreurs, and Y. Yamada, 2006, The numerical sandbox: Comparison of model results for a shortening and an extension experiment: p. 29–64.

Butler, R. W. ., and W. . McCaffrey, 2004, Nature of thrust zones in deep water sand-shale sequences: outcrop examples from the Champsaur sandstones of SE France: Marine and Petroleum Geology, v. 21, no. 7, p. 911–921, doi:10.1016/j.marpetgeo.2003.07.005.

Caine, J. S., J. P. Evans, and C. B. Forster, 1996, Fault zone architecture and permeability structure: Geology, v. 24, no. 11, p. 1025–1028, doi:10.1130/0091-7613(1996)024.

Carcione, J. M., G. C. Herman, and A. P. E. ten Kroode, 2002, Seismic modeling: GEOPHYSICS, v. 67, no. 4, p. 1304–1325, doi:10.1190/1.1500393.

Cardozo, N., and R. W. Allmendinger, 2009, SSPX: A program to compute strain from displacement/velocity data: Computers and Geosciences, v. 35, no. 6, p. 1343–1357, doi:10.1016/j.cageo.2008.05.008.

Cardozo, N., R. W. Allmendinger, and J. K. Morgan, 2005, Influence of mechanical stratigraphy and initial stress state on the formation of two fault propagation folds: Journal of Structural Geology, v. 27, no. 11, p. 1954–1972, doi:10.1016/j.jsg.2005.06.003.

Cardozo, N., K. Bhalla, A. T. Zehnder, and R. W. Allmendinger, 2003, Mechanical models of fault propagation folds and comparison to the trishear kinematic model: Journal of Structural Geology, v. 25, no. 1, p. 1–18, doi:10.1016/S0191-8141(02)00013-5.

Chehrazi, A., H. Rahimpour-Bonab, and M. R. Rezaee, 2013, Seismic data conditioning and neural network-based attribute selection for enhanced fault detection: Petroleum Geoscience, v. 19, no. 2, p. 169–183, doi:10.1144/petgeo2011-001.

Childs, C., T. Manzocchi, J. J. Walsh, C. G. Bonson, A. Nicol, and M. P. J. Schöpfer, 2009, A geometric model of fault zone and fault rock thickness variations: Journal of Structural Geology, v. 31, no. 2, p. 117–127, doi:10.1016/j.jsg.2008.08.009.

Childs, C., J. Watterson, and J. J. Walsh, 1996, A model for the structure and development of fault zones: Journal of the Geological Society, v. 153, no. 3, p. 337–340, doi:10.1144/gsjgs.153.3.0337.

Chopra, S., and K. Marfurt, 2007, Curvature attribute applications to 3D surface seismic data: The Leading Edge, v. 26, no. 4, p. 404–414.

Chopra, S., and K. J. Marfurt, 2005, Seismic attributes - A historical perspective: Geophysics, v. 70, no. 5, p. 3SO–28SO, doi:10.1190/1.2098670.

Chopra, S., and K. Marfurt, 2007, Seismic attributes for prospect identification and reservoir characterization: SEG Geophysical Developments Series No. 11, v. 2, no. 9.

Chopra, S., V. Sudhakar, G. Larsen, and H. Leong, 2000, Azimuth-based coherence for detecting faults and fractures: World Oil, v. 221, no. 9, p. 57–62.

Couples, G., J. Ma, H. Lewis, P. Olden, J. Quijano, T. Fasae, and R. Maguire, 2007, Geomechanics of faults: Impacts on seismic imaging: First Break, v. 25, no. 10, p. 83–90.

Cundall, P., and O. Strack, 1979, A discrete numerical model for granular assemblies: Géotechnique, v. 29, no. 1, p. 47–65.

Davatzes, N. C., and A. Aydin, 2005, Distribution and nature of fault architecture in a layered sandstone and shale sequence: An example from the Moab fault, Utah: AAPG Memoir, no. 85, p. 153–180, doi:10.1306/1033722m853134.

Dockrill, B., and Z. K. Shipton, 2010, Structural controls on leakage from a natural CO2 geologic storage site: Central Utah, U.S.A.: Journal of Structural Geology, v. 32, no. 11, p. 1768–1782, doi:10.1016/j.jsg.2010.01.007.

Dutzer, J.-F., H. Basford, and S. Purves, 2010, Investigating fault-sealing potential through fault relative seismic volume analysis: Petroleum Geology Conference series, v. 7, p. 509–515.

Egholm, D. L., O. R. Clausen, M. Sandiford, M. B. Kristensen, and J. A. Korstgård, 2008, The mechanics of clay smearing along faults: Geology, v. 36, no. 10, p. 787–790.

Egholm, D. L., M. Sandiford, O. R. Clausen, and S. B. Nielsen, 2007, A new strategy for discrete element numerical models: 2. Sandbox applications: Journal of Geophysical Research: Solid Earth, v. 112, no. B5, p. B05204, doi:10.1029/2006jb004558.

Eichhubl, P., P. S. D'Onfro, A. Aydin, J. Waters, and D. K. McCarty, 2005, Structure, petrophysics, and diagenesis of shale entrained along a normal fault at Black Diamond Mines, California—Implications for fault seal: AAPG Bulletin, v. 89, no. 9, p. 1113–1137, doi:10.1306/04220504099.

Fachri, M., A. Rotevatn, and J. Tveranger, 2013, Fluid flow in relay zones revisited: Towards an improved representation of small-scale structural heterogeneities in flow models: Marine and Petroleum Geology, v. 46, p. 144–164, doi:10.1016/j.marpetgeo.2013.05.016.

Fagin, S., 1996, The fault shadow problem: Its nature and elimination: The Leading Edge, v. 15, no. 9, p. 1005–1013, doi:10.1190/1.1437403.

Faulkner, D. R., C. A. L. Jackson, R. J. Lunn, R. W. Schlische, Z. K. Shipton, C. A. J. Wibberley, and M. O. Withjack, 2010, A review of recent developments concerning the structure, mechanics and fluid flow properties of fault zones: Journal of Structural Geology, v. 32, no. 11, p. 1557–1575, doi:10.1016/j.jsg.2010.06.009.

Fehmers, G. C., and C. F. W. Höcker, 2003, Fast structural interpretation with structure- oriented filtering: GEOPHYSICS, v. 68, no. 4, p. 1286–1293, doi:10.1190/1.1598121.

Finch, E., S. Hardy, and R. Gawthorpe, 2003, Discrete element modelling of contractional fault-propagation folding above rigid basement fault blocks: Journal of Structural Geology, v. 25, no. 4, p. 515–528, doi:10.1016/S0191-8141(02)00053-6.

Finch, E., S. Hardy, and R. Gawthorpe, 2004, Discrete-element modelling of extensional fault-propagation folding above rigid basement fault blocks: Basin Research, v. 16, no. 4, p. 489–506, doi:10.1111/j.1365-2117.2004.00241.x.

Fisher, Q. J., and S. J. Jolley, 2007, Treatment of faults in production simulation models: Geological Society, London, Special Publications, v. 292, no. 1, p. 219–233, doi:10.1144/SP292.13.

Fisher, Q. J., and R. J. Knipe, 2001, The permeability of faults within siliciclastic petroleum reservoirs of the North Sea and Norwegian Continental Shelf: Marine and Petroleum Geology, v. 18, no. 10, p. 1063–1081.

Foxford, K. A., J. J. Walsh, J. Watterson, I. R. Garden, S. C. Guscott, and S. D. Burley, 1998, Structure and content of the Moab Fault Zone, Utah, USA, and its implications for fault seal prediction: p. 87–103.

Gersztenkorn, A., and K. J. Marfurt, 1999, Eigenstructure- based coherence computations as an aid to 3-D structural and stratigraphic mapping: GEOPHYSICS, v. 64, no. 5, p. 1468–1479, doi:10.1190/1.1444651.

Gray, G. G., J. K. Morgan, and P. F. Sanz, 2014, Overview of continuum and particle dynamics methods for mechanical modeling of contractional geologic structures: Journal of Structural Geology, v. 59, no. 0, p. 19–36,

doi:http://dx.doi.org/10.1016/j.jsg.2013.11.009.

Gregg Erickson, S., and W. R. Jamison, 1995, Viscous-plastic finite-element models of fault-bend folds: Journal of Structural Geology, v. 17, no. 4, p. 561–573, doi:10.1016/0191-8141(94)00082-B.

Han, D., 1986, Effects of porosity and clay content on acoustic properties of sandstones and uncosolidated sediments: PhD Thesis. Stanford University, Department of Geophysics, School of Earth Sciences.

Hardy, S., 2011, Cover deformation above steep, basement normal faults: Insights from 2D discrete element modeling: Marine and Petroleum Geology, v. 28, no. 5, p. 966–972, doi:10.1016/j.marpetgeo.2010.11.005.

Hardy, S., 2013, Propagation of blind normal faults to the surface in basaltic sequences: Insights from 2D discrete element modelling: Marine and Petroleum Geology, v. 48, p. 149–159.

Hardy, S., 2008, Structural evolution of calderas: insights from two-dimensional discrete element simulations: Geology, v. 36, no. 12, p. 927–930.

Hardy, S., and E. Finch, 2006, Discrete element modelling of the influence of cover strength on basement-involved fault-propagation folding: Tectonophysics, v. 415, no. 1-4, p. 225–238, doi:10.1016/j.tecto.2006.01.002.

Hardy, S., and E. Finch, 2005, Discrete-element modelling of detachment folding: Basin Research, v. 17, no. 4, p. 507–520, doi:10.1111/j.1365-2117.2005.00280.x.

Hardy, S., K. McClay, and J. Anton Muñoz, 2009, Deformation and fault activity in space and time in high-resolution numerical models of doubly vergent thrust wedges: Marine and Petroleum Geology, v. 26, no. 2, p. 232–248, doi:10.1016/j.marpetgeo.2007.12.003.

Hatchell, P., and S. Bourne, 2005, Rocks under strain: Strain-induced time-lapse time shifts are observed for depleting reservoirs: Leading Edge (Tulsa, OK), v. 24, no. 12, p. 1222–1225, doi:10.1190/1.2149624.

Healy, D., J. E. Neilson, T. J. Haines, Michie, N. E. Timms, and M. E. J. Wilson, 2014, An investigation of porosity-velocity relationships in faulted carbonates using outcrop analogues: Geological Society Special

Publication, v. 406, p. 261–280, doi:10.1144/SP406.13.

Hesthammer, J., and H. Fossen, 1997, Research article: The influence of seismic noise in structural interpretation of seismic attribute maps: First Break, v. 15, no. 1024, p. 209–219, doi:10.3997/1365-2397.1997007.

Hesthammer, J., and J. O. Henden, 2000, Closing the gap between theory and practice in seismic interpretation of small-scale faults: Petroleum Geoscience, v. 6, no. 2, p. 107–111.

Hoek, E., and E. T. Brown, 1997, Practical estimates of rock mass strength: International Journal of Rock Mechanics and Mining Sciences, v. 34, no. 8, p. 1165–1186.

Holohan, E. P., M. P. J. Schöpfer, and J. J. Walsh, 2011, Mechanical and geometric controls on the structural evolution of pit crater and caldera subsidence: Journal of Geophysical Research B: Solid Earth, v. 116, no. 7.

Holt, R. M., E. Fjær, O. M. Nes, and J. F. Stenebråten, 2008, Strain sensitivity of wave velocities in sediments and sedimentary rocks, *in* 42nd US Rock Mechanics Symposium and 2nd U.S.-Canada Rock Mechanics Symposium: American Rock Mechanics Association.

Horsrud, P., E. F. Sønsteb Ø, and R. Bøe, 1998, Mechanical and petrophysical properties of North Sea shales: International Journal of Rock Mechanics and Mining Sciences, v. 35, no. 8, p. 1009–1020.

Hubbert, M. K., 1951, Mechanical Basis For Certain Familiar Geological Structures: Geological Society of America Bulletin, v. 62, no. 4, p. 355, doi:10.1130/0016-7606(1951)62.

Höcker, C., and G. Fehmers, 2002, Fast structural interpretation with structure-oriented filtering: The Leading Edge, v. 21, no. 3, p. 238–243, doi:10.1190/1.1463775.

Iacopini, D., and R. W. H. Butler, 2011, Imaging deformation in submarine thrust belts using seismic attributes: Earth and Planetary Science Letters, v. 302, no. 3–4, p. 414–422, doi:10.1016/j.epsl.2010.12.041.

Iacopini, D., R. W. H. Butler, and S. Purves, 2012, Seismic imaging of thrust faults and structural damage: a visualization workflow for deepwater thrust belts: First Break, v. 30, no. 5, p. 77–84.

Jackson, C. A. L., and K. E. Kane, 2012, 3D Seismic Interpretation Techniques: Applications to Basin Analysis, *in* Tectonics of Sedimentary Basins: Recent Advances: John Wiley and Sons, p. 95–110, doi:10.1002/9781444347166.ch5.

Jeanne, P., Y. Guglielmi, and F. Cappa, 2012, Multiscale seismic signature of a small fault zone in a carbonate reservoir: Relationships between VP imaging, fault zone architecture and cohesion: Tectonophysics, v. 554–557, no. 0, p. 185–201, doi:10.1016/j.tecto.2012.05.012.

Joergensen, H., and B. Alaei, 2015, Application of Seismic Attribute Volumes for Detailed Interpretation of Fault Interactions and Growth, *in* 4th International Conference on Fault and Top Seals 2015: EAGE.

Jolley, S. J., H. Dijk, J. H. Lamens, Q. J. Fisher, T. Manzocchi, H. Eikmans, and Y. Huang, 2007, Faulting and fault sealing in production simulation models: Brent Province, northern North Sea: Petroleum Geoscience, v. 13, no. 4, p. 321–340, doi:10.1144/1354-079306-733.

Kalkomey, C. T., 1997, Potential risks when using seismic attributes as predictors of reservoir properties: The Leading Edge, v. 16, no. 3, p. 247–251, doi:10.1190/1.1437610.

Koledoye, B. A., A. Aydin, and E. May, 2003, A new process-based methodology for analysis of shale smear along normal faults in the Niger Delta: AAPG Bulletin, v. 87, no. 3, p. 445–463.

Kolyukhin, D., V. Lisitsa, D. Qu, M. Protasov, V. Tcheverda, J. Tveranger, and D. Vishnevsky, 2015, Seismic imaging of fault facies models - A pilot study, *in* 4th International Conference on Fault and Top Seals 2015: European Association of Geoscientists and Engineers, EAGE, p. 95–99.

Krebes, E., 2004, Seismic forward modeling: CSEG Recorder, v. 30, p. 28–39.

Lecomte, I., 2008, Resolution and illumination analyses in PSDM: A ray-based approach: Leading Edge (Tulsa, OK), v. 27, no. 5, p. 650–663, doi:10.1190/1.2919581.

Lecomte, I., H. Gjøystdal, and Å. Drottning, 2003, Simulated Prestack Local Imaging: a Robust And Efficient Interpretation Tool to Control Illumination, Resolution, And Time-lapse Properties of Reservoirs., *in* 2003 SEG Annual Meeting: Society of Exploration Geophysicists.

Lecomte, I., and T. Kaschwich, 2008, Closer to Real Earth In Reservoir Characterization: a 3D Isotropic/anisotropic PSDM Simulator, *in* SEG Technical Program Expanded Abstracts: Society of Exploration Geophysicists.

Lecomte, I., P. L. Lavadera, I. Anell, S. J. Buckley, D. W. Schmid, and M. Heeremans, 2015, Ray-based seismic modeling of geologic models: Understanding and analyzing seismic images efficiently: Interpretation, v. 3, no. 4, p. SAC71–SAC89.

Lewis, M. A., Z. Peng, Y. Ben-Zion, and F. L. Vernon, 2005, Shallow seismic trapping structure in the San Jacinto fault zone near Anza, California: Geophysical Journal International, v. 162, no. 3, p. 867–881.

Long, J. J., and J. Imber, 2010, Geometrically coherent continuous deformation in the volume surrounding a seismically imaged normal fault-array: Journal of Structural Geology, v. 32, no. 2, p. 222–234, doi:10.1016/j.jsg.2009.11.009.

Long, J. J., and J. Imber, 2012, Strain compatibility and fault linkage in relay zones on normal faults: Journal of Structural Geology, v. 36, p. 16–26, doi:10.1016/j.jsg.2011.12.013.

MacBeth, C., K. D. Stephen, and A. McInally, 2005, The 4D seismic signature of oil-water contact movement due to natural production in a stacked turbidite reservoir: Geophysical Prospecting, v. 53, no. 2, p. 183–203, doi:10.1111/j.1365-2478.2004.00463.x.

Manzocchi, T., C. Childs, and J. J. Walsh, 2010, Faults and fault properties in hydrocarbon flow models: Geofluids, v. 10, no. 1-2, p. 94–113, doi:10.1111/j.1468-8123.2010.00283.x.

Marfurt, K. J., 2006, Robust estimates of 3D reflector dip and azimuth: Geophysics, v. 71, no. 4, p. P29–P40, doi:10.1190/1.2213049.

Marfurt, K. J., and T. M. Alves, 2015, Pitfalls and limitations in seismic attribute interpretation of tectonic features: Interpretation, v. 3, no. 1, p. SB5–SB15, doi:10.1190/INT-2014-0122.1.

Mascolo, V., G. Rusciadelli, and I. Lecomte, 2015, Synthetic Seismic Modelling of Outcropping Carbonate System of the Maiella Mountain (Central Apennines-Italy), *in* 77th EAGE Conference and Exhibition 2015.

Mavko, G., T. Mukerji, and J. Dvorkin, 2009, The rock physics handbook: Tools for seismic analysis of porous media: 329 p.

Mora, P., and D. Place, 1993, A lattice solid model for the nonlinear dynamics of earthquakes: International Journal of Modern Physics C, v. 04, no. 06, p. 1059–1074, doi:10.1142/s0129183193000823.

Nes, O.-M., R. M. Holt, and E. Fjær, 2000, The Reliability of Core Data as Input to Seismic Reservoir Monitoring Studies, *in* SPE European Petroleum Conference: Society of Petroleum Engineers, doi:10.2118/65180-MS.

Nicolaisen, E. M., 2009, Seismic characterization of fault zones for use in fault facies reservoir models: MSc Thesis, University of Stavanger, Norway, 66 p.

Niño, F., H. Philip, and J. Chéry, 1998, The role of bed-parallel slip in the formation of blind thrust faults: Journal of Structural Geology, v. 20, no. 5, p. 503–516, doi:10.1016/S0191-8141(97)00102-8.

Nygård, R., M. Gutierrez, R. K. Bratli, and K. Høeg, 2006, Brittle-ductile transition, shear failure and leakage in shales and mudrocks: Marine and Petroleum Geology, v. 23, no. 2, p. 201–212, doi:10.1016/j.marpetgeo.2005.10.001.

Pei, Y., D. A. Paton, R. J. Knipe, and K. Wu, 2015, A review of fault sealing behaviour and its evaluation in siliciclastic rocks: Earth-Science Reviews, v. 150, p. 121–138, doi:10.1016/j.earscirev.2015.07.011.

Perona, P., and J. Malik, 1990, Scale-space and edge detection using anisotropic diffusion: Pattern Analysis and Machine Intelligence, ….

Place, D., and P. Mora, 1999, The lattice solid model to simulate the physics of rocks and earthquakes: incorporation of friction: Journal of Computational Physics, v. 150, no. 2, p. 332–372, doi:10.1006/jcph.1999.6184.

Qu, D., P. Røe, and J. Tveranger, 2015, A method for generating volumetric fault zone grids for pillar gridded reservoir models: Computers & Geosciences, v. 81, p. 28–37, doi:10.1016/j.cageo.2015.04.009.

Robinson, E. A., and S. Treitel, 1978, The Fine Structure of the Normal Incidence Synthetic Seismogram: Geophysical Journal International, v.

53, no. 2, p. 289–309, doi:10.1111/j.1365-246X.1978.tb03743.x.

Rotevatn, A., S. J. Buckley, J. A. Howell, and H. Fossen, 2009, Overlapping faults and their effect on fluid flow in different reservoir types: A LIDAR-based outcrop modeling and flow simulation study: AAPG Bulletin, v. 93, no. 3, p. 407–427.

Rotevatn, A., and H. Fossen, 2011, Simulating the effect of subseismic fault tails and process zones in a siliciclastic reservoir analogue: Implications for aquifer support and trap definition: Marine and Petroleum Geology, v. 28, no. 9, p. 1648–e1662.

Rotevatn, A., H. Fossen, J. Hesthammer, T. E. Aas, and J. A. Howell, 2007, Are relay ramps conduits for fluid flow? Structural analysis of a relay ramp in Arches National Park, Utah: p. 55–71.

Sanz, P. F., R. I. Borja, and D. D. Pollard, 2007, Mechanical aspects of thrust faulting driven by far-field compression and their implications for fold geometry: Acta Geotechnica, v. 2, no. 1, p. 17–31, doi:10.1007/s11440-007-0025-0.

Sayers, C., and S. Chopra, 2009, Introduction to this special section: Seismic modeling: The Leading Edge, v. 28, no. 5, p. 528–529, doi:10.1190/1.3124926.

Schueller, S., A. Braathen, H. Fossen, and J. Tveranger, 2013, Spatial distribution of deformation bands in damage zones of extensional faults in porous sandstones: Statistical analysis of field data: Journal of Structural Geology, v. 52, p. 148–162, doi:10.1016/j.jsg.2013.03.013.

Schöpfer, M. P. J., C. Childs, and J. J. Walsh, 2007, Two-dimensional distinct element modeling of the structure and growth of normal faults in multilayer sequences: 1. Model calibration, boundary conditions, and selected results: Journal of Geophysical Research B: Solid Earth, v. 112, no. 10, doi:10.1029/2006jb004902.

Sheriff, R. E., and L. P. Geldart, 1995, Exploration Seismology: Cambridge Univ Press.

Shtivelman, V., S. Marco, M. Reshef, A. Agnon, and Y. Hamiel, 2005, Using trapped waves for mapping shallow fault zones: Near Surface Geophysics, v. 3, no. 2, p. 91–97.

Sigernes, L., 2004, Rock Physics of extensional Faults and their seismic imaging Properties: Dissertation, PhD, 366 p.

Skurtveit, E., A. Torabi, R. H. Gabrielsen, and M. D. Zoback, 2013, Experimental investigation of deformation mechanisms during shear-enhanced compaction in poorly lithified sandstone and sand: Journal of Geophysical Research: Solid Earth, v. 118, no. 8, p. 4083–4100, doi:10.1002/jgrb.50342.

Solum, J. G., N. C. Davatzes, and D. A. Lockner, 2010, Fault-related clay authigenesis along the Moab Fault: Implications for calculations of fault rock composition and mechanical and hydrologic fault zone properties: Journal of Structural Geology, v. 32, no. 12, p. 1899–1911, doi:10.1016/j.jsg.2010.07.009.

Stockwell, J., and J. Cohen, 2002, The New SU User's Manual version 3.2: Colorado School of Mines Golden, CO.

Strayer, L. M., and J. S. , S. Gregg Erickson, 2004, Influence of Growth Strata on the Evolution of Fault-related Folds— Distinct-element Models: p. 413–437.

Taner, M., 2001, Seismic attributes: CSEG recorder, v. 26, p. 48–56.

Terheege, J. H., B. B. T. Wassing, B. Orlic, S. B. Giger, and M. B. Clennell, 2013, Constraints on the sealing capacity of faults with clay smears from discrete element models validated by laboratory experiments: Rock Mechanics and Rock Engineering, v. 46, no. 3, p. 465–478, doi:10.1007/s00603-013-0383-x.

Tillner, E., T. Kempka, B. Nakaten, and M. Kühn, 2013, Brine migration through fault zones: 3D numerical simulations for a prospective CO2 storage site in Northeast Germany: International Journal of Greenhouse Gas Control, v. 19, p. 689–703, doi:10.1016/j.ijggc.2013.03.012.

Townsend, C., I. R. Firth, R. Westerman, L. Kirkevollen, M. Hårde, and T. Andersen, 1998, Small seismic-scale fault identification and mapping, *in* G. S. S. Publication, ed., JONES, G., FISHER, Q. J. & KNIPE, R. J. (eds) Faulting, Fault Sealing and Fluid Flow in Hydrocarbon Reservoirs.: Geological Society, London, Special Publications, v. 147, p. 1–25.

Vargemezis, G., 2014, 3D geoelectrical model of geothermal spring mechanism derived from VLF measurements: A case study from Aggistro (Northern

Greece): Geothermics, v. 51, p. 1–8, doi:10.1016/j.geothermics.2013.09.001.

Weickert, J., 1998, Anisotropic diffusion in image processing.

Wibberley, C. A. J., G. Yielding, and G. Di Toro, 2008, Recent advances in the understanding of fault zone internal structure: A review, *in* C. A. J. Wibberley, W. Kurz, J. Imber, R. E. Holdsworth, and C. Collettini, eds., (eds) The Internal Structure of Fault Zones: Implications for Mechanical and Fluid-Flow Properties.: Geological Society, London, Special Publications, v. 299, p. 5–33.

Williams, G., and T. Chapman, 1983, Strains developed in the hangingwalls of thrusts due to their slip/propagation rate: A dislocation model: Journal of Structural Geology, v. 5, no. 6, p. 563–571, doi:10.1016/0191-8141(83)90068-8.

Wilson, T. H., A. Wells, D. Peters, A. Mioduchowski, G. Martinez, G. Koperna, B. N. Akwari, and J. Heath, 2012, Fracture and 3D seismic interpretations of the Fruitland Formation and cover strata: Implications for CO2 retention and tracer movement, San Juan Basin Pilot test: International Journal of Coal Geology, v. 99, p. 35–53, doi:10.1016/j.coal.2012.02.007.

Wood, A. M., D. A. Paton, and R. E. L. L. Collier, 2015, The missing complexity in seismically imaged normal faults: What are the implications for geometry and production response?, *in* Richards, F. L., Richardson, N. J., Rippington, S. J.,Wilson,R.W.&Bond, C. E. (eds) 2015. Industrial Structural Geology: Principles, Techniques and Integration.: Geological Society of London, Special Publications, v. 421, p. 213–230, doi:10.1144/SP421.12.

Zhang, J., J. K. Morgan, G. G. Gray, N. W. Harkins, P. F. Sanz, and I. Chikichev, 2013, Comparative FEM and DEM modeling of basement-involved thrust structures, with application to Sheep Mountain, Greybull area, Wyoming: Tectonophysics, v. 608, no. 0, p. 408–417, doi:http://dx.doi.org/10.1016/j.tecto.2013.09.006.

Zhou, G., W. B. Lei, and J. H. Zhang, 2012, Application of Fault Detection Using Ant-Tracking Algorithm: Daqing Oilfield Example: Advanced Materials Research, v. 459, p. 406–410.

Zoback, M. D., 2010, Reservoir geomechanics: Cambridge University Press, 461 p.

Chapter 2

Compilation of papers

1

PAPER 1

From mechanical modeling to seismic imaging of faults: A synthetic workflow to study the impact of fault on seismic

Botter, Charlotte; Cardozo, Nestor; Hardy, Stuart; Lecomte, Isabelle & Escalona, Alejandro

2014, *Marine and Petroleum Geology*, **57**, 187-207

doi: http://dx.doi.org/10.1016/j.marpetgeo.2014.05.013.

Marine and Petroleum Geology 57 (2014) 187–207

Contents lists available at ScienceDirect

Marine and Petroleum Geology

journal homepage: www.elsevier.com/locate/marpetgeo

Research paper

From mechanical modeling to seismic imaging of faults: A synthetic workflow to study the impact of faults on seismic

Charlotte Botter [a, *], Nestor Cardozo [a], Stuart Hardy [b], Isabelle Lecomte [c], Alejandro Escalona [a]

[a] Department of Petroleum Engineering, University of Stavanger, 4036 Stavanger, Norway
[b] Institució Catalana de Recerca i Estudis Avançats (ICREA), Catalonia, Spain
[c] NORSAR, Gunnar Randers vei 15, 2007 Kjeller, Norway

ARTICLE INFO

Article history:
Received 16 December 2013
Received in revised form
19 May 2014
Accepted 25 May 2014
Available online 5 June 2014

Keywords:
Faults
Geomechanical modeling
Finite strain
Seismic properties
Seismic modeling
Seismic interpretation

ABSTRACT

Although typically interpreted as 2D surfaces, faults are 3D narrow zones of highly and heterogeneously strained rocks, with petrophysical properties differing from the host rock. Here we present a synthetic workflow to evaluate the potential of seismic data for imaging fault structure and properties. The workflow consists of discrete element modeling (DEM) of faulting, empirical relations to modify initial acoustic properties based on volumetric strain, and a ray-based algorithm simulating prestack depth migration (PSDM). We illustrate the application of the workflow in 2D to a 100 m displacement normal fault in a kilometer size sandstone-shale sequence at 1.5 km depth. To explore the effect of particle size on fault evolution, we ran two DEM simulations with particle assemblages of similar bulk mechanical behavior but different particle size, one with coarse (1–3 m particle radii) and the other with fine (0.5–1.5 m particle radii) particles. Both simulations produce realistic but different fault geometries and strain fields, with the finer particle size model displaying narrower fault zones and fault linkage at later stages. Seismic images of these models are highly influenced by illumination direction and wave frequency. Specular illumination highlights flat reflectors outside the fault zone, but fault related diffractions are still observable. Footwall directed illumination produces low amplitude images. Hanging wall directed illumination images the shale layers within the main fault segment and the lateral extent of fault related deformation. Resolution and the accuracy of the reflectors are proportional to wave frequency. Wave frequencies of 20 Hz or more are necessary to image the different fault structure of the coarse and fine models. At 30–40 Hz, there is a direct correlation between seismic amplitude variations and the input acoustic properties after faulting. At these high frequencies, seismic amplitude variations predict both the extent of faulting and the changes in rock properties in the fault zone.

1. Introduction

Faults play a key role in restricting or enhancing fluid flow in reservoirs. Although commonly represented as 2D surfaces in reservoir models, faults are actually narrow zones or volumes of highly and heterogeneously strained rocks, with petrophysical properties differing from those of the host rock (Faulkner et al., 2010 and references therein). Faults are complex and their 3D structure and rock properties distribution depend on factors such as host lithology and stratigraphy (Davatzes et al., 2005; Eichhubl et al., 2005; Bastesen and Braathen, 2010), depth of burial at time of faulting (Fisher and Knipe, 1998), initial fault array geometry and structural evolution (Childs et al., 2009), and diagenesis (Solum et al., 2010). Figure 1a illustrates the differences between an actual fault (Fig. 1a, left), and its standard 2D reservoir model representation (Fig. 1a, right). The structures and rocks inside the fault volume affect reservoir connectivity, and can either stop or allow fluid flow depending on their 3D geometry, distribution, and petrophysical properties. 3D fault structure and internal petrophysical properties are therefore primary controls on fluid flow in faulted reservoirs, determining fault-sealing capacity over geologic and production time scales (Faulkner et al., 2010 and references therein). This has major implications in hydrocarbon exploration and production, CO_2 storage, hydrogeological and geothermal systems (e.g., Wibberley et al., 2008).

* Corresponding author.
E-mail addresses: charlotte.botter@gmail.com, charlotte.botter@uis.no (C. Botter).

http://dx.doi.org/10.1016/j.marpetgeo.2014.05.013
0264-8172/

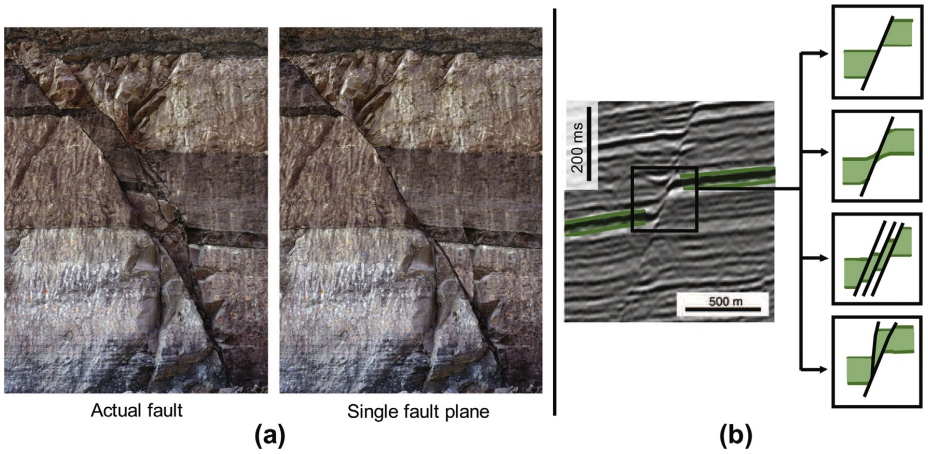

Figure 1. Examples of faults in outcrop (a) and seismic (b). (a) Actual fault (left) and modified picture with a single fault plane (right). This situation can be representative of scales going from m to km (actual and modified pictures from Haakon Fossen, http://folk.uib.no/nglhe). (b) Seismic profile of a fault with four possible interpretations resulting in different assessments of reservoir connectivity (modified from Wibberley et al., 2008).

Despite the impact of faults on reservoir connectivity, we still lack the understanding to fully represent them in reservoir models (Manzocchi et al., 2010). Much of what we know about the structure and internal properties of faults comes from outcrop studies. Field studies of exceptional fault outcrops have given unprecedented detail of the structure and properties of faults in 2D (e.g., Eichhubl et al., 2005) and 3D (e.g., Foxford et al., 1998), as well as an understanding of the physical and chemical processes operating in faults. These studies have also highlighted the complexity of faults in 3D (e.g., Childs et al., 1996, their Fig. 3). Outcrop data, however, mostly consist of small-scale cm to tens of m displacement faults (e.g., Childs et al., 2009, their Fig. 4). For specific combinations of lithology and fault displacement there are a limited number of outcrops and sometimes only incomplete 2D sections. Relationships derived from this small-scale outcrop dataset are often extrapolated to larger scales, although there are some concerns about the validity of this extrapolation (Færseth, 2006). Faults exhibit high variability in 3D, but we still lack quantitative, statistical tools to predict this variability (Manzocchi et al., 2010).

Large-scale faults with hundreds of m to km displacement can be mapped with seismic data. In few exceptional cases there are even well core data across these faults (Aarland and Skjerven, 1998). Fault internal structure and properties, however, are at the limit of seismic resolution. Strictly speaking, fault sealing as a property over the fault volume cannot be mapped directly with seismic. One rather looks at the impact of the fault on the surrounding rock (e.g., across fault pressure differences) to infer something about the fault properties and its sealing capacity (Yielding et al., 2010). A single fault surface with fault sealing properties determined in this manner is a reasonable estimate of the flow properties across and along the fault. However, within the limits of resolution of seismic data, there is room for alternative interpretations, which are equally valid and result in different assessments of reservoir connectivity (Fig. 1b).

Most of the seismic interpretation studies target the recognition of fault networks and their organization, whilst there are not many examples in the literature examining the potential of seismic data to elucidate the complexity of fault structure and its properties in space and time (i.e., fault evolution). A few studies focus on existing 3D seismic data using a range of seismic attributes to resolve the fault seismic response. Townsend et al. (1998) use seismic amplitude anomalies to detect small-scale faulting. Koledoye et al. (2003) decompose a large, seismically resolvable fault into segments to determine shale smearing. Dutzer et al. (2010) estimate fault architecture and fault sealing using seismic attributes in fault volumes. Long and Imber (2010, 2012) map the spatial distribution of fault related deformation using a seismic dip anomaly attribute. Iacopini and Butler (2011) and Iacopini et al. (2012) describe the geometry of complex thrust belts and associated fault damage zones by combining seismic attributes and volume based image processing and visualization techniques. Other works focus on the response of trapped waves within large fault zones in order to relate the anomalous behavior of the seismic wavefield to a possible fault zone (e.g. Ben-Zion et al., 2003; Lewis et al., 2005; Shtivelman et al., 2005). These techniques are however not applicable to standard industry seismic data and faults at large depths. Seismic characterization of fractured reservoirs is well covered in the literature, and fracture recognition (e.g., azimuthal variation in P-field, Li et al., 2003) could to some extent be extrapolated to larger fault zones. Nonetheless, despite all these studies, there is broad skepticism about the use of seismic data to characterize faults, partly because faults are at the limit of vertical and horizontal seismic resolution (Fig. 1b), and partly because standard industry seismic data are not designed to deal properly with the non-specular, back-scattered energy from faults.

The main objective of this paper is to describe a synthetic workflow to assess the potential of seismic for imaging fault structure and properties. The workflow is based on a geomechanical discrete element method (DEM) of faulting (Hardy et al., 2009), simple empirical relations to modify the initial acoustic properties of the model based on fault related finite strain, and a ray-based prestack depth migration (PSDM) simulator (Lecomte, 2008) to produce seismic images of the modeled fault. As a proof of concept, the workflow is investigated here in 2D, although it is possible to extend it to 3D. The DEM models the rock as an assemblage of circular rigid particles in 2D, and its main

purpose is to produce a realistic fault geometry and finite strain field. This strain field is then used to modify initial/base acoustic properties of the host rock using a simple empirical relation between acoustic properties and volumetric strain. The modified acoustic properties are used to construct a reflectivity volume, which is the input to the PSDM simulator. Parameters such as wave frequency and illumination direction and their impact on the resulting seismic image can be evaluated with the PSDM simulator. As a proof of concept, the study will focus mainly on the impact of illumination direction on the resultant seismic image, and on how the amplitude variations are related to the fault architecture and its modified acoustic properties.

Notice that the DEM is not the only way to produce a realistic picture of the fault. A digitized/parameterized schematic of a fault based on outcrop data could also suffice for this purpose. This outcrop based schematic however, will not be exempt from issues related to strain heterogeneity and most importantly upscaling of petrophysical and acoustic properties from the outcrop or laboratory to the realm of industry standard seismic acquisition at a couple of kilometers depth. We use the DEM because besides producing realistic fault architectures, it gives flexibility for imposing different displacement and stress boundary conditions, as well as allowing upscaling in terms of a continuous parameter such as strain. Practical considerations (i.e. computing limitation in the number of particles) in the DEM do not allow us to simulate faulting at the grain scale, but rather in a large fault displacement model, bulk strain at a meter size scale. Our geomechanical model does not predict the effect of fault related, grain scale processes such as disaggregation or cataclasis on rock properties. Rather we use a simple relation between bulk volumetric strain and change of acoustic properties to update the model. The ultimate proof of this approach is the production of a reflectivity volume realistic enough that contains the effects of faulting.

We illustrate the application of the workflow in 2D to a large-scale (100 m displacement) normal fault model in an interlayered sandstone-shale sequence. To evaluate the impact of particle (i.e. element) size in the DEM, we run the simulation with two assemblages of similar bulk stress–strain behavior but different particle size: one with coarser particles and another with finer particles approximately half the size of the coarser one. The finer particle size assemblage results in more strain localization and a narrower fault area. This result, which at first view seems to point up a weakness of the DEM method, actually indicates the richness and complexity of the simulated fault behavior. Just as in analogue models, for modeling materials of similar bulk behavior, fault zone thickness is controlled by particle size (Eisenstadt and Sims, 2005), so in the DEM strain localization and fault extent are controlled by particle size. We construct reflectivity grids for the two, coarse and fine particle size models, using our simple relation between change of acoustic properties and volumetric strain in the models. PSDM simulations of the two models for different wave frequencies and illumination directions, resulting in different seismic images, are presented. In an attempt to understand which combination of these parameters result in a better prediction of the structure and properties of the fault, we look in the different seismic images at the variation of seismic amplitude along interpreted reflectors, and compare it to the variation in acoustic properties along the same paths in the input reflectivity models. Overall, this exercise provides guidelines for a better characterization of faults using seismic data.

2. Methodology

Our workflow takes into consideration the complexity of fault development, the large finite strains resulting from faulting and the impact of the overburden. The methodology is divided in three steps: 1. Geomechanical simulation using the discrete element method (DEM), 2. Empirical relations applied to the geomechanical model to modify its initial acoustic properties based on finite strain, and 3. Simulated seismic imaging (PSDM), taking into account effects in resolution and illumination. This methodology is similar to that of Couples et al. (2007), where they use a continuum finite element technique to simulate faulting, and ray-tracing (1D convolution) of the geomechanical model (with acoustic properties modified by finite strain), to produce a seismic image of the fault. Our workflow, however, has some important differences. For geomechanical modeling, we use a discontinuum, meshless technique (DEM; Hardy et al., 2009), and for seismic imaging, we use a ray-based algorithm (Lecomte, 2008) that, as opposed to 1D convolution, can handle model and survey-based effects in resolution and illumination, as well as diffracted energy (Gjøystdal et al., 2007; Lecomte, 2008; Drottning et al., 2009; Kaschwich et al., 2011).

2.1. Mechanical modeling

The DEM is a discontinuum method used to simulate the dynamic evolution of a system of discrete elements under applied forces and displacement boundary conditions. Discrete element models, in common with other numerical techniques, have both advantages and disadvantages when considering their application to geological problems (Gray et al., 2014). On one hand, modeling of high-strain deformation of brittle sedimentary cover is ideal for the discrete element technique as it is well suited to studying problems in which discontinuities (shear-zones, faults, fractures, etc.) are important. The DEM allows large deformations involving large relative displacements of individual particles and complex, abrupt boundary conditions without the need for re-meshing (Cundall and Strack, 1979; Finch et al., 2004: Egholm et al., 2007; Hardy, 2008, 2011; Thompson et al., 2010). In addition, it allows localization and the formation and linkage of faults and fractures as a natural part of the numerical scheme. However, one disadvantage of the technique lies in the necessary, but tedious and time-consuming, calibration of particle parameters to the emergent rock physical properties (Egholm et al., 2007; Holohan et al., 2011). The selection of particle parameters ultimately controls the bulk mechanical behavior of the assembly under consideration, and has to be calibrated rather than directly input as in the case of finite element or finite difference methods. The particle properties and the emergent bulk material properties are typically assessed through the use of angle of repose and biaxial tests. Such tests are performed on a subpart of the system in order to evaluate multiple sets of particle property values within acceptable runtimes (Oger et al., 1998; Finch et al., 2004; Holohan et al., 2011). Similarly, the sensitivity of models to subtle initial differences in, e.g., assembly packing is well known (Abe et al., 2011). Even with meticulous and precise work, the calibration process can lead to results slightly different from similar finite element models (Gray et al., 2014; Zhang et al., 2013). Indeed, the interaction of thousands of particles, both locally and globally, leads to situations wherein our ability to explain precisely why a particular fault or fracture grew at the expense of another is limited. Such issues also exist in analogue modeling of faulting where repeated experiments under the same boundary conditions are reasonably reproducible but not in the finer details of the fault and fracture systems (e.g. van Gent et al., 2010). The important message to be taken from any of these studies is not the precise location of an individual fault, but rather the distinctive, repeatable patterns and sequences of structural behavior emerging from multiple experiments. Bearing these factors in mind, we consider that the DEM is an appropriate method to study the process of fault formation: from initiation, through propagation and linkage,

including fault-related folding. Computational limitations on element size and/or model resolution are important, but recent, rapid advances in computational power and the parallelization of discrete element codes allow for higher resolution models.

Fault evolution has been studied by DEM modeling at large and small scales, and both at shallow and deep depths (Schöpfer et al., 2007; Egholm et al., 2008; Hardy, 2011; Terheege et al., 2013). Here we apply the technique to large-scale faults (100 m to km fault displacement) in sedimentary-layered sequences at a few kilometers depth. The particular discrete element code employed here is a variant of the lattice solid model of Mora and Place (1993), further developed by Hardy and Finch (2005, 2006) and Hardy et al. (2009), where the rock mass is treated as an assemblage of circular particles in 2D (Fig. 2a–b). These particles are rigid, have meter-size scale (in km size simulations) and a given density. They interact with elastic, frictional, and gravitational forces (Fig. 2a–c). Imposed displacement conditions are applied to the boundary particles in order to initiate and propagate faulting in the model (Fig. 2a, bold black lines and arrows). As the assembly, these boundary particles are unbounded and frictional, and displace according to the assigned direction parallel to the fault plane. At each time step, the total forces applied to a particle by its neighbors are used to compute its displacement. The particles are moved to their new positions by integrating their equations of motion using Newtonian physics and a velocity Verlet numerical scheme (Mora and Place, 1993). Figure 2b shows a 2D particle assemblage before (left) and after deformation (right).

To model a layered sedimentary sequence at a few kilometers depth requires some refinement of our modeling technique. Firstly, the simulation of a layered sequence comprising weak and strong materials (shale and sandstone, Fig. 2a) requires the use, and calibration, of different coefficients of interparticle friction (Fig. 2c) for each rock material. Secondly, to bring the model to reservoir depths, we must apply an overburden stress at the top of it. This is a traction component applied at the center of the particles, normal to the slope of the top surface. For each particle, the slope defined by its left and right neighbors is calculated, and the overburden traction is applied perpendicular to it (Fig. 2d). The same methodology is used in biaxial simulations for the calibration of the sandstone and shale rock materials (Section 3). In our model, there is no bonding between particles, which results in the assemblage having no tensile strength and a purely frictional behavior (Hardy, 2013).

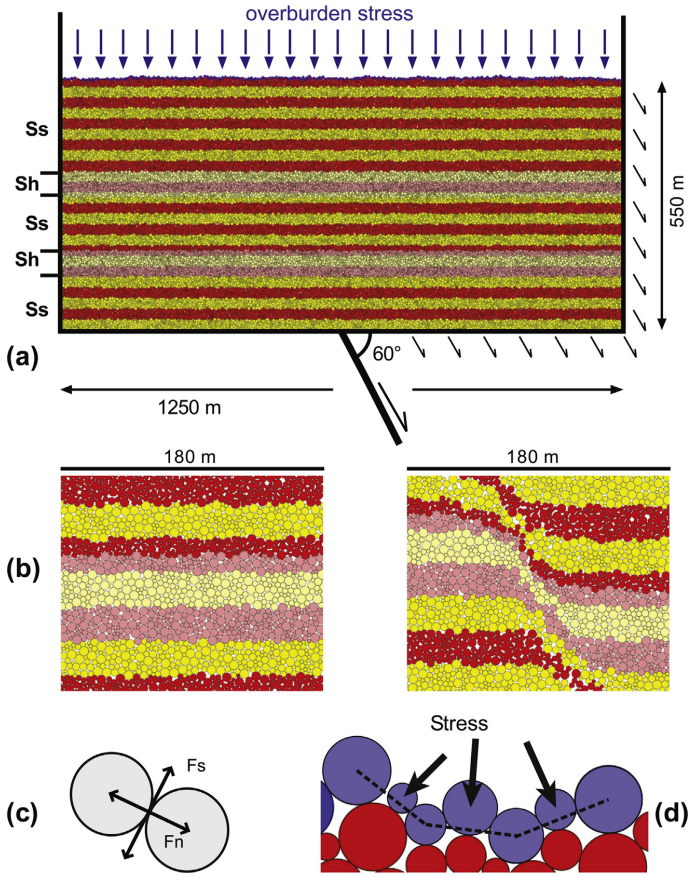

Figure 2. Example of the DEM used in the workflow: (a) Initial fault model with four different particle radii, sedimentary layering (Ss = sandstone and Sh = shale), and boundary conditions for a 60° dipping normal fault represented by the small black arrows on the hanging wall side of the model. (b) Zoom in before (left) and after (right) faulting. (c) Normal (Fn) and shear (Fs) forces at particle contacts. (d) Overburden stress applied normal to the top surface at the center of each particle.

For simulations at several kilometers depth in an upper crust full of discontinuities and in frictional equilibrium, a purely frictional failure envelope is a good representation of rock behavior (Hubbert, 1951; Zoback, 2010). In this case, the particle elasticity/stiffness chosen allows some overlap between the particles in contact (<1% of the particles combined radii), and thus frictional interaction without unrealistic overlaps.

Although the DEM is a mechanical model, it has some interesting similarities with analogue, scaled models. As in analogue models, the modeling materials should be chosen to reproduce the appropriate bulk rock behavior at the scale of consideration, so in the DEM the right particle properties should be chosen to give a realistic bulk rock behavior at the scale of the problem. In addition, just as in analogue models the grains of the modeling material are not the same as the grains of the rocks being modeled, so in the DEM the particles in the model do not represent the sedimentary rock grains. At the scale of our problem (a large fault), the DEM captures the bulk behavior and geometry of faulting and its associated deformation, but not the physical and chemical processes occurring at the grain scale. Even though the DEM does not target grain scale or rock-fluid interaction processes, it results in realistic fault development and evolution that we can use as input to our workflow. Many studies have shown the ability of the technique to reproduce realistic fault geometries in extensional and contractional settings, at seismic to sub-seismic scales and at reservoir depths (e.g. Egholm et al., 2008; Hardy et al., 2009; Hardy, 2011).

2.2. Change of seismic properties due to finite strain

Large displacement faults involve large and permanent deformations (folding and fracturing). Under this situation, we cannot easily relate stress to strain. Neither can we use standard, continuum rock physics equations to predict the change of elastic properties due to large finite strains. Few studies discuss the impact of large strains on rock properties. Holt et al. (2008) study the impact of small volumetric strains (lower than 1%) on seismic velocities in cm-scale sandstone and shale samples, Sigernes (2004) measured seismic velocities in cm-scale samples at several distances from the fault core in five normal fault outcrops in siliciclastic rocks. Skurveit et al. (2013) investigate deformation mechanisms and their impact on ultrasonic velocity during shear-enhanced compaction in poorly lithified sandstone. Hatchell and Bourne (2005) look at the impact of pressure depletion induced strain and fracturing on seismic velocities in a reservoir at a field scale. Although these studies encompass a large range of lithologies, scales and finite strain magnitudes, they broadly illustrate how volumetric strain and fracturing modify seismic velocities: compaction (i.e., negative volumetric strain) decreases porosity, thereby increasing density and seismic velocities, while dilation (i.e., positive volumetric strain) and shear or tensile induced fracturing have the opposite effect. Scaling of the lab results and outcrop studies to the larger dimensions and much lower wave frequencies of industry standard seismic is complicated, such that we do not know exactly how finite strain modifies acoustic properties at the reservoir scale.

We use the general consensus of the studies above. As a first hypothesis, we consider only the volumetric strain effects on seismic properties. Shear strain effects are of course important, particularly for fracture-induced porosity in low-porosity sedimentary rocks. Porosity, density, and seismic velocities are assigned to the rock materials in the DEM model before faulting (Fig. 2a). These values are averages from the literature adapted to the scale, depth and stress conditions of the simulations. In the models of Section 3, they correspond to sandstone (Hoek and Brown, 1997; Mavko et al., 2009) and shale (Horsrud et al., 1998; Nygård et al., 2006). At any stage of the DEM simulation, incremental and total particle displacements are known. These are used to compute incremental or total strains (the gradients of the particles incremental or total displacements). We use a nearest-neighbor routine (Cardozo and Allmendinger, 2009) to compute strain. Essentially, we divide the DEM model into regular cells. At the center of each of these cells, the strain is computed from the displacements of the particles within a maximum radius from the cell center. We use a cell size appropriate for capturing the complexity of fault related strain, and a maximum radius large enough to include six particles in the strain computation (in 2D, a minimum of 3 particles are needed to compute strain; Allmendinger et al., 2012). Underlying the strain computation is the assumption that finite strain is homogeneous in the cells, thus we are converting (and in a way upscaling) the heterogeneous strain in the fault volume, to a cell-based strain. Although not a direct measure of the physical processes occurring in the rocks at the grain scale, the computed strain is a proxy for these processes (just as in a triaxial test, the axial strain of a sample is a proxy for the processes occurring in the sample at the grain scale). We use the computed finite strain and specifically dilatation (the product of the principal stretches minus one) to modify the initial rock properties. Data from Sigernes (2004) on siliciclastic and from Jeanne et al. (2012) on carbonate fault zones reveal highly variable density and P-wave velocity changes (e.g., from 10% to 50% and more) across and away from the faults. We assume here that the maximum changes of porosity, P-wave and S-wave velocities at our model scale are within a reasonable range of ±25% from their initial values due to dilation or compaction. The fact that 100% compaction is unrealistic is also taken into account (Fig. 3).

We modify the porosity from its initial value according to a linear relation (Fig. 3):

$$\phi = \phi_{ini}(0.25\varepsilon_v + 1), \quad -1 \le \varepsilon_v \le 1 \tag{1}$$

where ϕ is porosity, ϕ_{ini} is initial porosity and ε_v is volumetric strain. Rock density ρ is computed from porosity assuming saturated conditions:

$$\rho = \rho_g(1-\phi) + \rho_w\phi \tag{2}$$

where ρ_g and ρ_w are grain and fluid densities respectively. P-wave velocity V_P follows a sigmoidal relation (Equation (3) and Fig. 3):

$$V_P = \begin{cases} V_{P_{ini}}\left(-0.25\varepsilon_v^2 - 0.5\varepsilon_v + 1\right), & -1 \le \varepsilon_v < 0 \quad \text{(compaction)} \\ V_{P_{ini}}\left(0.25\varepsilon_v^2 - 0.5\varepsilon_v + 1\right), & 0 \le \varepsilon_v \le 1 \quad \text{(dilation)} \end{cases} \tag{3}$$

where $V_{P_{ini}}$ is the initial P-wave velocity. This sigmoidal relation emphasizes that the change of V_P is more significant at lower strains than at relatively large strains. For sandstone and shale, the relation between V_P and S-wave velocity V_S is within the range defined by Han's and Castagna's empirical laws (Sigernes, 2004). We use the Han's relation to compute V_S:

$$V_S = 0.794V_P - 0.787 \tag{4}$$

Equations 1–4 allow us to compute the change of seismic properties due to finite volumetric strains. Even if the estimated values are not accurate, they are within a reasonable range (for poorly lithified sediments, the changes of acoustic properties due to large volumetric strains can be more dramatic; Skurveit et al., 2013 and Fig. 3). Relative changes of seismic properties within the fault zone rather than their absolute values are more important for seismic imaging.

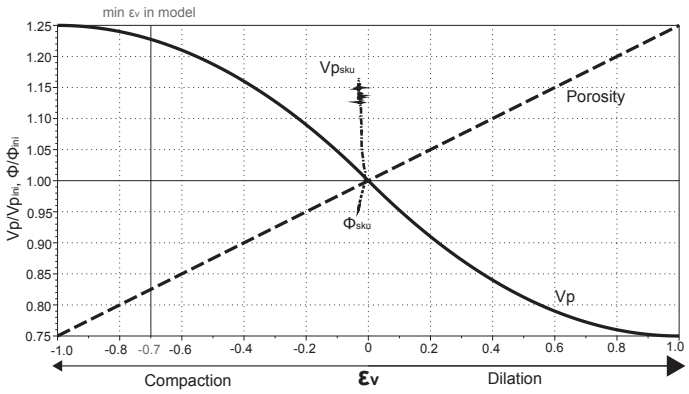

Figure 3. Assumed change of porosity ϕ and P-wave velocity V_P with volumetric strain ε_v. ϕ_{ini} and $V_{P_{ini}}$ are porosity and P-wave velocity before faulting. ϕ_{sku} and $V_{P_{sku}}$ are porosity and P-wave velocity from triaxial testing of poorly lithified sandstone at 15 MPa (Skurveit et al., 2013).

2.3. Simulated seismic imaging

Seismic imaging simulation is used to assess the impact of fault internal structure and properties on the resulting seismic image. With the known architecture and estimated rock properties of the fault from geomechanical modeling, it is possible to experiment with various parameters (especially those related to survey design, but also processing) to see their impact on the seismic images. The technique we use is a 3D PSDM simulator (Lecomte, 2008). This simulator acts as an image-processing method by distorting the input reflectivity to reproduce the effects of seismic imaging in PSDM mode.

The standard trace-modeling method of the industry is 1D convolution in the time domain, i.e., convolution of a vertical reflectivity log in time with a wavelet. 1D convolution can only simulate poststack time-migrated sections for limited and non-totally realistic modeling cases, i.e., for full-aperture surveys and models without lateral variations (1D). Applying 1D convolution to 2D/3D models can be misleading, with possible mis-positioning of seismic events and total lack of lateral resolution effects. To the contrary, the PSDM simulator (Lecomte, 2008) works in the pre-stack domain and in depth, and properly handles 3D effects in resolution and illumination as function of various parameters such as velocity model, survey geometry, wavelet, etc. (Lecomte and Kaschwich, 2008). Besides vertical resolution, which is more or less predicted by 1D convolution, the PSDM simulator reproduces also lateral resolution effects such as those resulting from faults or other structural discontinuities. Another important feature of this seismic modeling approach is the automatic integration of 3D illumination effects, i.e., the ability of the simulator to properly reproduce whether or not a given structure will be seen by seismic. Though largely going beyond the limitations of 1D convolution, the PSDM simulator is still approximate in comparison to direct modeling methods solving the full-wave equation (e.g., via finite differences – FD), because it does not take into account the complete wavefield and considers only single scattering. The processing time of the PSDM simulator is however quite similar to 1D convolution, because PSDM cubes are generated directly from input reflectivity cubes, i.e., without calculating synthetic recordings and processing them, as it would be done in a standard FD-based modeling followed by PSDM. The latter approach is far more complex and time-consuming, requiring several codes and expert users. The PSDM simulator is therefore still a fast and robust approach, more advanced than 1D convolution, and allowing efficient and near-interactive sensitivity analyses on various seismic parameters (Drottning et al., 2009).

The structural input to the PSDM simulator is an angle-dependent reflectivity cube, which is obtained from the acoustic properties of the model, i.e., density, V_P, and V_S (Fig. 4a). This reflectivity cube can be converted to the wavenumber domain using a Fast Fourier Transform (FFT, Fig. 4a), and further processed using ray-based modeling to build the so-called PSDM filters. For these, and key to the method, illumination vectors (Lecomte, 2008) are calculated at a given reference point (e.g., center of the target) using ray-based methods (Gjøystdal et al., 2007). The illumination vectors are computed according to a selected survey, wave type, velocity model and other PSDM related parameters. They are formed at the considered point as a combination of the incident ray and the scattered one. In case of specular reflection (i.e., following Snell's law), the illumination vectors direction indicate which reflector dips will be seen by the seismic waves, i.e., the reflectors normal to the illuminations vectors. But the illumination vectors are also indicative of other scattering patterns and therefore cover diffraction effects too, as demonstrated by Kaschwich et al. (2011). From the illumination vectors and a given wavelet, a PSDM filter is generated in the wavenumber domain (Fig. 4b–c, center). Figure 4b (center) is the PSDM filter corresponding to a complete survey acquisition with illumination of a wide range of dips, including the horizontal ones (the latter corresponds to the vertical band in the PSDM filter). Figure 4c (center) is the PSDM filter using a sub-selection of the survey to generate an off-side illumination, chosen to avoid illuminating the flat reflectors (the vertical band in the PSDM filter is not covered). Figure 4d (center) is an ideal (synthetic) case where all reflector dips would be illuminated; no survey can really produce such cases in practice. This latter case is somewhere similar to 1D convolution.

Finally, the PSDM filter is applied to the input reflectivity in the wavenumber domain, and an FFT^{-1} over this result is used to produce the simulated PSDM cube in the spatial domain (Fig. 4b–c, right). Note that the application of an inverse FFT (FFT^{-1}) to the PSDM filter itself yields the corresponding Point-Spread Function (PSF) in the spatial domain, that is the image response of a point scatterer at the reference point (Fig. 4b–c, left; Lecomte, 2008). Such PSF is indicative of the local imaging capability of the PSDM, i.e., how well retrieved a point scatterer will be, which is especially important for features such as faults, fractures, and other structural

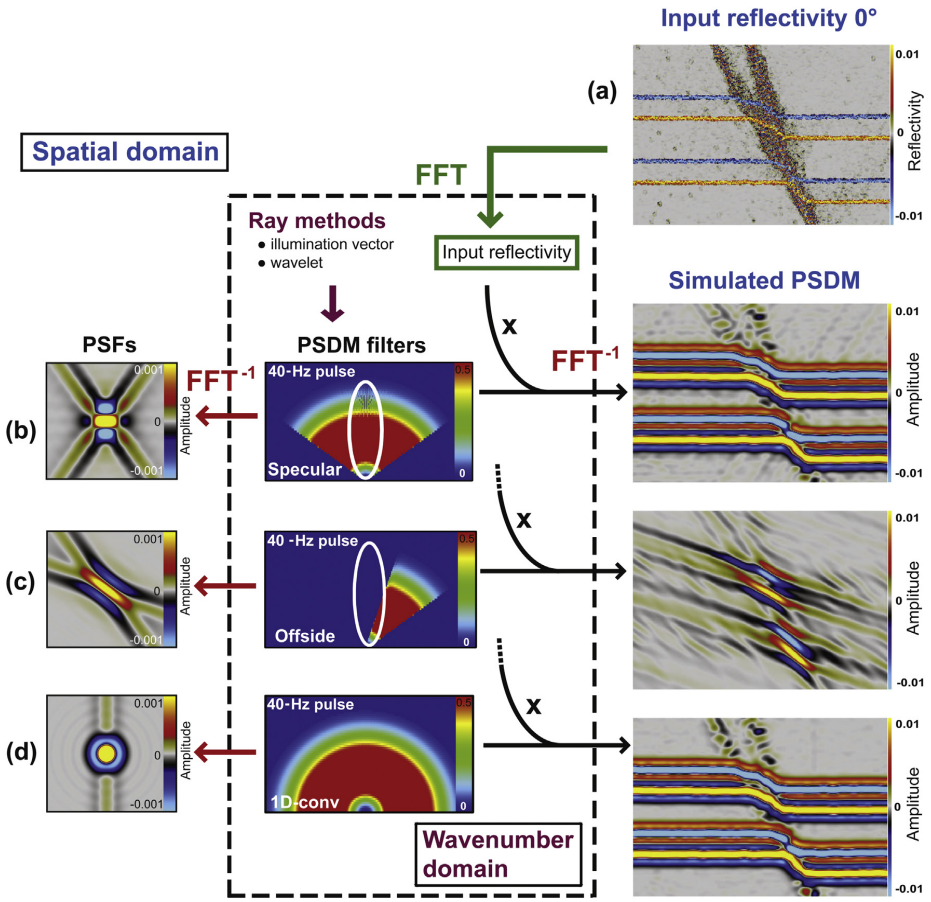

Figure 4. Illustration of the PSDM simulator. (a) A reflectivity grid is input in the spatial domain. This input reflectivity is converted to the wavenumber domain using a Fast Fourier Transform (FFT). Ray methods are used to calculate PSDM filters (center) in the wavenumber domain for two types of illumination: (b) Specular and (c) Offside. The corresponding filters in the spatial domain (point spread functions or PSFs, left) are shown. Application of the PSDM filters to the input reflectivity in the wavenumber domain, plus an inverse FFT (FFT^{-1}) on the result of this operation produces the simulated PSDM images (right). (d) Perfect illumination (approximate 1D-convolution). In b to d, a 2D constant-offset survey, a homogeneous overburden, and a 40-Hz, zero-phase Ricker wavelet were used.

discontinuities. Applying the PSDM filter to the input reflectivity in the wavenumber domain is equivalent to a 3D convolution of the PSF with the reflectivity cube in the spatial domain. The process in the wavenumber domain is however more efficient when using only one PSF for the whole target model, as done here, as we only consider one reference point (center of the images). Spatially variable PSFs can also be applied for a more accurate imaging, depending on the size of the target zone (here fault zones), although this is more time-consuming. Preliminary results of spatially-variable PSF modeling can be found in Zühlsdorff et al. (2013), and are more relevant when dealing with 3D models.

The resulting simulated PSDM cubes are more realistic than the image produced by 1D convolution considering the limitations of the latter, especially its lack of model-based wave-propagation effects for a given survey. 1D convolution can only be realistic for geological structure of low complexity (weak lateral velocity variation). As an approximation to 1D convolution, the PSDM simulator was used with a perfect PSDM filter, i.e., with illumination of all reflector dips, but still with a certain width due to the frequency band of the wavelet (Fig. 4d, center). This corresponds in the spatial domain to a more point-wise PSF whose size only depends on the wavelength frequency band and the velocity at the reference point (Fig. 4d, left). A true 1D-convolution operator would even be narrower laterally, i.e., corresponding to a 1D (vertical) PSF. Though the obtained image (Fig. 4d, right) resembles the other PSDM-simulated ones (Fig. 4b, c, right), except for less migration noise in Figure 4d, there is no way to experiment with other parameters than the frequency band (vertical resolution), and certainly no possibility to consider realistic geologic models and surveys with correct lateral resolution and illumination effects.

3. Application: large normal fault

We show the application of the workflow in 2D to a 60° dipping normal fault in a 1.25 × 0.55 km interbedded sandstone-shale sequence (Fig. 2a). The fault is imposed as a displacement

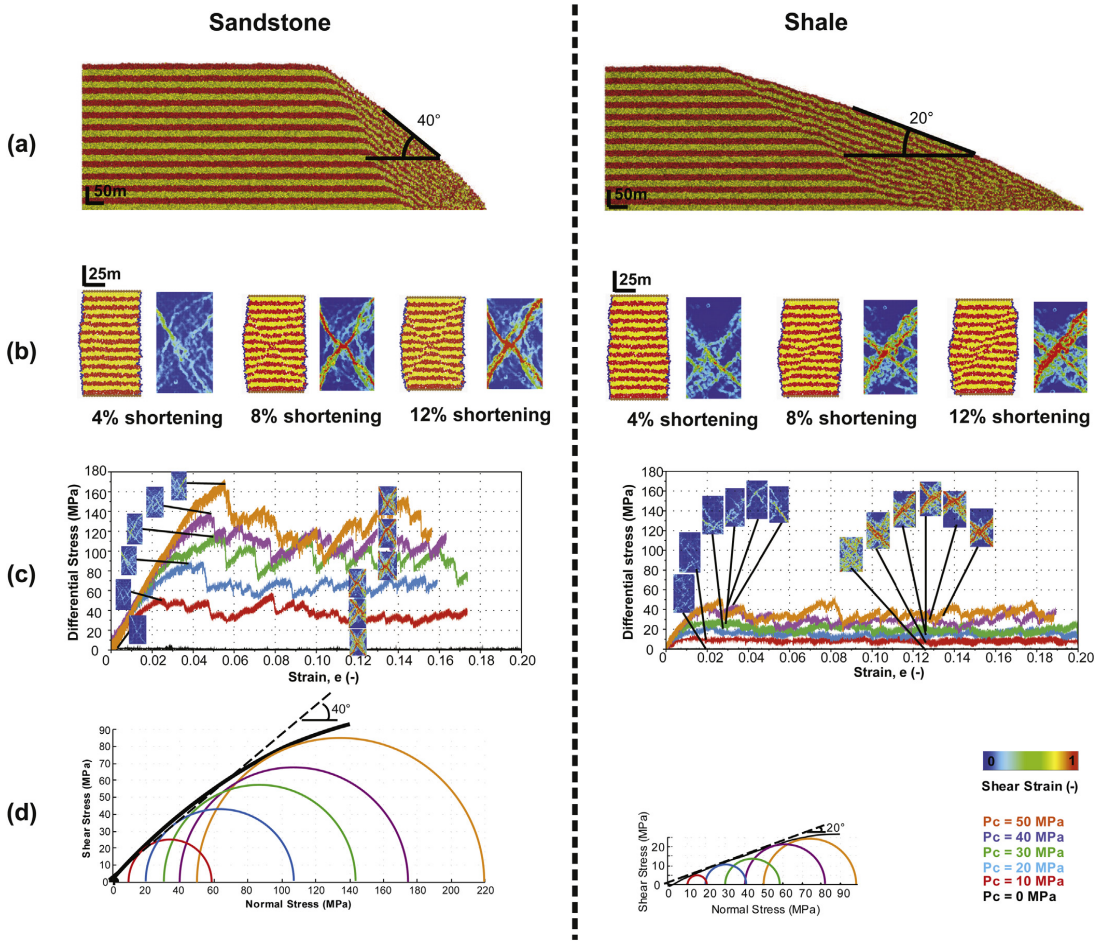

Figure 5. Bulk response of the coarse sandstone and shale assemblages for the input particle properties of Table 1. (a) Collapse simulations. (b) Biaxial compressive simulations under 20 MPa confining pressure at three shortening stages (left is geometry and right is shear strain). (c) Axial strain vs. differential stress curves. Rectangular images are samples colored by shear strain at different values of axial strain. (d) Failure envelopes from biaxial simulations.

boundary condition at the base of the model (Fig. 2a). The shale layers are 50 m thick and are thinner and more incompetent than the sandstone layers (Fig. 2a). The competence contrast between the shale and the sandstone layers has significant impact in both the DEM and the simulated seismic images. A normal stress of 25 MPa is applied at the top of the model, representing a sedimentary overburden of about 1.5 km (Fig. 2a). To investigate the impact of particle size on fault evolution, two DEM assemblages of similar bulk stress–strain behavior are considered. The first assemblage is constituted of 45,000 particles with four different radii going from 1.25 to 3.125 m. We refer to this assemblage as the "coarse model". The second assemblage has 180,000 particles with four different radii going from 0.625 to 1.5625 m. We refer to this assemblage as the "fine model". These two, 2D models are used to illustrate the impact of faulting on seismic properties, and to run sensitivity analyses of the effect of illumination direction and frequency on the resulting seismic images.

3.1. Mechanical modeling

3.1.1. Coarse model

3.1.1.1. Material calibration. As discussed in Section 2.1, the first step in the DEM simulation is to calibrate the assemblage so that it mechanically behaves like a real rock, in our case sandstone and shale, at the scale and depth of consideration. To do this, we use two tests: 1. Collapse simulations at km scale where initially the assemblage is inside a rigid box, and then one side of the box is removed, allowing the measure of the static angle of repose of the material (Fig. 5a); and 2. Biaxial compression simulations at different confining pressures, which allow determining the failure envelope of the material (Fig. 5b and c). The dimensions of the biaxial samples are 125 × 250 m (Fig. 5b), which is a representative size of the DEM simulation (Fig. 2a–b), but does not target laboratory (cm) to grain (mm) scales.

For the four particle radii going from 1.25 to 3.125 m and for the particle properties of Table 1 (particles density, stiffness and

Table 1
Particle properties of the coarse and fine assemblages for sandstone and shale materials.

Input parameters:		4 particle radii (m)	Density of particles (kg/m^3)	Particle stiffness (GPa)	Particle friction
Sandstone	Coarse	1.25–3.125	2500	5.6	0.35
	Fine	0.625–1.5625			
Shale	Coarse	1.25–3.125	2500	5.6	0.1
	Fine	0.625–1.5625			

interparticle friction), the bulk response of the assemblages representing sandstone and shale is summarized in Figure 5 and Table 2. The interparticle friction is the main parameter controlling the competence of the material. The interparticle friction in the shale is about one third that in the sandstone (Table 1), such that the bulk internal friction angle (φ_i) of the shale is about half that of the sandstone in both, the collapse simulations (Fig. 5a) and the biaxial tests (Fig. 5b–c, Table 2). Sandstone and shale are known to have a large range of values of mechanical properties. For reservoir conditions at the depth of our study, an internal angle of friction of 40° (Fig. 5a) is adequate for consolidated sandstone (Zoback, 2010). A bulk internal friction angle of about 20° (Fig. 5b) is consistent with North Sea shale at 1–2 km depth (Horsrud et al., 1998). Notice that even though the mechanical behavior of the sandstone and shale assemblages is purely frictional (zero strength at zero confining pressure and no tensile strength), there is strain localization (i.e., faulting) in both the sandstone and shale, as indicated by the shear strain of the samples at different amounts of shortening (Fig. 5b–c). The sandstone presents two conjugate faults, each one making an angle of about 25° ($45° - \varphi_i/2$) with the direction of the axial stress (σ_1). The shale shows two conjugate faults, less localized than in the sandstone, and making an angle of about 35° with σ_1. In the sandstone and shale, the expected normal fault dip angles ($45° + \varphi_i/2$) are 65 and 55°, respectively. The fault displacement boundary condition at the base of the DEM model, corresponding to a 60° dipping normal fault (Fig. 2a), is consistent with the mechanical behavior of the sandstone and shale materials.

3.1.1.2. Evolution of geometry and finite strain. To model the 60° dipping fault, we use the DEM model presented in Figure 2a, with extension of the model controlled by the displacement of the assemblage boundary particles of the hanging wall parallel to the dip direction. The model was run to 100 m fault displacement with a total horizontal extension of 50 m. Figure 6 presents the evolution of the model geometry (left), shear strain (center), and volumetric strain (right) at four stages of vertical fault displacement: 10, 40, 60 and 100 m (Fig. 6a–d). At 10 m fault displacement (Fig. 6a), a fault starts to propagate across the assemblage. The fault dips steeply, about 65°–70° in the sandstones, and at a lower angle of about 60° in the shale. A second less steep fault nucleates from the initial fault in the center sandstone layer around 40 m fault displacement (Fig. 6b). The dip angle of this second fault in the sandstone and shale layers is 60° and 50°, respectively. These two faults continue to develop until later stages (Fig. 6b–d). From 80 m fault displacement, the second, less steep fault becomes more active displaying larger displacements and shear strains (Fig. 6d). From 60 m fault displacement, there are visible offsets of the sandstone layers, especially the top layer, while the shale layers are smeared across the fault zone (Fig. 6c–d, left). Shear strain (Fig. 6, center) shows that the evolution of the normal fault zone is complex with low and narrow strain areas at early development (Fig. 6a–b), to high and broader (e.g., up to 50 m) strain areas at large displacements (Fig. 6c–d). High shear strain zones link to form larger faults. At 10 m fault displacement (Fig. 6a), the fault segments have already linked to form the main fault. The second fault starts to develop at about 20 m fault displacement and links to the first one at about 40 m fault displacement (Fig. 6b). Volumetric strain increases with fault displacement, mainly with a dilation component (positive volumetric strain, red in the web version, Fig. 6 right), although at certain locations the fault is under compaction (negative volumetric strain, blue, Fig. 6 right). The highest shear strain regions correlate with the highest dilation and compaction. The shale layers experience higher compaction and thinning within the fault zone, especially the lowest shale layer (Fig. 6, right). At 100 m fault displacement, the more incompetent shale layers show continuous smearing across the two faults, whereas the sandstone, including the center layer, display clear, different offsets across the two faults (Fig. 6d, right).

3.1.1.3. Change of seismic properties. Seismic imaging simulation needs an input reflectivity model of the fault at a given amount of displacement. Seismic resolution of the fault will be dependent on the amount of fault displacement. To have a sufficient impact on the displacement of the reflectors and on the resultant seismic image, we choose to use the normal fault DEM model at 60 m of fault displacement (Fig. 6c). At this amount of fault displacement, the shale layers are not completely offset, but the fault structure is sufficiently complex to investigate on seismic. To compute the seismic properties in the fault, we assign elastic properties to the sandstone and shale before faulting (Table 3). These properties are average values from the literature for intact sandstone (Hoek and Brown, 1997; Mavko et al., 2009) and shale (Horsrud et al., 1998; Nygård et al., 2006) at ~1.5 km depth and at the scale of the DEM. The computed finite volumetric strain (section 2.2) at 60 m of fault displacement (Fig. 6c right) is then used to modify the initial rock properties (Table 3) using Equations 1–4. Figure 7 shows the change of density (Fig. 7a) and seismic velocities (Fig. 7b) at 60 m of fault displacement. As expected from the mechanical properties of the sandstone and shale (Fig. 5), the shale layers within the fault zone experience more volumetric strain and larger relative changes in wave velocities and density than the sandstone layers.

3.1.2. Fine model

To investigate the impact of particle size on the DEM simulation and its resultant seismic images, we use a normal fault model as in Figure 2a, but with half-sized and four-times more particles than in the coarse model of the previous section.

3.1.2.1. Material calibration. With the exception of particle radii, particle properties in the fine sandstone and shale assemblages are the same as in the coarse assemblages (Table 1). However, smaller particles in the fine assemblage require a smaller time step of computation, resulting in significant longer runtimes. Due to this time and computing limitations, only biaxial compression simulations at different confining pressures were run for the calibration of the fine sandstone and shale assemblages (Fig. 8). As in the biaxial

Table 2
Calibration results for the coarse and fine, sandstone and shale assemblages. The angles of repose and internal friction are equivalent.

Calibration results:		Angle of repose	Angle of internal friction	Coefficient of internal friction	Fault dip in extension
Sandstone	Coarse	40°	40°	0.84	65°
	Fine	\			
Shale	Coarse	20°	20°	0.36	55°
	Fine	\	19°	0.34	54.5°

\ This back slash means that there is no value available for this box.

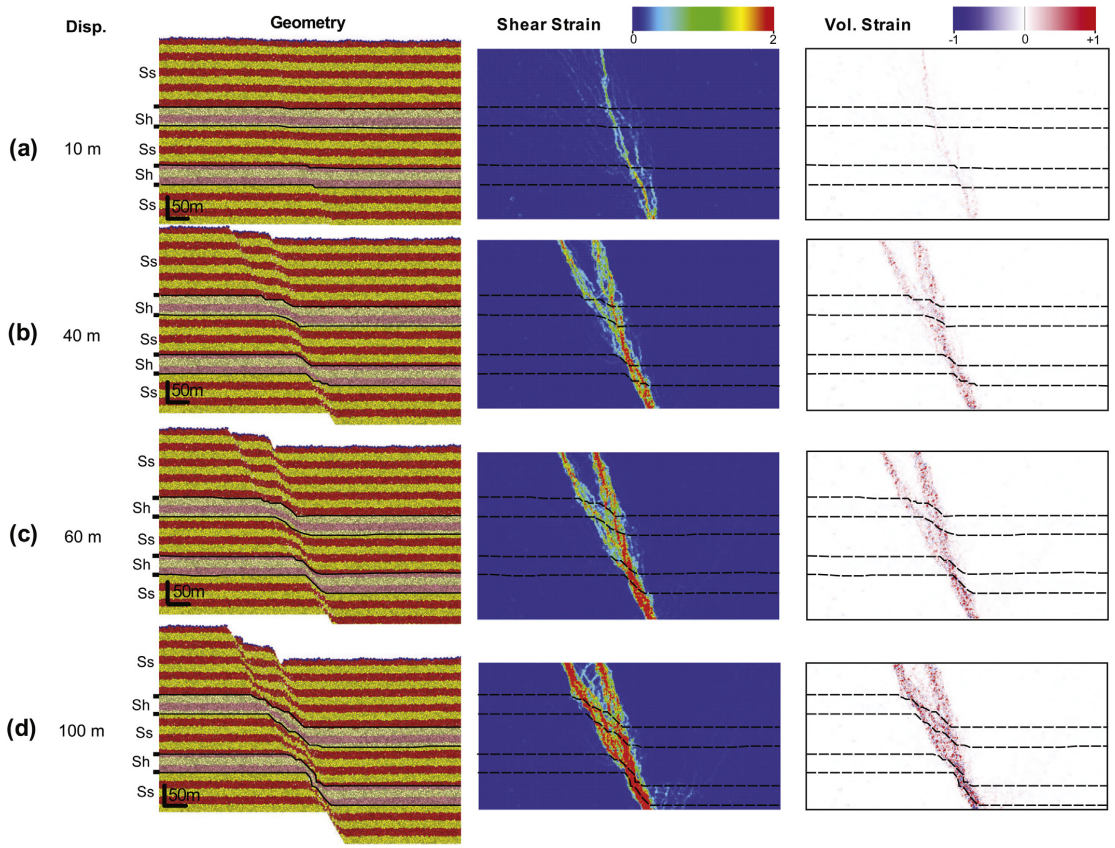

Figure 6. Evolution of the coarse DEM normal fault simulation at: (a) 10, (b) 40, (c) 60 and (d) 100 m of fault displacement. Left is geometry, center is shear strain, and right is volumetric strain. Ss and Sh represent sandstone and shale layers respectively. Black lines are layer boundaries.

tests for the coarse assemblages, the dimensions of the samples for biaxial compression of the fine assemblages are 125 × 250 m (Fig. 8a). For the four particle radii going from 0.625 to 1.5625 m and for the particle properties of Table 1, the bulk stress–strain response of the fine sandstone and shale assemblages is close to that of the coarse ones (Figs. 8 and 5 and Table 3). Biaxial simulations of the fine sandstone and shale assemblages under a confining pressure of 20 MPa (Fig. 8a), show an evolution of faulting similar to the one observed in the biaxial tests of the coarse sandstone and shale assemblages at the same confining pressure (Fig. 5b). Faulting in the fine and coarse sandstone and shale assemblages is also similar at other confining pressures between 0 and 50 MPa (Figs. 8b and 5c). However, in the fine sandstone and shale assemblages, there is more strain localization and the fault zones are narrower and better defined (Fig. 8a). Stress–strain curves and failure envelopes of the fine and coarse sandstone and shale assemblages are similar, although the stress–strain curves of the coarse assemblages display more variability (Figs. 8b and 5c). For similar particle properties and bulk stress–strain behavior, particle size influences strain localization, extent of faulting and its resolution. Although the fine and coarse sandstone and shale assemblages have similar bulk mechanical behavior, they are essentially different. The fine sandstone and shale assemblages result in narrow fault zones, while the coarse assemblages give more distributed fault related deformation. This numerical issue can to some extent reflect what is observed in nature, where faulting in rocks of similar bulk mechanical behavior may be expressed as either narrower or broader zones of fault related deformation.

Table 3
Acoustic properties assumed for the unfaulted sandstone and shale materials.

	Φ_{ini}	ρ_g (kg/m^3)	$\rho_{tot\ ini}$ (kg/m^3)	$V_{P\ ini}$ (km/s)	$V_{S\ ini}$ (km/s)
Sandstone	0.15	2650	2402.5	4	2.389
Shale	0.3	2700	2190	2	0.801

3.1.2.2. Evolution of geometry and finite strain. A normal fault DEM simulation with dimensions and boundary conditions similar to Figure 2a was run in the fine assemblage. The number of particles in this DEM model is 180,000. Figure 9 shows the evolution of the model geometry (left), shear strain (center), and volumetric strain (right) at 20, 40, 60 and 90 m of fault displacement (Fig. 9a–d). Fault evolution is different than that of the coarse model. At early stages (up to 20 m of fault displacement, Fig. 9a), the fault consists of several narrow segments. Each of these segments is up to 10 m and displays high shear and volumetric strain (Fig. 9a center and

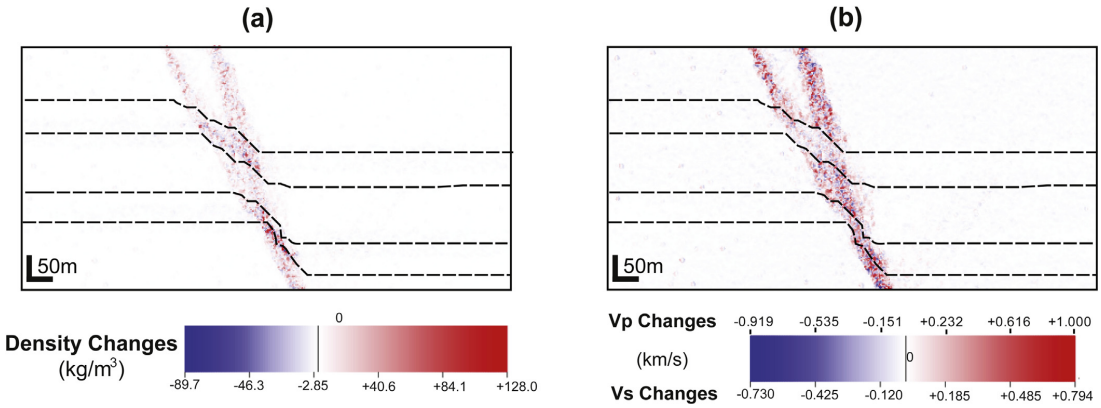

Figure 7. Changes of (a) Density and (b) Seismic velocities in the coarse model after 60 m of fault displacement. Black dashed lines are layer boundaries. Changes in the shale layers are more pronounced due to larger volumetric strains.

right). These fault segments dip 65° in the sandstone and 55–60° in the shale. At 40 m of fault displacement, the fault segments are larger and have accumulated more strain, but they have not totally linked yet into a through going fault (Fig. 9b). Only at about 60 m of fault displacement, the fault segments are fully linked into a main fault with a throw of about 50 m (Fig. 9c). From 50 m of fault displacement, a less steep fault in the footwall of the main fault develops (Fig. 9b, center). This second fault also consists of several fault segments displaying high strain. These fault segments dip 60° in the sandstone and 40–45° in the shale (Fig. 9c–d). From 60 m of fault displacement, smaller synthetic and antithetic normal faults develop linking the two major faults, especially in the center sandstone layer, but also in the top shale layer (Fig. 9c–d). The highest strains are localized in the major largest fault, and the shale layers accumulate more volumetric strain (Fig. 9d, center and right). The extent of fault related deformation (i.e. width of fault zone) is less than in the coarse model (Figs. 9 and 6). At early stages, the fault is mainly subjected to dilation (in red in the web version Fig. 9a, right), while at later stages both compaction and dilation occur along the two main faults, with the highest volumetric strains corresponding to the highest shear strains (Fig. 9b–d, right). The resolution of the fine model is higher than that of the coarse model, allowing capturing more details of fault formation, e.g. where the fault segments connect, as well as minor synthetic and antithetic faults that link the two major faults. Smaller particles give narrower fault zones. The particle size can also be responsible for the difference in fault dip angles between the two DEM models, but these differences can also be due to slight variations in the bulk properties of the assemblages.

3.1.2.3. Change of seismic properties. As in the coarse model, we choose the fine normal fault model at 60 m of fault displacement (Fig. 9c) to compute the change of elastic properties due to faulting. The same initial rock properties for sandstone and shale (Table 3) are assigned to the unfaulted fine model. Equations 1–4 are used to modify the initial elastic properties using the computed finite volumetric strain. Figure 10 shows the changes in density (Fig. 10a) and seismic velocities (Fig. 10b) in the fine model at 60 m of fault displacement. Since the shale layers accrued more volumetric strains, these layers exhibit the highest relative changes of elastic properties (Fig. 10). The lateral extent of faulting is less than in the coarse model (Figs. 10 and 7), which results in less impact of the fault zone on its seismic image (section 3.2).

3.2. Simulated seismic imaging

For both the coarse and fine models, the values of density and seismic velocities after 60 m of normal fault displacement (Figs. 7 and 10) were used to compute the corresponding reflectivity grids with a 0° incident angle (Fig. 15a and b, first column). A few sensitivity studies were run to illustrate the impact of the fault on the resulting seismic images. The parameters explored here are the illumination direction (model and survey dependent in real cases) and the wave frequency. Comparison of seismic amplitudes and input elastic properties along interpreted reflectors was also performed, to assess the potential of the different seismic images for predicting fault architecture and internal properties.

3.2.1. Impact of illumination direction

The illumination direction has an impact on the total fault volume illuminated in the seismic image. The PSDM simulator was applied for a 1.5 km thick homogeneous overburden with a P-wave velocity of 4.0 m/s and shear wave velocity 2.389 m/s, zero-phase Ricker pulses of 10–40 Hz main frequency (a Ricker pulse is a special type of wavelet defined by its dominant frequency, and zero-phase means the wavelet is symmetrical with a maximum at time zero), and three different illumination directions (Figs. 11 and 12). The survey consists of a single streamer centered at the fault for the specular illumination, or offset towards the footwall or hanging wall for the left and right side illuminations, respectively.

Specular illumination (i.e., following Snell's law) is good for imaging reflectors; it corresponds to illumination vectors perpendicular to the reflectors, which in this case are horizontal outside the fault zone (the specular illumination is then vertical). If specular illumination exists, the corresponding reflectors dominate the seismic image, as in the case of the coarse normal fault model (Fig. 11, first column). However, some seismic energy related to diffractions from the fault is still visible especially at higher frequencies (Fig. 11, first column). The fault thus impacts the seismic image. The illuminations from the left or right sides, corresponding to different wave propagation directions, do not contain specular energy from the flat reflectors, but only diffracted energy from the fault (Fig. 11, second and third columns). The illumination from the

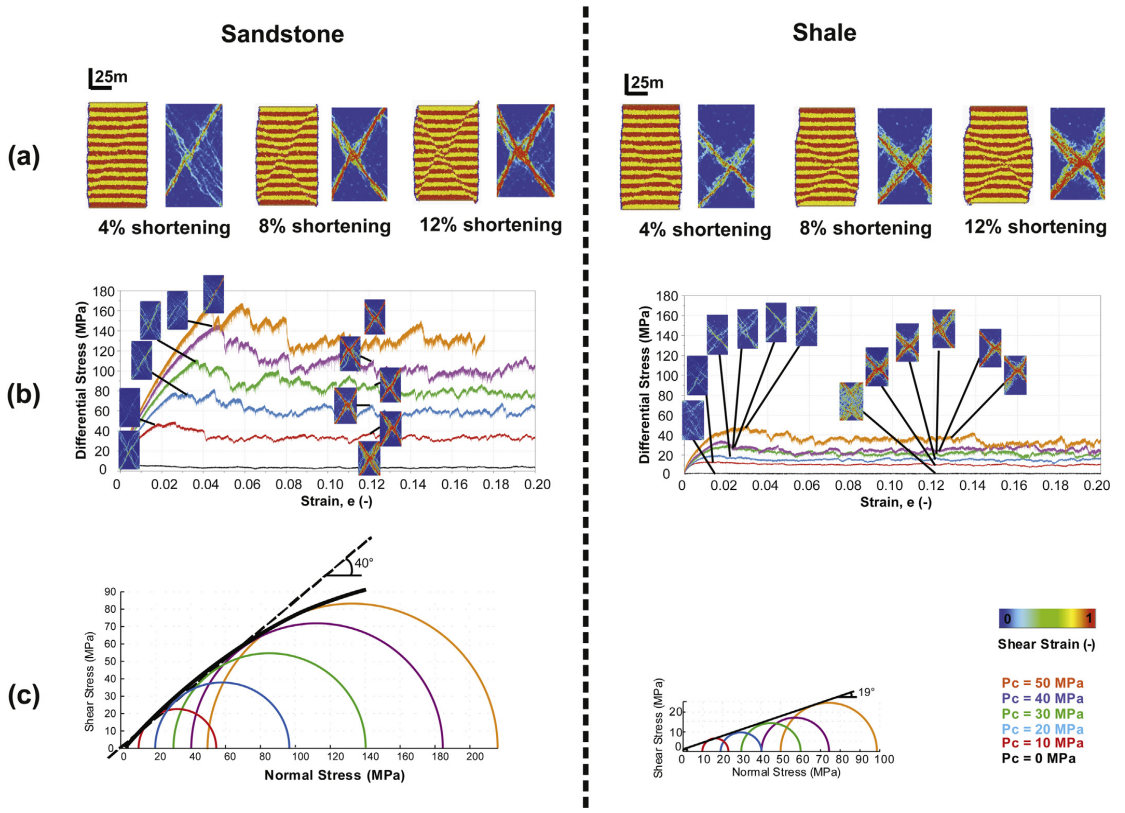

Figure 8. Bulk response of the fine sandstone and shale assemblages for the input particle properties of Table 1. (a) Biaxial compressive simulations under 20 MPa confining pressure at three shortening stages (left is geometry and right is shear strain). (b) Axial strain vs. differential stress curves. Rectangular images are samples colored by shear strain at different values of axial strain. (c) Failure envelopes from biaxial simulations.

footwall side (i.e., left side) produces an image with low amplitude values in which it is difficult to distinguish the two shale layers or to associate the reflections and diffractions to the fault structure. Higher amplitudes are visible at the top of the lower shale layer, which is offset (Fig. 11, second column). The illumination from the hanging wall side (i.e., right side), however, highlights the shale layers in the fault zone (particularly at frequencies of 20 Hz or more, Fig. 11, third column). These shale layers, which experienced higher finite strains than the sandstone layers (Figs. 6c and 7), are indicated by higher amplitude values. The changes in amplitude seem to correlate with the amount of finite strain, with lower amplitude values in the upper less deformed shale layer, and higher amplitude values in the lower more deformed one (Fig. 11, third column). For the left or right side illuminations, diffractions are related to the structural complexity of the fault zone (Fig. 11, right), but also to the irregular, jagged geometry of the shale/sandstone layer boundaries (Fig. 11, second and third columns).

Figure 12 shows the corresponding seismic images for the fine normal fault model. Even if the general aspect of the seismic images for the fine model (Fig. 12) is similar to those for the coarse model (Fig. 11), there are significant differences. In fact, using the coarse and fine models is an effective way to test the potential of seismic to differentiate between the fault related structure of these models (Figs. 6c and 9c). Specular illumination in the fine model highlights mainly the shale layers and their folding without major diffractions associated to the two fault segments (Fig. 12, first column). The small offset of the top of the upper shale layer is visible by a decrease of the amplitude value. The smaller fault segment towards the footwall of the main fault is almost not noticeable, but just indicated by a gentle downward bending of the upper shale reflectors (Fig. 12, first column). Diffractions can be detected but are difficult to interpret. Diffractions associated to reflectivity changes within the fault zone have large impact on the resulting image. Although it is easy to delimit the offset of the main fault, it is difficult to tell that there is another smaller fault segment, even at high frequencies (Fig. 12, first column). Footwall illumination gives low amplitude images (Fig. 12, second column). However, some extra information can be extracted from these images. The folding of the shale layers associated to the main fault segment generates higher amplitude reflections, either by significant thinning of the layer (e.g. lower shale layer) or layer offset (e.g. top shale layer). The smaller fault segment in the top upper shale layer is marked by diffracted energy (Fig. 12, second column). Hanging wall illumination (Fig. 12, third column) illuminates directly the main fault plane and the steeply dipping shale layers within the fault zone. The smaller fault segment, however, is not distinguishable because its related diffractions interact with those of the main fault segment.

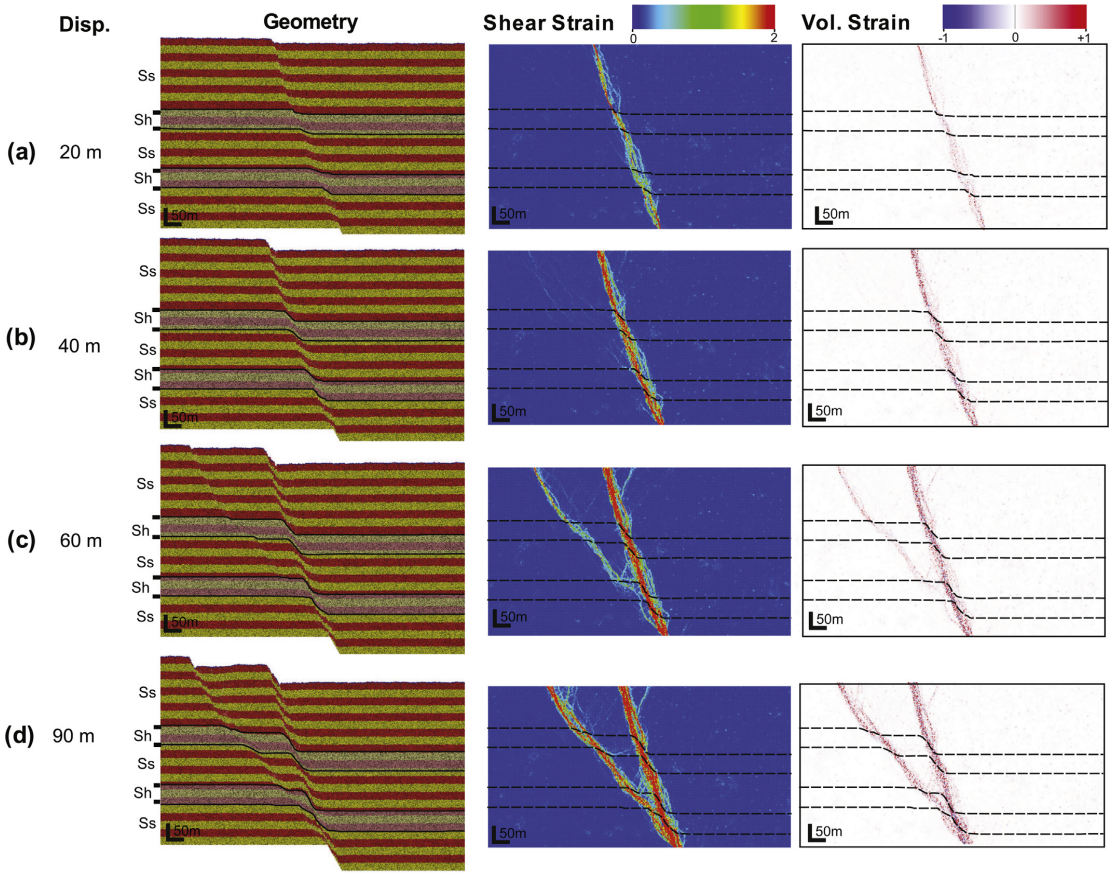

Figure 9. Evolution of the fine DEM normal fault simulation at: (a) 20, (b) 40, (c) 60 and (d) 90 m of fault displacement. Left is geometry, center is shear strain, and right is volumetric strain. Ss and Sh represent sandstone and shale layers respectively. Black lines are layer boundaries.

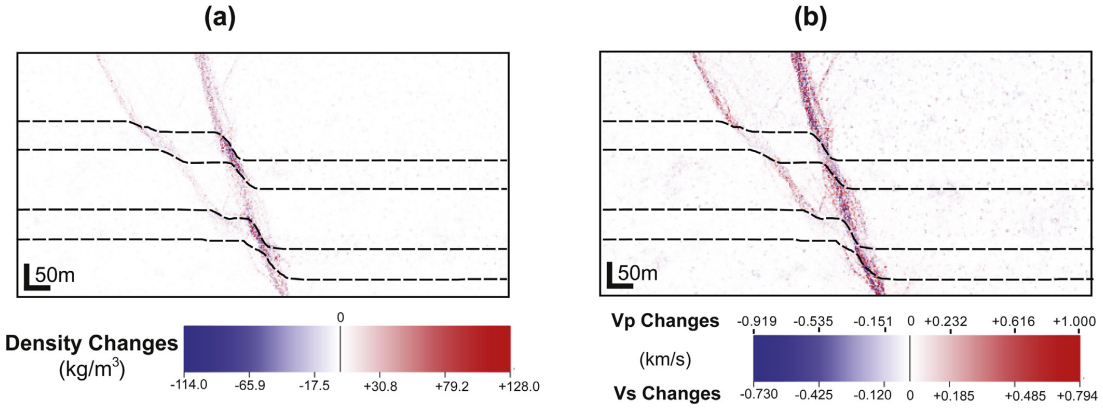

Figure 10. Changes of (a) Density and (b) Seismic velocities in the fine model after 60 m of fault displacement. Black dashed lines are layer boundaries. Changes in the shale layers are more pronounced due to larger volumetric strains. Density changes are more pronounced than in the coarse model (Fig. 7).

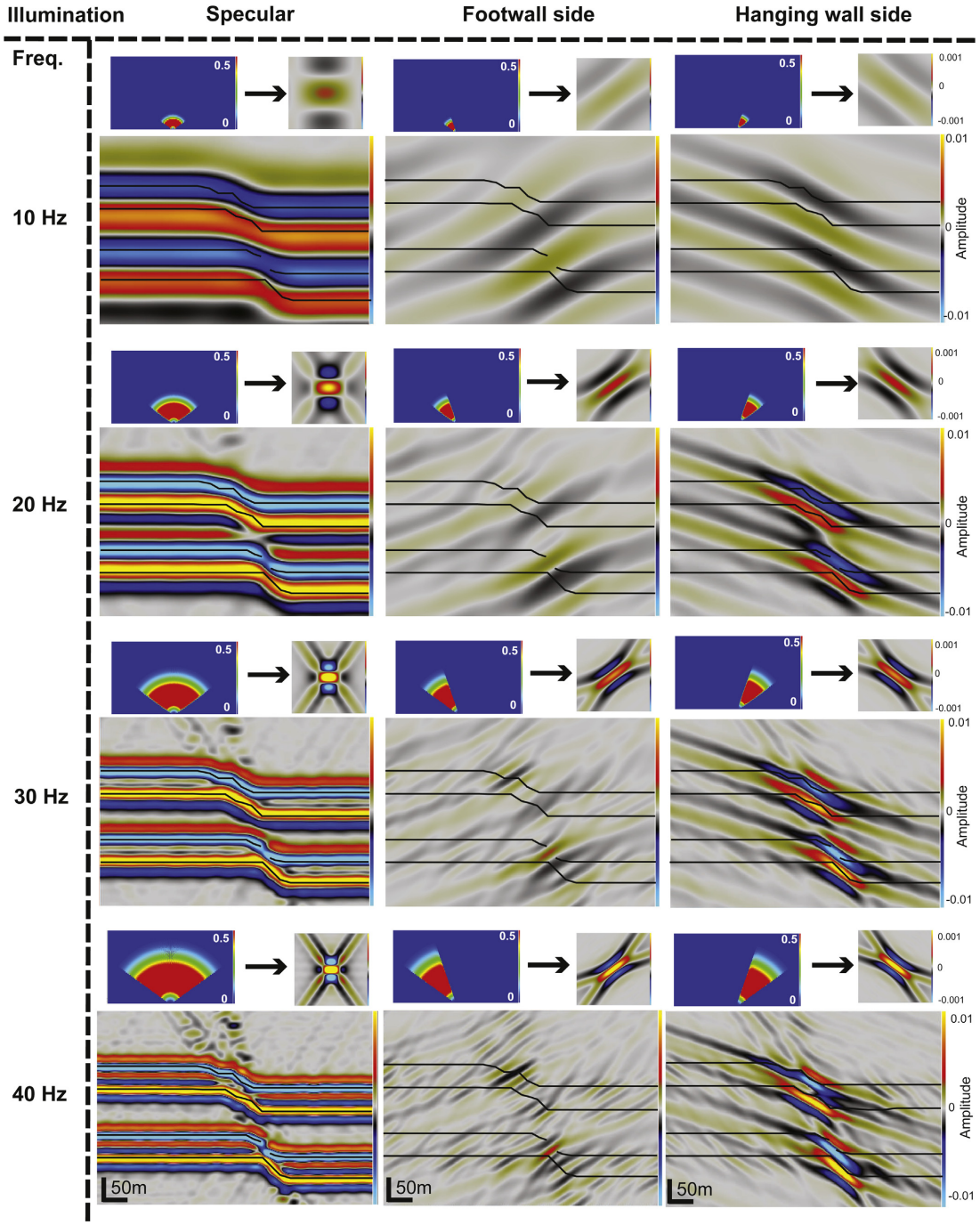

Figure 11. PSDM seismic images of normal fault coarse model at 60 m of fault displacement. The columns correspond to three different illumination directions: direct (left), footwall or left side (center), and hanging wall or right side (right). The rows correspond to four different frequencies of an incoming zero-phase Ricker pulse: 10 (first row), 20 (second row), 30 (third row), and 40 Hz (fourth row). At the top of each seismic image the PSDM filter and corresponding point spread function or PSF are shown. The overburden is 1.5 km and is homogeneous. Black lines are layer boundaries.

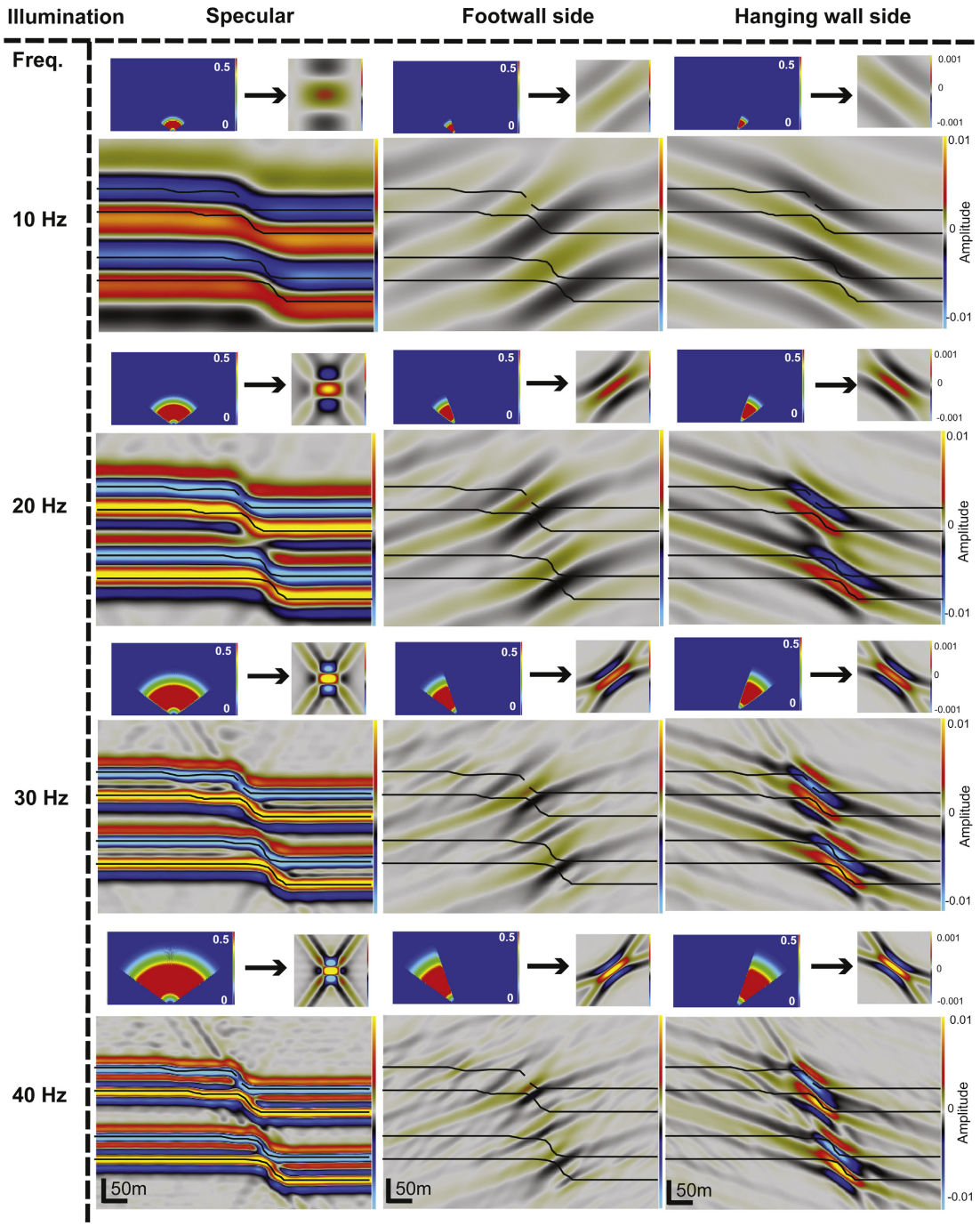

Figure 12. PSDM seismic images of normal fault fine model at 60 m of fault displacement. The columns correspond to three different illumination directions: direct (left), footwall or left side (center), and hanging wall or right side (right). The rows correspond to four different frequencies of an incoming zero-phase Ricker pulse: 10 (first row), 20 (second row), 30 (third row), and 40 Hz (fourth row). At the top of each seismic image the PSDM filter and corresponding point spread function or PSF are shown. The overburden is 1.5 km and is homogeneous. Black lines are layer boundaries.

3.2.2. Impact of frequency

Wave frequency is one of the parameter controlling the resolution of the fault in the resulting seismic image. In the coarse model, for small frequency wavelets (10–20 Hz), the vertical resolution is low (Fig. 11, first and second rows). The reflectors are continuous in the vertical and horizontal direction, which make difficult to distinguish the sandstone and shale layers or to interpret the normal fault (Fig. 11, first and second rows). For specular illumination, the top reflector is continuous, and for the left and right side illuminations, amplitude values are low (Fig. 11, first and second rows). From 30 Hz and higher frequencies, the two shale layers are distinguishable and the diffractions associated to the fault are visible (Fig. 11, third and fourth rows). Breaks or offsets in the layer boundaries, are marked by low amplitude values in the images produced by specular illumination, and by diffracted energy in the images produced by footwall or hanging wall directed illumination (Fig. 11, third and fourth rows).

For the fine model, at low frequency (10 Hz) the resulting seismic images (Fig. 12, first and second rows) are almost identical to those of the coarse model (Fig. 11, first and second rows). However, amplitude values are slightly higher for the fine model where the main fault is closer to a single plane. From 20 Hz, the fault structure and irregular geometry of the layer boundaries are more evident (Fig. 12, second row). At 30 and 40 Hz, the impact of the smaller fault segment is visible mostly in the upper shale layer in the three illumination images, and the diffracted energy is more important for the left and right side illuminations (Fig. 12, third and four rows).

3.2.3. Reflector geometry and associated amplitude

In an attempt to perform a more quantitative interpretation of the seismic images, we extract the amplitude values along selected profiles in the seismic images produced by specular illumination (Figs. 11 and 12, first column). Although there are several seismic attributes that help in the interpretation and characterization of faults (e.g., Dutzer et al., 2010; Iacopini and Butler, 2011; Iacopini et al., 2012), we decided to focus only on the amplitude response of the fault zone at several wave frequencies as a proof of concept of our workflow. The selected profiles correspond to the interpreted top interfaces of the shale layers in the seismic images (Figs. 13b and 14b). The extraction of the amplitudes was performed in a window 10 m above and below the interpreted reflector, using a root mean square (RMS) computation, and for wave frequencies from 10 to 40 Hz (Figs. 13a and c, and 14a and c). The amplitude profiles are compared to the RMS input elastic properties along the same interpreted reflector paths, in order to evaluate the correlation between amplitude anomalies and variations of elastic properties controlled by fault structure. For comparison, the RMS amplitude, density, and P-wave velocity are all scaled from 0 to 1 (Figs. 13a and c, and 14a and c).

In the coarse model (Fig. 13), the geometry of the interpreted reflector changes with the frequency of the wavelet (Fig. 13b): the higher the wave frequency is, the better the interpreted reflector matches the shale/sandstone interface and more information can be obtained about the structure of the fault (Fig. 13). RMS amplitudes (black lines in Fig. 13a and c) are similar for the interpreted upper and lower reflectors at 10 Hz (Fig. 13a and c, first column). From 20-Hz, there are differences due to higher dips of the interpreted lower reflector in the fault zone, which leads to higher relative changes in amplitude over shorter distances (Fig. 13 a and c, second to fourth columns). At relatively high frequencies (30–40 Hz), the interpreted lower reflector shows an offset, which is represented in the amplitude profile by a sharp drop right before the offset, followed by a sharp increase after the offset. The split of the fault into two segments is also visible in the interpreted upper reflector at these high frequencies, where it is defined by a pair of amplitude lows and highs (Fig. 13a and c, third and fourth columns).

The specular seismic images for the fine model (Fig. 14) present similar characteristics than those for the coarse model. The accuracy of the interpreted reflector geometry in following the actual

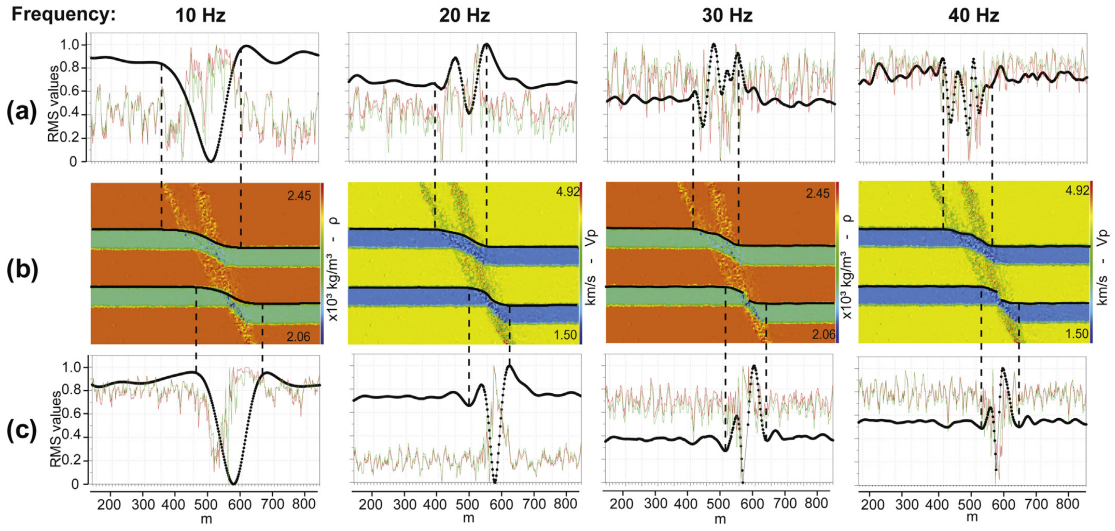

Figure 13. RMS amplitude (black line) and RMS property (density in red and P-wave velocity in green) along a swath 10 m above and below the interpreted top of the upper (a) and lower (c) shale layers, in the seismic profile with specular illumination of the normal fault coarse model (Fig. 11, left column). (b) Density ρ, P-wave velocity V_P, and interpreted reflectors (black lines). The four columns in (a) and (c) correspond to different frequencies of an incoming zero-phase Ricker pulse: 10 (first column), 20 (second column), 30 (third column), and 40 Hz (fourth column). Dotted lines in (a) and (c) indicate the area of influence of the fault. (For interpretation of the references to color in this figure legend, the reader is referred to the web version of this article.)

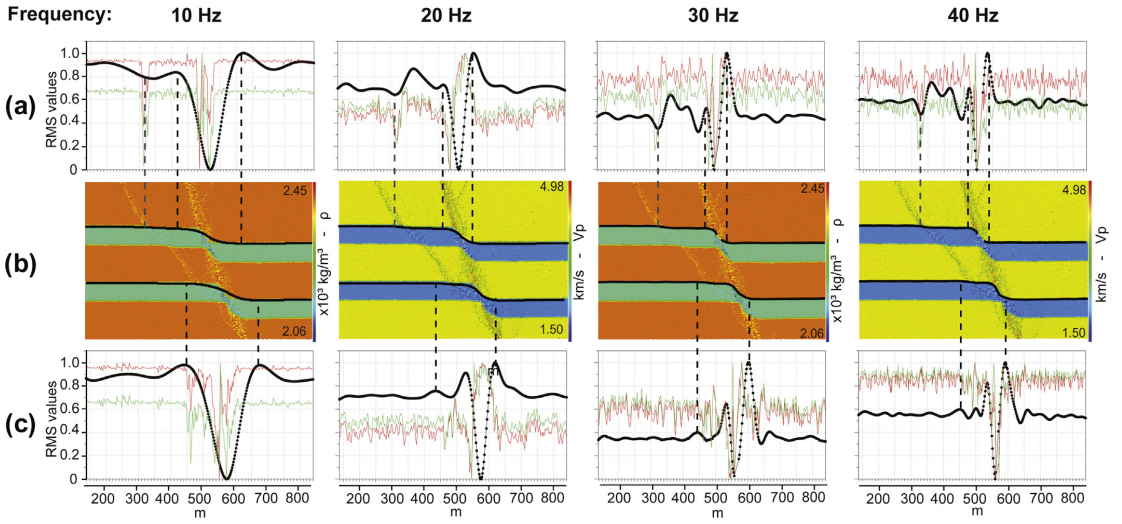

Figure 14. RMS amplitude (black line) and RMS property (density in red and P-wave velocity in green) along a swath 10 m above and below the interpreted top of the upper (a) and lower (c) shale layers, in the seismic profile with specular illumination of the normal fault fine model (Fig. 12, left column). (b) Density ρ, P-wave velocity V_P, and interpreted reflectors (black lines). The four columns in (a) and (c) correspond to different frequencies of an incoming zero-phase Ricker pulse: 10 (first column), 20 (second column), 30 (third column), and 40 Hz (fourth column). Dotted lines in (a) and (c) indicate the area of influence of the fault. (For interpretation of the references to color in this figure legend, the reader is referred to the web version of this article.)

shale/sandstone boundary increases with the frequency (Fig. 14). At a wave frequency of 10 Hz, the interpreted reflectors geometry and the extracted RMS amplitudes are very similar to those of the coarse model, with no further details of fault structure (Fig. 14a and c, first column). From 20 Hz wave frequencies, the second smaller fault segment is indicated by amplitude changes, especially in the interpreted upper reflector, (Fig. 14a and c, second column). At 30 and 40 Hz, the offset of the upper reflector by the main fault, is shown by a trough and peak in the amplitude profile. A smaller trough and peak in the amplitude profile also mark the smaller fault segment (Fig. 14a, third and fourth columns). The interpreted lower reflector has approximately the same geometry and RMS amplitude variations than in the coarse model (Figs. 14b–c and 13b–c).

3.2.4. Amplitude and elastic properties correlation

Figures 13 (a and c) and 14 (a and c) show the variation of the input RMS density (red lines in the web version) and P-wave velocity (green lines in the web version) along the interpreted reflectors for a window of 10 m above and below the reflector. The shear-wave velocity is not presented, because it is directly related to the P-wave velocity (Equation (4)). In the coarse model, changes in density and P-wave velocity in the fault zone correlate well with amplitude changes (Fig. 13). This correlation increases with wave frequency. Along the interpreted upper reflector at a wave frequency of 10 Hz, the presence of two fault segments is clear in the density and P-wave velocity profiles, but not in the amplitude profile (Fig. 13a, first column). From 20 Hz, the changes of acoustic properties and amplitude are approximately in phase (Fig. 13a, second column). At 30 and 40 Hz, a pair of troughs and highs in both the acoustic properties and amplitude profiles clearly indicates the two fault segments (Fig. 13a, third and fourth columns). At these high frequencies amplitude and acoustic properties variations are practically in phase. Along the interpreted lower reflector at low wave frequencies of 10–20 Hz, the relative changes of acoustic properties and amplitude are almost similar, although the acoustic properties and amplitude variations are out of phase at 10 Hz (Fig. 13c, first and second columns). From 30 Hz, a trough and peak in both the acoustic properties and amplitude profiles mark the offset of the lower reflector (Fig. 13c, third and fourth columns). The acoustic properties fluctuations, however, are larger than those of the amplitude. At 40 Hz, the amplitude variation correlates well with the changes in acoustic properties (Fig. 13c, fourth column).

The higher resolution of the fine model results in smaller fluctuations in acoustic properties along the interpreted reflectors than those for the coarse model (Fig. 14). Along the interpreted upper reflector at low wave frequencies of 10–20 Hz, the smaller fault segment clearly marked by the acoustic properties variations, is less detectable in the amplitude profiles. An abrupt drop in both acoustic properties and amplitude indicates the main fault segment, although amplitude and acoustic properties are slightly out of phase (Fig. 14a, first and second columns). At 30 and particularly 40 Hz, the acoustic properties and amplitude variations correlate well. Both, the smaller and main fault segments are visible (Fig. 14a, third and fourth columns). Along the interpreted lower reflector, the profiles of acoustic properties and amplitude are similar to those of the coarse model, but with smaller fluctuations (Fig. 14c). A large drop in acoustic properties and amplitude mark the main fault, although acoustic properties and amplitude are out of phase at low frequencies of 10–20 Hz (Fig. 14c, first and second columns). At higher frequencies of 30 and particularly 40 Hz, acoustic properties and amplitude variations are in phase and correlate well (Fig. 14c, third and fourth columns). Interestingly, neither the acoustic properties nor the amplitude variations at any of the chosen frequencies seem to indicate a second fault segment in the lower reflector (Fig. 14c).

Overall, Figures 13 and 14 show that the correlation between amplitude and acoustic properties variations increases with wave frequency and the accuracy of the interpreted reflector. The amplitude profiles allow determining the lateral extent of fault related deformation (i.e. the fault zone) at the level of the

interpreted reflector (dotted black lines in Figs. 13 and 14). Changes in acoustic (and petrophysical) properties in the fault zone can also be determined from the amplitude variations (Figs. 13 and 14). For the coarse and fine models, the maximum changes in RMS amplitude (troughs and peaks) in the main fault segment correspond to changes of 20–25% in P-wave velocity from the host rock values (Figs. 7 and 10). This is a direct result of the assumed correlation between P-wave velocity variation and volumetric finite strain (Fig. 3). For the fine model, changes in amplitude in the small fault segment correspond to changes of 10–15% in P-wave velocity (Fig. 10). Changes in density are lower than changes in seismic velocities. In the largest troughs and peaks of the amplitude profiles for the coarse and fine models (Figs. 13 and 14), changes in porosity are 20–25% (Fig. 3). This corresponds to density changes of about 4–5% (Equation (2) and Table 3). This knowledge of the extent of fault related deformation as well as of the relative changes of rock properties in the fault zone is critical for the assessment of the sealing capacity of the fault.

4. Discussion and conclusions

We have presented a synthetic methodology to study the impact of fault zone structure on seismic images. Fault evolution was simulated with a DEM, which allowed us to study faulting at large scale and the impact on fault deformation of parameters such as rock competence, overburden stress, fault displacement and particle size. Although the mechanical behavior of the DEM is purely frictional (i.e., no unconfined compressive strength and no tensile strength) and particle sizes are large in the coarse and fine models, the models were able to capture complex features of fault evolution and produce realistic fault geometries and strain fields. Both models display a fault zone initially consisting of isolated fault segments that later link. Particle size controls fault evolution, with the fine model displaying narrower fault zones and fault linkage at later stages. This behavior is also observed in sand and clay analogue models of faulting (Eisenstadt and Sims, 2005). The differences between the coarse and fine models can be seen as a numerical issue resulting from the particle sizes. However, they can also reflect reality. Smaller particles or grains allow more localization. The range of particle sizes can therefore be used as an advantage to simulate a large spectrum of fault geometries and strain fields observable in nature. Our DEM models do not have the complexity of the smaller-scale, bonded DEM models of Schöpfer et al. (2007), which require high tensile strengths; or the resolution of the DEM models of Egholm et al. (2008), which focus on clay smearing at the outcrop scale. The role of different loading configurations, which can produce similar fault geometry but dissimilar incremental and permanent strain (Lewis et al., 2007) is also not considered.

Seismic imaging requires an input cube of elastic properties (density, V_P and V_S). However after faulting, these properties are difficult to retrieve. The effect of large, permanent strain on elastic properties is poorly understood. At the magnitudes of finite strain in fault zones, simple linear laws that relate stress to strain such as elasticity are not applicable, and finite strain is the main reliable variable that we can take into account. The presented DEM models do not address processes at the grain scale and so there are challenges relating laboratory studies to the bulk mechanical behavior of the DEM. Therefore, the estimation of the changes of seismic properties due to finite strain has to be simple and empirical due to the complexity of the problem. As stated by Hatchell and Bourne (2005) and Couples et al. (2007), a simple relationship between permanent strain and acoustic properties at large scale, although probably inaccurate, is sufficient to assess the impact of faulting on seismic data. Equations 1–4 allow computing the change of seismic properties with finite volumetric strain in the modeled fault zone. In the future, we could add more information to the link between geomechanics and seismic modeling, such as the impact of shear strain and fracturing on seismic properties. However, we most probably still have to rely on empirical relations to link these two.

The application of the PSDM simulator to the mechanically derived reflectivity field provides a way to evaluate the acquisition and processing parameters required to better image the fault zone. Even if the ray-based PSDM simulator relies on some assumptions (e.g. single scattering and local plane wavenumber), the sensitivity analysis introduced here approaches closer the reality of seismic acquisition and processing than industry standard, post-stack seismic modeling techniques such as 1D convolution. The two parameters presented, illumination direction and frequency, already include survey geometry, wave type, background media and overburden, all of which have a large impact on the seismic image. Other parameters and more complex cases (e.g., lateral variations in overburden) will be considered in future work. In both the coarse and fine normal fault models with specular illumination, higher wave frequencies (30 Hz and more) result in better definition and higher diffracted energy from the fault zone (Figs. 11 and 12, first column). The diffraction part of the seismic energy really helps to characterize the fault zone. Diffractions make possible determining the lateral and vertical extent of faulting without focusing only on reflector offsets (Figs. 11 and 12, first column). The depth of our model (about 1.5 km) is shallow in conventional seismic. At this depth, the typical dominant frequency can be higher than 30 Hz. For reservoirs deeper than 3 km (which is a typical case in the North Sea), it is sometimes difficult to obtain frequencies higher than 30 Hz, and reflections can hide details of the fault structure. Changing the illumination direction can help to highlight the internal structure of the fault zone, and therefore this parameter can be tested during seismic acquisition for specific fault characterization. Side illumination targets directly the fault plane. Hanging wall side illumination shows well the structure of the main fault zone, but not the smaller fault segment in the footwall of the main fault (Figs. 11 and 12, third column). Footwall side illumination results in low amplitude images, however, only this illumination makes the smaller fault segment of the fine model visible (Fig. 12, second column). Both frequency and illumination direction are important for imaging the fault zone.

This work emphasizes the impact of fault zone internal structure on the resultant seismic image. Indeed, the general interpretation of faults as 2D surfaces is too simplistic. Figure 15 shows a comparison between the coarse model (Fig. 15a), the fine model (Fig. 15b), and a planar 60° dipping normal fault model (Fig. 15c). The planar fault model (Fig. 15c, left) represents how faults are typically interpreted; with only reflector offsets and no fault related strain (folding, minor faulting, fracturing, etc.). Seismic images for a 40 Hz, zero-phase Ricker pulse, a 1.5 km homogeneous overburden with a P-wave velocity of 4 m/s, and three illumination patterns are presented for the three models (Fig. 15a–c, second to fourth columns). Even though the general aspect of the seismic images is similar, there are clear differences between them. For the specular illumination images, diffractions are critical to delimit the extent of faulting in the coarse and fine models (Fig. 15a–b, second column), and should be used to guide the correct interpretation of faults in seismic data. Diffractions, however, are almost absent in the planar fault model (Fig. 15c, second column). For the side illumination images, reflections are continuous outside the main fault in the planar fault model (Fig. 15c, third and fourth columns), but are discontinuous and display more amplitude variability in the coarse and fine models (Fig. 15a–b, third and fourth columns). For the hanging wall side illumination, it is interesting to see how the

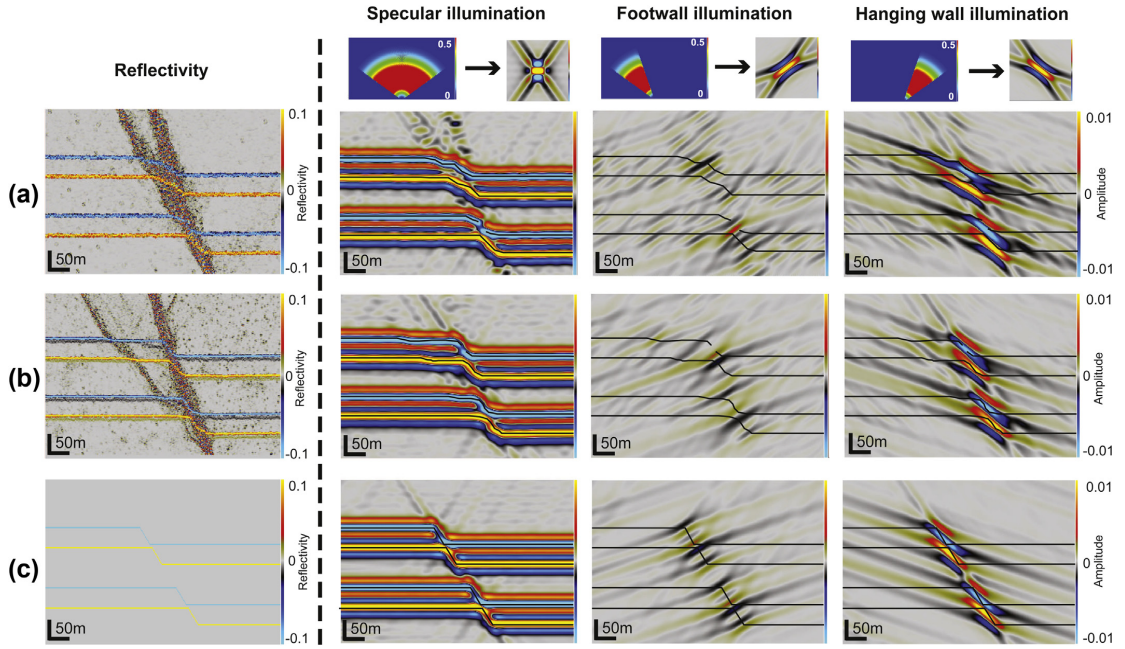

Figure 15. Seismic profiles of (a) Normal fault coarse model, (b) Normal fault fine model, and (c) Planar normal fault model. First column is the input reflectivity. Second to fourth columns correspond to different illumination directions: Specular (second column), from footwall (third column), and from hanging wall (fourth column). The seismic images were generated with a 40 Hz, zero-phase Ricker pulse. The overburden is 1.5 km and is homogeneous. Black lines in second to fourth columns are layer boundaries.

width of the high amplitude reflections in the fault zone decreases from the coarse model (Fig. 15a, fourth column), to the fine model (Fig. 15b, fourth column), and to the planar fault model (Fig. 15c, fourth column); giving a clear indication of the thickness of the fault zone.

The analysis of RMS amplitude along interpreted reflectors helps defining the architecture of the fault zone. The higher the frequency band is, the closer the interpreted reflectors are to the layer boundaries and the better the definition of fault architecture (Figs. 13 and 14). However, at high wave frequencies, e.g. 40 Hz, the interpreted reflector and its associated RMS amplitude can capture small fluctuations of the layer interface, which may interfere with the interpretation of the fault geometry. For example in the fine model, it can be difficult to distinguish the smaller fault segment along the interpreted lower shale/sandstone interface at 40-Hz (Fig. 14c, fourth column). When working at high frequencies, the interpreter may need to disregard small amplitude variations (e.g. small layer fluctuations), and focus on larger amplitude changes that may indicate faulting (e.g. the slightly higher peak defining the smaller fault segment in Fig. 14c, fourth column).

In our synthetic modeling, changes in RMS amplitude along the interpreted reflectors are directly correlated to changes in acoustic properties, especially at high wave frequencies (Figs. 13 and 14, third and fourth columns). This may provide a way to estimate the changes in acoustic properties in the fault zone with respect to the host rock, but pending that amplitudes have been properly preserved while processing and imaging. Seismic amplitude (black lines in Figs. 13 and 14), although displaying less variability than the input acoustic properties (red and green lines in Figs. 13 and 14), gives an estimate of the average gradient of change and maximum change of acoustic properties in the fault zone. Even though RMS amplitude was the only attribute used for the qualitative interpretation of the seismic images, this information is critical for reconstructing the distribution of rock properties in the fault zone. Although acoustic and fluid flow (e.g., permeability) rock properties are not directly correlated, contrast changes of seismic amplitude across faults could be a direct indicator of the permeability distribution, which will be critical for determining fault sealing. The study of more seismic attributes (e.g. dip and azimuth, curvature, coherence or tensor, Dutzer et al., 2010) could help to a better definition of the petrophysical properties of the model, but require a deeper investigation of the relation between the seismic data and each of these properties.

The proposed workflow is a step forward towards the seismic characterization of complex fault zones. The coarse and fine DEM models give insight on fault evolution at large scales. Sensitivity analyses of two seismic parameters, illumination direction and wave frequency, give information on how to handle seismic data for fault interpretation: During acquisition (e.g., by focusing on an illumination from the hanging wall rather than from the footwall), processing (e.g., by focusing on diffracted rather than reflected energy), and interpretation (e.g., by analyzing amplitude variations). The methodology is here presented as a proof of concept in 2D, but it can be extended to 3D. 2D does not allow us to investigate several factors that are key during faulting, including variations of fault geometry (e.g. fault dip) and fault displacement, and fault propagation and linkage along strike. In an actual faulted volume, a single illumination direction is most probably not sufficient to image the fault network. Ongoing work is focusing on running such 3D simulations. These simulations allow us to explore additional geologic processes such as changes of fault displacement and fault interaction along strike, plus exploiting the true potential of the

PSDM simulator with realistic surveys, overburdens, etc. The validity of seismic attributes analyses to determine the extent of fault damage, isolate the fault damage volume, and predict its internal architecture and properties (Dutzer et al., 2010), can also be evaluated. Future work will also include seismic imaging simulations of a real 3D case scenario (e.g. outcrop) with well-constrained fault related deformation and petrophysical properties (e.g., Rotevatn and Fossen, 2011).

Acknowledgments

This work was funded by the Norwegian Research Council through the project "Seismic Imaging of Fault Zones" (NFR-PETROMAKS, project no. 210425/E30). Mechanical modeling was performed using the program cdem2D by Stuart Hardy, finite strain was computed using the program SSPX by Nestor Cardozo and Richard Allmendinger, seismic imaging simulation was performed in SeisRoX (NORSAR), and analysis of seismic amplitudes was done in Petrel (Schlumberger).

References

Abe, S., van Gent, H., Urai, J.L., 2011. DEM simulation of normal faults in cohesive materials. Tectonophysics 512, 12–21.
Allmendinger, R.W., Cardozo, N., Fisher, D., 2012. Structural Geology Algorithms: Vectors and Tensors. Cambridge University Press, 302 p.
Aarland, R.K., Skjerven, J., 1998. Fault and fracture characteristics of a major fault zone in the northern North Sea: analysis of 3D seismic and oriented cores in the Brage Field (Block 31/4). In: Geological Society, London, Special Publications, vol. 127, pp. 209–229.
Bastesen, E., Braathen, A., 2010. Extensional faults in fine grained carbonates – analysis of fault core lithology and thickness-displacement relatioships. J. Struct. Geol. 32, 1609–1628.
Ben-Zion, Y., Peng, Z., Okaya, D., Seeber, L., Armbruster, J.G., Ozer, N., Michael, A.J., Baris, S., Aktar, M., 2003. A shallow fault-zone structure illuminated by trapped waves in the Karadere-Duzce branch of the North Anatolian Fault, western Turkey. Geophys. J. Int. 152, 699–717.
Cardozo, N., Allmendinger, R.W., 2009. SSPX: a program to compute strain from displacement/velocity data. Comput. Geosci. 35, 1343–1357.
Childs, C., Watterson, J., Walsh, J.J., 1996. A model for the structure and development of fault zones. J. Geol. Soc. Lond. 153, 337–340.
Childs, C., Manzocchi, T., Walsh, J.J., Bonson, C.G., Nicol, A., Schöpfer, M.P.J., 2009. A geometric model of fault zone and fault rock thickness variations. J. Struct. Geol. 31, 117–127.
Couples, G., Ma, J., Lewis, H., Olden, P., Quijano, J., Fasae, T., Maguire, R., 2007. Geomechanics of faults: impacts on seismic imaging. First Break 25, 83–90.
Cundall, P.A., Strack, O.D.L., 1979. A discrete numerical model for granular assemblies. Geotechnique 29, 47–65.
Davatzes, N.C., Eichhubl, P., Aydin, A., 2005. Structural evolution of fault zones in sandstone by multiple deformation mechanisms: Moab fault, southeast Utah. GSA Bull. 117, 135–148.
Drottning, Å., Branston, M., Lecomte, I., 2009. Value of illumination-consistent modeling in time-lapse seismic analysis. First Break 27 (10), 75–83.
Dutzer, J.F., Basfor, H., Purves, S., 2010. Investigating fault sealing potential through fault relative seismic volume analysis. Petroleum Geology Conference. In: The Geological Society, London, vol. 7, pp. 509–515.
Egholm, D.L., Sandiford, M., Clausen, O.R., Nielsen, S.B., 2007. A new strategy for discrete element numerical models: 2. Sandbox applications. J. Geophys. Res. 112, B05204 http://dx.doi.org/10.1029/2006JB004558.
Egholm, D.L., Clausen, O.R., Sandiford, M., Kristensen, M.B., Korstgård, J.A., 2008. The mechanics of clay smearing along faults. Geology 36, 787–790.
Eichhubl, P., D'Onfro, P.S., Aydin, A., Waters, J., McCarty, D.K., 2005. Structure, petrophysics, and diagenesis of shale entrained along a normal fault at Black Diamond Mines, California – implications for fault seal. AAPG Bull. 89, 113–1137.
Eisenstadt, G., Sims, D., 2005. Evaluating sand and clay models: do rheological differences matter? J. Struct. Geol. 27, 1399–1412.
Faulkner, D.R., Jackson, C.A.L., Lunn, R.J., Schlische, R.W., Shipton, Z.K., Wibberley, C.A.J., Withjack, M.O., 2010. A review of recent developments concerning the structure, mechanics and fluid flow properties of fault zones. J. Struct. Geol. 32, 1557–1575.
Finch, E., Hardy, S., Gawthorpe, R.L., 2004. Discrete element modelling of extensional fault-propagation folding above rigid basement fault blocks. Basin Res. 16, 489–506.
Fisher, Q.J., Knipe, R.J., 1998. Fault sealing processes in siliciclastic sediments. In: Jones, G., Fisher, Q.J., Knipe, R.J. (Eds.), Faulting, Fault Sealing and Fluid Flow in Hydrocarbon Reservoirs, Geological Society, London, Special Publications, vol. 147, pp. 117–134.
Foxford, K.A., Walsh, J.J., Watterson, J., Garden, I.R., Guscott, S.C., Burley, S.D., 1998. Structure and content of the Moab Fault Zone, Utah, USA, and its implications for fault seal prediction. In: Jones, G., Fisher, Q.J., Knipe, R.J. (Eds.), Faulting, Fault Sealing and Fluid Flow in Hydrocarbon Reservoirs, Geological Society, London, Special Publications, vol. 147, pp. 87–103.
Færseth, R.B., 2006. Shale smear along large faults: continuity of smear and the fault seal capacity. J. Geol. Soc. Lond. 163, 741–751.
Gray, G.G., Morgan, J.K., Sanz, P.F., 2014. Overview of continuum and particle dynamics methods for mechanical modeling of contractional geologic structures. J. Struct. Geol. 59, 19–36.
Gjøystdal, H., Iversen, E., Lecomte, I., Kaschwish, T., Drottning, Å., Mispel, J., 2007. Improved applicability of ray tracing in seismic acquisition, imaging, and interpretation. Geophysics 72, SM261–SM271.
Hardy, S., 2008. Structural evolution of calderas: insights from two-dimensional discrete element simulations. Geology 36, 927–930.
Hardy, S., 2011. Cover deformation above steep, basement normal faults: insights from 2D discrete element modeling. Mar. Pet. Geol. 28, 966–972.
Hardy, S., 2013. Propagation of blind normal faults to the surface in basaltic sequences: insights from 2D discrete element modelling. Mar. Pet. Geol. 48, 149–159.
Hardy, S., Finch, E., 2005. Discrete-element modelling of detachment folding. Basin Res. 17, 507–520.
Hardy, S., Finch, E., 2006. Discrete element modelling of the influence of cover strength on basement-involved fault-propagation folding. Tectonophysics 415, 225–238.
Hardy, S., McClay, K., Anton Muñoz, J.A., 2009. Deformation and fault activity in space and time in high-resolution numerical models of doubly vergent thrust wedges. Mar. Pet. Geol. 26, 232–248.
Hatchell, P., Bourne, S., 2005. Rocks under strain: strain-induced time-lapse time shifts are observed for depleting reservoirs. Lead. Edge 24, 1222–1225.
Hoek, E., Brown, E.T., 1997. Practical estimates of rock mass strength. Int. J. Rock Mech. Min. Sci. 34, 1165–1186.
Holohan, E.P., Schopfer, M.P.J., Walsh, J.J., 2011. Mechanical and geometric controls on the structural evolution of pit crater and caldera subsidence. J. Geophys. Res. 116, B07202 doi:1029/2010JB008032.
Holt, R.M., Fjaer, E., Nes, O.M., Stenebraten, J.F., 2008. Strain sensitivity of wave velocities in sediments and sedimentary rocks. In: The 42nd US Rock Mechanics Symposium (USRMS). American Rock Mechanics Association.
Horsrud, P., SønstebØ, E.F., Bøe, R., 1998. Mechanical and petrophysical properties of North Sea shales. Int. J. Rock Mech. Min. Sci. 35, 1009–1020.
Hubbert, M.K., 1951. Mechanical basis for certain familiar geologic structures. GSA Bull. 62, 355–372.
Iacopini, D., Butler, R., 2011. Imaging deformation in submarine thrust belts using seismic attributes. Earth Planet. Sci. Lett. 302, 414–422.
Iacopini, D., Butler, R., Purves, S., 2012. Seismic imaging of thrust faults and structural damage: a visualization workflow for deepwater thrust belts. First Break 30, 77–84.
Jeanne, P., Guglielmi, Y., Cappa, F., 2012. Multiscale seismic signature of a small fault zone in a carbonate reservoir: relationships between VP imaging, fault zone architecture and cohesion. Tectonophysics 554–557, 185–201.
Kaschwich, T., Gjøystdal, H., Lecomte, I., 2011. Impact of diffraction on resolution of PSDM, extended abstract. In: 73rd EAGE Conference & Exhibition incorporating SPE EUROPEC 2011, Vienna, Austria, 23–26 May, P384.
Koledoye, B.A., Aydin, A., May, E., 2003. A new process-based methodology for analysis of shale smear along normal faults in the Niger Delta. AAPG Bull. 87, 445–463.
Lecomte, I., Kaschwich, T., 2008. Closer to Real Earth in Reservoir Characterization: a 3D Isotropic/Anisotropic PSDM Simulator. 2008 SEG Annual Meeting, 9–14 November. Society of Exploration Geophysicists, Las Vegas, Nevada.
Lecomte, I., 2008. Resolution and illumination analyses in PSDM: a ray-based approach. Lead. Edge 27, 650–663.
Lewis, M.A., Peng, Z., Ben-Zion, Y., Vernon, F.L., 2005. Shallow seismic trapping structure in the San Jacinto fault zone near Anza, California. Geophys. J. Int. 162, 867–881.
Lewis, H., Hall, S.A., Guest, J., Couples, G.D., 2007. Kinematically-equivalent but geomechanically-different simulations of fault evolution: the role of loading configurations. In: Jolley, S.J., Barr, D., Walsh, J.J., Knipe, R.J. (Eds.), Structurally Complex Reservoirs, Geological Society, London, Special Publications, vol. 292, pp. 159–172.
Li, X., Liu, Y., Liu, E., Shen, F., Qi, L., Shouli, Q., 2003. Fracture detection using land 3D seismic data from the Yellow River Delta, China. Lead. Edge 22, 680–683.
Long, J.J., Imber, J., 2010. Geometrically coherent continuous deformation in the volume surrounding a seismically imaged normal fault-array. J. Struct. Geol. 32, 222–234.
Long, J.J., Imber, J., 2012. Strain compatibility and fault linkage in relay zones on normal faults. J. Struct. Geol. 36, 16–26.
Manzocchi, T., Childs, C., Walsh, J.J., 2010. Faults and fault properties in hydrocarbon flow models. Geofluids 10, 94–113.
Mavko, G., Mukerji, T., Dvorkin, J., 2009. The Rock Physics Handbook: Tools for Seismic Analysis in Porous Media, second ed. Cambridge University Press, New York.
Mora, P., Place, D., 1993. A lattice solid model for the non-linear dynamics of earthquakes. Int. J. Mod. Phys. C 4, 1059–1074.

Nygård, R., Gutierrez, M., Bratli, R.K., Høeg, K., 2006. Brittle-ductile transition, shear failure and leakage in shales and mudrocks. Mar. Pet. Geol. 23, 201–212.
Oger, L., Savage, S.B., Corriveau, D., Sayed, M., 1998. Yield and deformation of an assembly of disks subject to a deviatoric stress loading. Mech. Mater. 27, 189–210.
Rotevatn, A., Fossen, H., 2011. Simulating the effect of subseismic fault tails and process zones in a siliciclastic reservoir analogue: implications for aquifer support and trap definition. Mar. Pet. Geol. 28, 1648–1662.
Schöpfer, M.P.J., Childs, C., Walsh, J.J., 2007. Two-dimensional distinct element modeling of the structure and growth of normal faults in multilayer sequences: 1. Model calibration, boundary conditions, and selected results. J. Geophys. Res. 112 (10), B10401.
Shtivelman, V., Marco, S., Reshef, M., Agnon, A., Hamiel, Y., 2005. Using trapped waves for mapping shallow fault zones. Near Surf. Geophys. 3, 91–97.
Sigernes, L.-T.W., 2004. Rock Physics of Extensional Faults and Their Seismic Imaging Properties (Doctoral thesis, monograph). Norwegian University of Science and Technology, 305 p.
Skurveit, E., Torabi, A., Gabrielsen, R.H., Zoback, M.D., 2013. Experimental investigation of deformation mechanisms during shear-enhanced compaction in poorly lithified sandstone and sand. J. Geophys. Res. Solid Earth 118, 4083–4100.
Solum, J.G., Davatzes, N.C., Lockner, D.A., 2010. Fault-related clay authigenesis along the Moab Fault: implications for calculations of fault rock composition and mechanical and hydrologic fault zone properties. J. Struct. Geol. 32, 1899–1911.
Terheege, J.H., Wassing, B.B.T., Orlic, B., Giger, S.B., Clennell, M.B., 2013. Constraints on the sealing capacity of faults with clay smears from discrete element models validated by laboratory experiments. Rock Mech. Rock Eng. 46, 465–478.
Thompson, N., Bennett, M.R., Petford, N., 2010. Development of characteristic volcanic debris avalanche deposit structures: new insights from distinct element simulations. J. Volcanol. Geotherm. Res. 192, 191–200.
Townsend, C., Firth, I.R., Westerman, R., Kirkevollen, L., Härde, M., Andersen, T., 1998. Small seismic-scale fault identification and mapping. In: Jones, G., Fisher, Q.J., Knipe, R.J. (Eds.), Faulting, Fault Sealing and Fluid Flow in Hydrocarbon Reservoirs, Geological Society, London, Special Publications, vol. 147, pp. 1–25.
van Gent, H.W., Holland, M., Urai, J.L., Loosveld, R., 2010. Evolution of fault zones in carbonates with mechanical stratigraphy - insights from scale models using layered cohesive powder. J. Struct. Geol. 32, 1375–1391.
Wibberley, C.A.J., Yielding, G., Di Toro, G., 2008. Recent advances in the understanding of fault zone internal structure: a review. In: Wibberley, C.A.J., Kurz, W., Imber, J., Holdsworth, R.E., Colletini, C. (Eds.), The Internal Structure of Fault Zones: Implications for Mechanical and Fluid-flow Properties, Geological Society, London, Special Publications, vol. 299, pp. 5–33.
Yielding, G., Bretan, P., Freeman, B., 2010. Fault seal calibration: a brief review. In: Jolley, S.J., Fisher, Q.J., Ainsworth, R.B., Vrolijk, P.J., Delisle, S. (Eds.), Reservoir Compartmentalization, Geological Society, London, Special Publications, vol. 347, pp. 243–255.
Zhang, J., Morgan, J.K., Gray, G.G., Harkins, N.W., Sanz, P.F., Chikichev, I., 2013. Comparative FEM and DEM modeling of basement-involved thrust structures, with application to Sheep Mountain, Greybull area, Wyoming. Tectonophysics 608, 408–417.
Zoback, M.D., 2010. Reservoir Geomechanics. Cambridge University Press, 461 p.
Zühlsdorff, L., Gjøystdal, H., Drottning, Å., Lecomte, I., Moen, S.I., Bolin, H., 2013. Modern ray-based modelling and simulated depth migration for survey planning and interpretation: a 3D VSP example. Geohorizons 18 (2), 27–37.

PAPER 2

Seismic characterisation of fault damage in 3D using mechanical and seismic modelling

Botter, Charlotte; Cardozo, Nestor; Hardy, Stuart; Lecomte, Isabelle; Paton, Gaynor & Escalona, Alejandro

Submitted to Marine and Petroleum Geology, January 2016.

2

Not available in UiS Brage due to copyright

PAPER 3

The impact of faulting and fluid flow on seismic images of a relay ramp

Botter, Charlotte; Cardozo, Nestor; Lecomte, Isabelle; Rotevatn, Atle & Paton, Gaynor

Submitted to Petroleum Geoscience, thematic set on fault & top seals, February 2016.

Not available in UiS Brage due to copyright

Appendices

Conference extended abstracts

Appendix 1

A1

Supplementary material to paper 3

Appendix 1

Addition to paper 3:

Quantitative analysis was not run in paper 3. However, cross plots between the seismic amplitude and the input properties, i.e. porosity and oil-saturation, are directly relevant for this thesis (e.g. workflow Figure 3). Figure 9 presents the seismic amplitude vs the input properties, e.g. porosity and oil saturation, of the base case of paper 3. Figure 9a plots the seismic amplitude versus the porosity for both the seismic volume corresponding to the geomodel volume (grey dots) and for the extracted geobody (colour dots) at the three stages of the flow simulation. To highlight the impact of porosity variation within the volume, we colour coded the sample points of the geobody by the fault enhancement attribute. At the beginning of the fluid flow simulation most of the geobody points are located within amplitudes of -0.006 to 0.006 and present high values of fault enhancement attribute (Figure 9a left). Most of the geobody points are located around porosity = 0.27, which matches the histogram distribution of porosity in the geomodel. Larger fault enhancement values, i.e. large probability of a fault, correspond to slightly higher amplitudes because all reflection in this cube is generated due to large porosity changes, i.e. fault damage zone. For the intermediate and final models (Figure 9a, middle and right), the seismic cube points are occupying the entire range of amplitudes. The extracted geobodies are mainly located near zero amplitude values with low probability of having a fault. The highest fault enhancement values are around porosity = 0.27 and are at large values of amplitude, i.e. up to -/+0.026. This is explained by stronger reflectivity contrast between oil and water in than between the damage zone and the host rock.

For the intermediate and final models, the seismic amplitude versus oil saturation is plotted in Figure 9b for the seismic cubes and the geobodies. Seismic amplitudes cover the range of oil saturation and are mainly positive, due to the larger amplitude values of the positive reflector corresponding to the thin oil layer at the top of the reservoir. The extracted geobodies are mainly defined by oil saturation greater than 0.55 with low fault enhancement values centred near zero amplitude. The highest values of the fault enhancement attribute correspond here to the probability of encountering a fluid contact

rather than a fault, and are therefore more related to larger amplitude values. By correlating the seismic amplitude to the input rock properties, we do not directly retrieve the rock properties from the seismic data, but we get better knowledge of the amplitude distribution related to the extracted geobody and the possible distribution of rock properties within it.

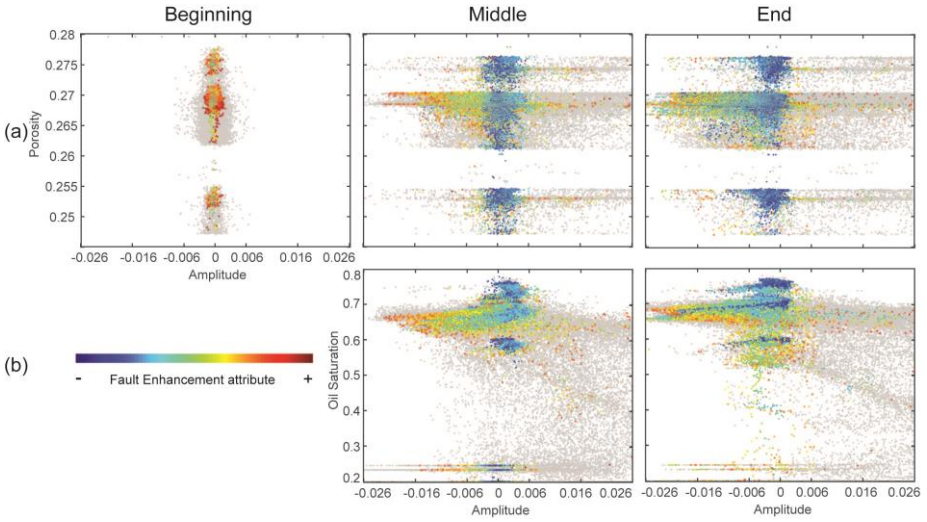

Figure 9: *Seismic amplitude versus (a) porosity and (b) oil saturation at the three stages of the fluid flow simulation (columns) for the base case. The grey dots correspond to the seismic cube reduced to the geomodel volume. The colour dots correspond to the geobody and are colour coded by the fault enhancement attribute (red = high and blue = low).*

Appendix 2

Extended abstract 1:

A2

Botter, Charlotte; Cardozo, Nestor; Hardy, Stuart; Lecomte, Isabelle & Escalona, Alejandro

Mechanical modelling and seismic imaging of fault zones.

*EAGE Fault and Top Seals Conference, Montpellier **2012**; 2012/10/01-03*

DOI: 10.3997/2214-4609.20142996

Accepted for oral presentation

Fault and Top Seals
Montpellier 2012

A08

Mechanical Modelling and Seismic Imaging of Fault Zones

C. Botter* (University of Stavanger), N. Cardozo (University of Stavanger), S. Hardy (ICREA), I. Lecomte (NORSAR) & A. Escalona (University of Stavanger)

SUMMARY

Faults are 3D zones of deformed rock that play a major role in controlling fluid flow in reservoirs. Fault zones are difficult to characterize: outcrops give limited view and seismic is limited by resolution and image quality. We propose an integrated approach to study fault zone evolution and its impact on seismic. We model fault zones using the discrete-element method (DEM). The finite strain of these models is used to condition seismic properties. Finally, seismic imaging of the DEM analogues is performed. An example is presented for a normal fault zone (60 m of fault displacement) in a 2D shale-sandstone layered model of size 1 x 0.5 km at 1 km depth. The fault zone has a complex distribution of shear and volumetric strain. Density, seismic velocities and reflectivities are conditioned by the volumetric strain of the DEM. Seismic imaging shows a response from the fault zone. Enhancing this part of the image is a challenge in acquisition and processing. Our approach can be extended to 3D. Future research will involve denser particles assemblages (smaller particles), and new techniques to pick much of the energy from the fault zone.

Introduction

Faults play a major role in controlling fluid flow in reservoirs. Faults are usually interpreted as 2D planar surfaces, but in reality they are zones of deformed rock with complex 3D geometry and internal structure. This internal structure determines fault-sealing capacity over geologic and production time scales (Faulkner et al., 2010 and associated papers). However, despite the importance of faults, there is a lack of truly quantitative data on fault zone internal structure (Manzocchi et al., 2010). Outcrops give only limited 2D views of faults. Seismic is limited by its resolution, as well as by poor image quality resulting from energy scattering in the fault zone (Townsend et al., 1998). Well core data are exceptional. In this paper, we propose an integrated approach to study fault zones and their impact on reservoir properties and seismic imaging. Fault zones are simulated with the discrete element method (DEM), and the finite strain of these models is used to condition seismic properties. Modelling of seismic images of the DEM analogues is then undertaken. This workflow allows us to study fault zone structure and the acquisition and processing challenges involved in imaging fault zones. It also provides guidelines for a better use of seismic and its attributes to depict fault zones.

Methodology

There are three main steps in our workflow: DEM modelling, conditioning of seismic properties, and seismic imaging.

- *DEM modelling:*

A realistic geomechanical model of faulting should include fault initiation, propagation, and linkage under any particular tectonic/stress regime. The model should be able to capture the extent of damage zone and the transition from faulting to folding. The DEM we use is a variant of the lattice solid model of Mora and Place (1993). The technique simulates the sedimentary rocks as an assemblage of spherical particles that obey Newton's equations of motion and that interact with elastic and frictional forces under gravity (Hardy et al., 2009). The method is capable of realistically and naturally model large deformations, fracturing, and fault development without complex re-meshing or/and internal boundary conditions (Hardy and Finch, 2006).

- *Conditioning of seismic properties:*

The DEM provides particle positions and velocity vectors at different time steps of the deformation. These can be used to invert for the strain tensor (Cardozo and Allmendinger, 2009). Strain parameters such as shear or volumetric strain can be used to condition the distribution of rock properties, including density and seismic velocities. There are several relations to compute seismic velocities from parameters such as density, porosity and fluid content. However, these apply only to the elastic regime. In fault zones, we are confronted to large and permanent deformations, with non-linear material response and no simple stress-strain relation (Couples et al., 2007). There are few studies about the impact of large, permanent strains on seismic properties; at laboratory (Holt et al., 2008), outcrop (Sigernes, 2004), or field reservoir (Hatchell et al., 2005) scales. These studies highlight the importance of two processes: i. Compaction, which reduces pore space, increasing density and wave velocity, and ii. Fracturing, which increases pore space, decreasing density and wave velocity. Particles in the DEM are much larger than grains, however, and strains from the DEM are broad averages of the deformation at the grain level. As a starting point and as a way to test our methodology, we assume that density (ρ) and P-wave velocity (V_p) are only modified by volumetric strain (ε_v) from the DEM, according to the following relations (Fig. 2a):

$$\begin{aligned} \phi &= \phi_{ini}\,(0.25\varepsilon_v + 1), \qquad -1 \le \varepsilon_v \le 1 \\ \rho &= \rho_g\,(1-\phi) + \rho_w\phi \end{aligned} \tag{1}$$

for density, where ϕ is porosity, ϕ_{ini} is porosity before faulting, and ρ_g, ρ_w are grain and fluid densities respectively; and:

$$V_p = \begin{cases} V_{p_{ini}}\,(-0.25\varepsilon_v^2 - 0.5\varepsilon_v + 1), & -1 \le \varepsilon_v < 0 \quad (contraction), \\ V_{p_{ini}}\,(0.25\varepsilon_v^2 - 0.5\varepsilon_v + 1), & 0 \le \varepsilon_v \le 1 \quad (dilation) \end{cases} \tag{2}$$

for P-wave velocity, where $V_{p_{ini}}$ is P-wave velocity before faulting. Sigernes (2004) shows that S-wave velocity (V_s) can be reasonably computed from V_p using Han's empirical law:

$$V_s = 0.794V_p - 0.787 \qquad (3)$$

- *Seismic imaging:*

Seismic modelling is used here to assess the impact of fault zone internal structure on the resulting seismic images. The technique we apply is a prestack depth migration (PSDM) simulator (Lecomte, 2008). This modelling of seismic volumes stems from a ray-based calculation of Point Spread Functions (PSFs), which are PSDM responses of point scatterers. The technique can be thought as a 3D spatial convolution of a reflectivity cube with such PSFs. This somehow resembles the industry-standard 1D convolution trace modelling. However, as opposed to the latter, the PSDM simulator works for prestack and depth, and handles properly 3D effects in resolution and illumination as function of various parameters (e.g., velocity model, survey geometry, wavelet, etc.). Simulated PSDM cubes are thus generated directly, i.e., without calculating synthetic recordings and processing them, in a fast (FFT-based) and robust manner allowing various sensitivity analyses.

Example

Results are given for a 2D DEM model with 45,000 particles and initial dimensions 1250 x 550 m (Fig. 1). The model has two shale layers interbedded in sandstone (Fig. 1a). A stress of 25 MPa corresponding to 1 km of sedimentary overburden is applied at the top. At the center of the base, a displacement boundary condition corresponding to a 60° dipping normal fault is applied. There is only friction (no bonding) between the particles, and the particles friction in the shale is about half the particles friction in the sandstone. This makes the shale weaker than the sandstone. The overall mechanical behavior of the layers is similar to average sandstone and shale, scaled for a km size rock mass. Fig. 1a shows the layers geometry after 60 m of normal fault displacement. A narrow fault zone at the base of the model widens upwards to a larger fault zone delimited by two faults. The steeper, larger fault forms at an early stage (10 m of displacement), while the gentler fault nucleates from the steeper fault at a later stage (40 m of displacement). Shear strain (Fig. 1b) shows that the fault is a complex area of deformation. Moreover, the fault zone is at some localities under high contraction, and at others under high dilation (Fig. 1c). The highest dilation regions correlate with the highest shear strains.

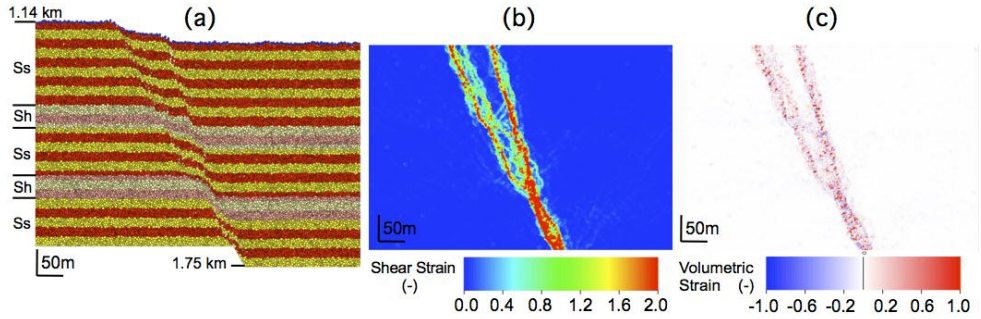

Figure 1: *Discrete element model after 60m of normal fault displacement.* ***a****. Layers geometry. Sh = Shale and Ss = Sandstone.* ***b****. Shear strain.* ***c.*** *Volumetric strain. Blue is contraction and red dilation. Strain was computed in 2x2m cells using a nearest neighbour algorithm with 6 particles neighbours and maximum radius 10m (Cardozo and Allmendinger, 2009).*

Seismic velocities and density in the model were computed using Eqs. 1 to 3 (Fig. 2a), assuming ϕ_{ini} and $V_{p_{ini}}$ of 0.15 and 4 km/s for the sandstone, and 0.3 and 2 km/s for the shale. Grain densities are 2650 and 2700 kg/m^3 for the sandstone and shale respectively, and both the sandstone and shale are water saturated. Figs. 2b and 2c show the resultant density and *Vp-Vs* fields. Low density and low *Vp-Vs* are associated with areas of high dilation (particularly in the shales), and high density and high *Vp-Vs* with areas of high contraction (particularly in the sandstones).

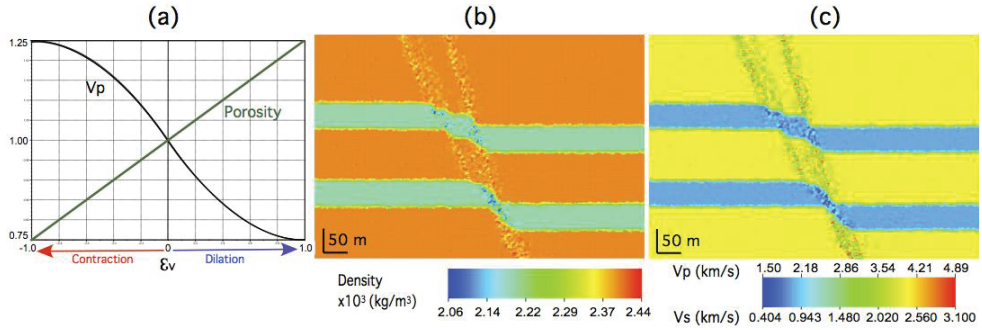

Figure 2: ***a****. Relations used to compute porosity (green) and Vp (black) as function of volumetric strain. The ordinate is given as a factor of the initial Vp or initial porosity.* ***b****. Density.* ***c****. Vp and Vs after 60 m of normal fault displacement.*

The density and seismic velocity fields of Fig. 2 were used to generate a reflectivity model (Fig. 3a). The PSDM simulator was then applied for a 40-Hz Ricker pulse and two types of illuminations (Figs. 3b and 3c), the latter being related to differences in, e.g., survey geometry, background velocity model, wave type, etc. (see Lecomte, 2008). Illumination patterns are obtained by ray tracing in both cases: the so-called specular illumination in Fig. 3b was designed for the flattish parts of the reflectors, while the "off-side" one in Fig. 3c does not contain specular energy for the same reflector parts (this may happen in, e.g., subsalt imaging). As a result, the flat reflectors dominate the simulated seismic image in Fig. 3b, though some related fault-structure seismic energy is visible. On the other side, the seismic image in Fig. 3c shows nearly only energy back-scattered at the fault zone. This indicates that tuning illumination might be a solution for better seismic imaging of the fault-zone, but such effects are strongly dependent on survey, reflectivity model, etc.

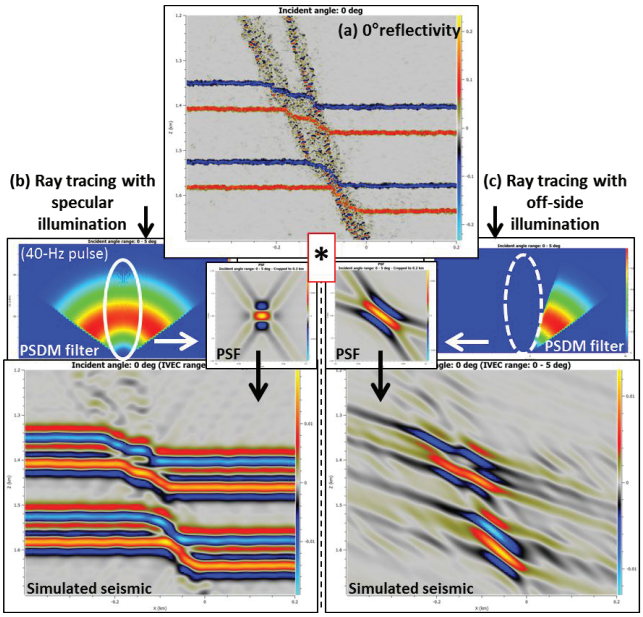

Figure 3: *Seismic modelling.* ***a****. Input reflectivity from DEM results.* ***b****. and* ***c****. PSDM simulator results for 2 illumination types, i.e., one containing specular energy for the flattish structures (b) and one without specular energy due to off-side illumination (c). The corresponding PSFs are given.*

Discussion and conclusion

We have shown a "proof of concept" of an integrated methodology to study the evolution of fault zones and their impact on seismic. The DEM allows us to study the effect on fault zone structure of geological parameters such as lithology contrast, stress fields (overburden), synsedimentation, and fault displacement. Seismic modelling (PSDM simulator) provides ways to evaluate the resulting seismic image, and the acquisition (e.g. wave frequencies, array geometry) and processing steps required to better image the fault zone. Future research on the geomechanical side will involve testing the effect of increasing the number of particles in the model (reducing particle size), and on the seismic modelling side devising techniques to get as much as possible the energy scattered from the fault zone. Once we understand well the 2D problem, we will move to 3D. Our current implementations of the DEM and PSDM simulator can do so. Establishing a link between the DEM and seismic modelling is one of the main challenges of our project. This is in essence a complicated rock physics problem for which there are not much data available. At present, we are using simplistic, empirical relations to attack this problem, and probably in the future we will have to do so. However, we argue that as long as we obtain realistic fault zone reflectivities (Fig. 3a) our assumptions are justified. It is not our intention to produce "exact" pictures of fault zones, but rather to implement a realistic geomechanical-geophysical framework to study fault zone structure and its impact on seismic.

References

Cardozo, N., and Allmendinger, R.W., [2009] SSPX: A program to compute strain from displacement/velocity data. *Computers and Geosciences* **35**, 1343-1357.

Couples, G., Ma, J., Lewis, H., Olden, P., Quijano, J., Fasae, T., and Maguire, R., [2007] Geomechanic of faults: impacts on seismic imaging. *First Break* **25**, 83-90.

Faulkner, D.R., Jackson, C.A.L, Lunn, R.J. et al. [2010] A review of recent developments concerning the structure, mechanics and fluid flow properties of fault zones. *Journal of Structural Geology* **32**, 1557-1575.

Hardy, S. and Finch, E. [2006] Discrete element modelling of the influence of cover strength on basement-involved fault-propagation folding. *Tectonophysics* **415**, 225-238.

Hardy, S., McClay, K.R., Muñoz, J.A., [2009] Deformation and fault activity in space and time in high-resolution numerical models of doubly-vergent thrust wedges. *Marine and Petroleum Geology*, **26**, 232-248.

Hatchell, P. and S. Bourne, [2005] Rocks under strain: Strain-induced time-lapse time shifts are observed for depleting reservoir. *The Leading Edge*, **24**(12), 1222–1225.

Holt, R. M., E. Fjær, O.-M. Nes, and J. F. Stenebråten, [2008] Strain sensitivity of wave velocities in sediments and sedimentary rocks, 42nd U.S. Rock Mechanics Symposium, *American Rock Mechanics Association Paper* No.ARMA08–291.

Lecomte, I., [2008], Resolution and illumination analyses in PSDM: A ray-based approach. *The Leading Edge*, **27,** 650-663.

Manzocchi, T., Childs, C., and Walsh, J.J., [2010], Faults and fault properties in hydrocarbon flow models. *Geofluids*, **10**, 94–113.

Mora, P., Place, D., [1993] A lattice solid model for the non-linear dynamics of earthquakes. *International Journal of Modern Physics*, **4**, 1059-1074.

Sigernes, Lill-Tove. [2004] Rock Physics of extensional faults and their seismic imaging properties. Doctoral thesis, monograph. *Norwegian University of Science and Technology,* 305 p.

Townsend, C., Firth, I.R., Westerman, R., Kirkevollen, L., Harde, M. and Andersen, T. [1998] Small seismic-scale fault identification and mapping. In: Jones, G., Fisher, Q.J. and Knipe, R.J. (Eds) Faulting, Fault Sealing and Fluid Flow in Hydrocarbon Reservoirs. *Geological Society of London, Special Publications* **147**, 1-25.

Appendix 3

Extended abstract 2:

Botter, Charlotte; Cardozo, Nestor; Hardy, Stuart; Lecomte, Isabelle; Escalona, Alejandro; Cooke, Nicholas & Paton, Gaynor

From Geomechanical Modelling to Seismic Imaging of 3D Faults.

Conference proceedings.

76th EAGE Conference & Exhibition. *EAGE **2014***

DOI: 10.3997/2214-4609.20141072
ISBN: 978-90-73834-89-7.

Accepted for oral presentation

A3

Amsterdam '14

We E104 09

From Geomechanical Modelling to Seismic Imaging of 3D Faults

C. Botter* (University of Stavanger), N. Cardozo (University of Stavanger), S. Hardy (ICREA), I. Lecomte (NORSAR), A. Escalona (University of Stavanger), N. Cooke (FFA) & G. Paton (FFA)

SUMMARY

Faults are 3D narrow zones of highly and heterogenously strained rocks, with petrophysical properties differing from the host rock, and are primary controls on fluid flow in reservoirs. We present a synthetic workflow to assess the potential of seismic data for imaging fault structure and internal properties. The workflow is based on a discrete element model (DEM) of faulting, simple relations to modify the seismic properties based on volumetric strain, and a ray-based modelling (pre-stack depth migration or PSDM simulator). Parameters such as wave frequency and their impact on the resulting seismic image are evaluated with the PSDM simulator. We illustrate the application of the workflow to a large displacement 3D normal fault in an interlayered sandstone-shale sequence in two mdoels, one with constant fault slip and the second with linearly variable fault slip along strike. DEM produces realistic fault geometries and strain fields. Seismic cubes at a high wave frequencies show the complexity of the faults, with reflectors offset and laterally affected. As the wave frequency decreases the fault traces become simplier. Seismic extracted fault geobodies make a direct link between the seismic, the DEM and the internal properties of the faults.

Introduction

Although typically interpreted as 2D surfaces, faults are 3D narrow zones of highly and heterogenously deformed rocks, with petrophysical properties differing from the host rock. 3D fault structure and properties are primary controls on fluid flow in faulted reservoirs (Faulkner et al., 2010 and associated papers). Even though seismic data are one of the main ways of subsurface investigation, faults are often at the limit of seismic resolution. Few examples in the literature examine the potential of seismic data to elucidate the complexity of fault structure and properties in space and time (e.g. Townsend et al., 1998; Long and Imber, 2010). We propose a synthetic workflow to assess the potential of reflection seismic data for imaging fault structure and properties. The workflow is based on a discrete element model (DEM) of faulting, simple relations to modify the initial elastic properties of the model based on volumetric strain, and a ray-based simulator (pre-stack depth migration or PSDM simulator). This methodology already investigated in 2D (Botter et al., 2012) is here introduced for 3D normal faults models, e.g. one with constant fault slip and the second with linearly variable fault slip along strike. The study of the corresponding seismic cubes provides guidelines for a better use of seismic and its attributes to characterize fault zones.

Methodology

Our workflow is divided in three main steps, taking into account the complexity of fault development, the large finite strains resulting from faulting, and the final seismic investigation.

We use a discrete element method (DEM) to simulate the process of fault formation: from initiation through propagation including fault-related folding. The DEM is a variant of the lattice solid model of Mora and Place (1993). The sedimentary rocks are simulated as an assemblage of spherical particles obeying Newton's equations of motion and interacting with elastic and frictional forces under gravity (Hardy et al., 2009). The method is capable of realistically and naturally model large deformations, fracturing, and fault development.

Large displacement faults involve large and permanent strains where we cannot easily relate stress to strain or use standard, continuum rock physics equations to predict the change of rock properties. Using the few studies available on this subject (e.g. Holt et al., 2008, Skurtveit et al., 2013), the impact of compaction on seismic properties (i.e., reduction of volume that decreases porosity and increases P-wave velocity) is used in our methodology (Botter et al., 2012). The density (ρ) and P-wave velocity (Vp) are modified by volumetric strain (εv) calculated from the DEM, according to the curves presented in Figure 1b left, where density is computed from porosity ϕ. Shear wave velocity is directly related to the P-wave velocity using Han's relation (Botter et al., 2012).

Seismic modelling is used here to assess the impact of fault zone internal structure on the resulting seismic images. The technique applied is a prestack depth migration (PSDM) simulator (Lecomte, 2008), acting as an image-processing method by distorting the input reflectivity to reproduce the effects of seismic imaging in PSDM mode. As opposed to 1D convolution, the PSDM simulator works in the prestack domain and in depth, and properly handles 3D effects in resolution and illumination as function of various parameters such as velocity model, survey geometry, wavelet, etc., including lateral resolution effects such as those resulting from faults or other discontinuities (Lecomte, 2008). A ray-based method computes point spread functions (i.e., PSDM responses of point scatterers), which are then convolved with the initial reflectivity cubes. Simulated PSDM cubes are generated without calculating synthetic recordings and processing them, in a fast (FFT-based) and robust manner.

Example of 3D normal faulting

Results are presented for a 3D DEM model of a normal fault. The model is composed of 180,000 particles with radii average of 10m for an interbedded sedimentary sequence of shales and sandstones, with initial dimensions of (x (east), y (north), z (up)) = (1450, 1450, 450) m (Figure 1a), and a stress at the top of 25 MPa corresponding to an overburden of 1.5 km. An initial boundary displacement

condition is set in the middle of the model corresponding to a 65° dipping normal fault with constant displacement along the strike through the entire model. A calibration phase ensures that the shale layers correspond to more ductile material than the sandstone. Figure 1a shows the model geometry, shear and volumetric strain, for one cross section perpendicular to strike at y = 750 m after 100 m of fault displacement. The fault dips in average 70° and its lateral extent is from 200 to 300 m. Higher shear strain is located at the bottom of the model (Figure 1a centre) and, overall, volumetric strain (Figure 1a right) shows more dilation than compaction in the fault zone.

Initial elastic properties are set in the initial non-faulted model, assuming ϕ_{ini} and Vp_{ini} of 0.15 and 4 km/s for the sandstone, and 0.3 and 2 km/s for the shale; grain densities of 2650 and 2700 kg/m^3 for the sandstone and shale respectively; and full water saturation for both the sandstone and shale. The changes of acoustic properties after deformation are computed through the relations of Figure 1b left, and the results are displayed in Figure 1b centre and right. The shale shows more compaction than the sandstone layers as well as relatively less changes in velocities.

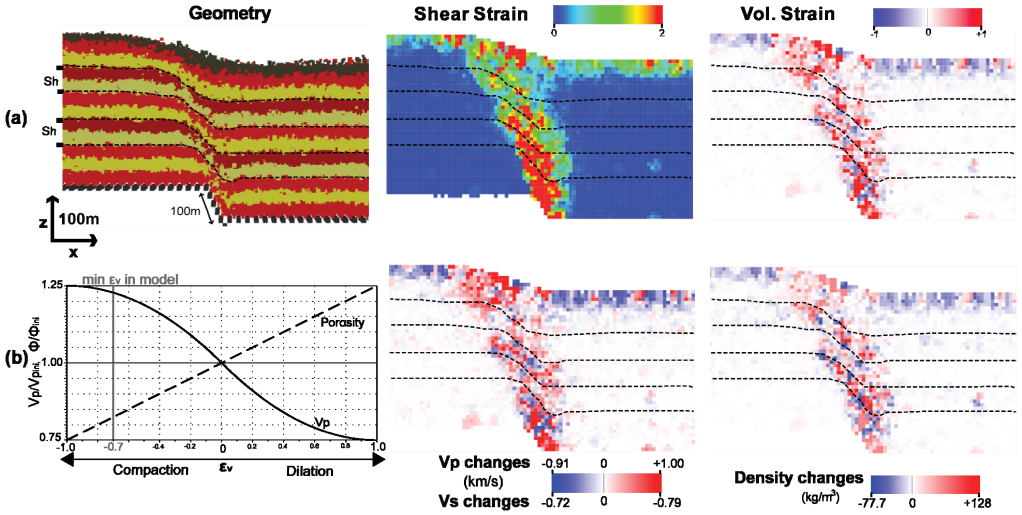

Figure 1 *Cross section at y= 750 m of the constant fault displacement model after 100m of fault displacement. (a) From the left to the right: the geometry (Ss: sandstone and Sh: shale), shear strain and volumetric strain of the model. (b) From left to right: Relations used to modify the initial properties P-wave velocities (Vp_{ini}) and porosity (ϕ_{ini}) to the final values of P-wave velocity (Vp) and porosity (ϕ) according to volumetric strain; resulting P- and shear-wave velocity changes; and density changes.*

These elastic cubes (i.e., density, P- and shear-wave velocities) are used to compute a reflectivity grid with a 0° incidence angle, and forward seismic modelling is applied for a homogeneous overburden and Ricker pulses going from 10 to 40 Hz. The cross section at y = 750 m at a frequency of 40 Hz (Figure 2a right) shows the large impact of the fault on the reflectors. They are displaced by the main fault slip surface, as well as distorted laterally by the 200 m extent of the fault. Fault associated diffractions are also visible. The fault complexity is captured by the map view (Figure 2b), where the center of the fault zone is not continuous and the visible reflection shows that sandstone and shale reflectors are part of the total extent of the fault. As the frequency wave decreases, the fault is displayed as a simpler structure (almost planar), which can lead to a wrong interpretation (Figure 2).

A more quantitative analysis of the seismic is the extraction of the fault damage zone geobody (i.e., total volume of reflection impacted by the fault). This can be extracted by analyzing the variation in signal around the fault, in particular characteristics such as dip (which indicates drag), chaos (which can highlight areas of damage) and amplitude. A direct comparison between the fault zone identified on the seismic and the fault volume in the initial geomechanical model is then possible and gives guidelines on how to better deal with the seismic for the fault interpretation.

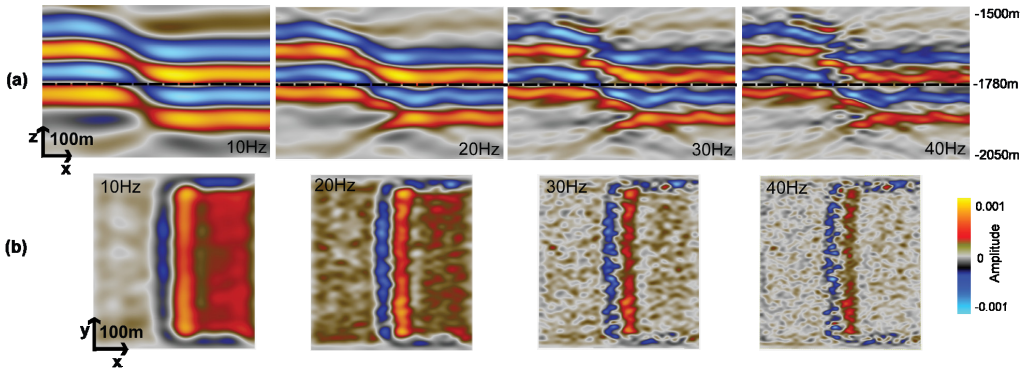

Figure 2 *Seismic sections of the constant slip model at several frequencies: (a) cross sections at y = 750m and (b) map view at z = -1780m. The dashed lines in a indicate the z sections.*

Example of 3D normal fault with variable displacement along the strike

The second fault model has the same initial settings than the first one, with the only difference that the fault displacement increases linearly to the north along fault strike. The boundary displacement conditions give a fault with displacement 0 m at y = 0 m and 140 m at y = 1450 m, with linear increase along y (Figure 3a). Finite strain (Figure 3b) suggests a fault dipping steeper during its early formation (y = 300 and 750 m) than during its late propagation (y = 1200 m). With 20 m of fault displacement (Figure 3, y = 300 m), there is little fault-related strain and even some antithetic faulting due to the boundary conditions at the bottom.

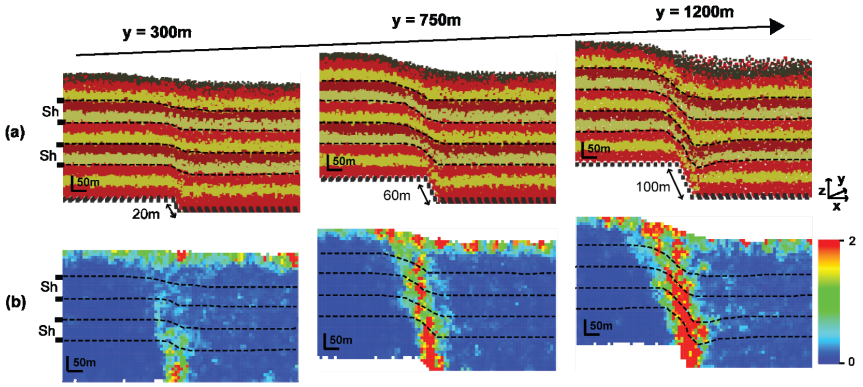

Figure 3 *Cross sections through the linearly increasing fault slip model at several values of y. (a) Geometry, (b) Shear strain.*

The forward seismic modelling was done under the same conditions and the resulting synthetic seismic is displayed for a Ricker pulse of 40 Hz in Figure 4. The fault is visible at y = 750 and 1200 m (Figure 4a), with fault-related diffractions at y = 1200 m. At 20 m fault displacement (y = 300 m), the shale reflectors are folded with less impact at the top of the model. The map views (Figure 4b) present the lateral limits of the fault zone, especially at the bottom (z = -1930 m) where the impact of the fault increases towards the north (high values of y). Upper map views (z = -1780 and -1630 m) show that the traces of the shale reflector are slightly curved, suggesting an increase of the fault impact towards the north. The approximate location of the tip of the fault can be found in all the map views. Further quantitative interpretation (i.e. seismic attributes analysis) helps to associate the fault volume extracted from the seismic with that of the DEM model.

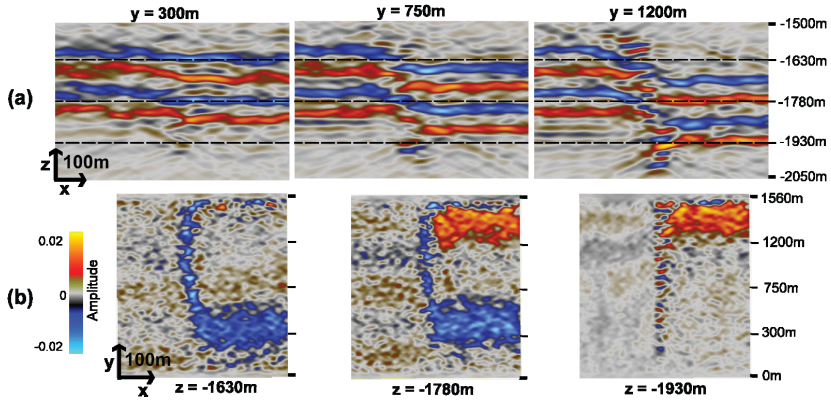

Figure 4 *Seismic sections through the variable slip model for a Ricker pulse of 40Hz (a) at several values of y and (b) at several values of depth z. The dashed lines in a indicate the z sections.*

Conclusions

The integrated methodology presented here is a new step in the study of faults in 3D and their impact on seismic. The geomechanical modelling allows understanding of fault formation under several geological parameters such as overburden, lithology contrasts, fault geometry, etc. Particle size is restricted due to computation limitations. Even though the changes of seismic properties due to faulting are at an early stage of investigation, the results are accurate enough to have a realistic impact on the seismic. The 3D seismic modelling provides ways to investigate several parameters such as wave frequency, geometry survey, or overburden on the resulting seismic image, and processing steps required to better image the fault zone. Future work will involve smaller particles, along-strike propagating-fault models, including interacting faults that form relay ramps; as well as seismic imaging of an outcrop with mapped fault deformation.

References

Botter, C., Cardozo, N., Hardy, S., Lecomte, I. and Escalona, A. [2012] Mechanical Modelling and Seismic Imaging of Fault Zones. Extended Abstract, *3rd International Conference on Fault and Top Seals – From Characterization to Modelling*, Montpellier.

Faulkner, D.R., Jackson, C.A.L., Lunn, R.J. *et al*. [2010] A review of recent developments concerning the structure, mechanics and fluid flow properties of fault zones. *Journal of Structural Geology*, **32**, 1557-1575.

Hardy, S., McClay, K.R. and Muñoz, J.A. [2009] Deformation and fault activity in space and time in high-resolution numerical models of doubly-vergent thrust wedges. *Marine and Petroleum Geology*, **26**, 232-248.

Lecomte, I. [2008] Resolution and illumination analyses in PSDM: A ray-based approach. *The Leading Edge*, **27**, 650-663.

Long, J.J. and Imber, J. [2011] Geological controls on fault relay zone scaling. *Journal of Structural Geology*, **33**(12), 1790-1800.

Mora, P. and Place, D. [1993] A lattice solid model for the non-linear dynamics of earthquakes. *International Journal of Modern Physics*, **4**, 1059-1074.

Skurtveit, E., Torabi, A., Gabrielsen, R.H. and Zoback, M.D. [2013] Experimental investigation of deformation mechanisms during shear-enhanced compaction in poorly lithified sandstone and sand. *Journal of Geophysical Research: Solid Earth*, **118**(8), 4083-4100.

Townsend, C., Firth, I.R., Westerman, R., Kirkevollen, L., Harde, M. and Andersen, T. [1998] Small seismic-scale fault identification and mapping. In: Jones, G., Fisher, Q.J. and Knipe, R.J. (Eds) Faulting, Fault Sealing and Fluid Flow in Hydrocarbon Reservoirs. *Geological Society of London, Special Publications*, **147**, 1-25.

Appendix 4

Extended abstract 3:

Botter, Charlotte; Cardozo, Nestor; Lecomte, Isabelle; Rotevatn, Atle & Paton, Gaynor

The effect of fluid flow in relay ramps on seismic images.

*EAGE Fault and Top Seals Conference, Almerìa **2015***
2015/09/20 -24.

DOI: 10.3997/2214-4609.201414048
ISBN: 9781510814172

Accepted for oral presentation

Received Award for Best Young Presenter

A4

Fault and Top Seals
Almería 2015

Mo FTS 05

The Effect of Fluid Flow in Relay Ramps on Seismic Images

C. Botter* (University of Stavanger), N. Cardozo (University of Stavanger), I. Lecomte (NORSAR), A. Rotevatn (University of Bergen) & G. Paton (ffA)

SUMMARY

Using an integrated workflow from an outcrop model in the Arches National Park, Utah, fluid flow simulation to seismic modelling, we intend to study the impact of a relay ramp system and its fluid composition on seismic images. Faulting in porous sandstone is associated to deformation bands that decrease the porosity and permeability locally. Based on those modified petrophysical properties, we run a fluid flow simulation and a ray-based pre-stack depth migration (PSDM) simulation to evaluate the impact of parameters such as illumination or wave frequency. We study the relay ramp at two stages of the fluid flow simulation: at the beginning and at the end. Only the changes in porosity around the faults are visible at the beginning, while fluid contacts affect also the model at the end. Resultant seismic images are able to show reflection and diffraction for the two faults when constant fluid saturation at the beginning. However, the thin layer of water at the top of model has a much stronger impact at the end and the faults can hardly be interpreted. Our methodology provides ways to better understand how faulting impact seismic, and therefore to tune acquisition and processing parameters for fault characterization.

Introduction

Soft-linked relay ramps have been studied to be controls on fluid flow in producing hydrocarbon reservoirs. At reservoir production scale, several properties within the fault system evolve especially the fluid saturations and pressures. Those variations can be monitored through time using well testing. The change of fluid contacts can also be visible when doing 4D seismic, by comparing a seismic data set at the beginning of the production to a newest one at the end. In order to study the impact of a relay ramp structure and its fluid composition on seismic data, we propose the use of a workflow where we combine flow simulation in a geomodel of an outcrop relay ramp and forward seismic modelling at several stages of the simulation. We use a field analogue model in where, after defining rock properties as porosity and permeability (Rotevatn et al., 2007), we run a flow simulation (Rotevatn et al., 2007 and 2009). The flow simulation results are then used as input for seismic modelling using a ray-based based prestack depth-migration (PSDM) simulator (Lecomte, 2008). The analogue is a relay ramp system from a well-exposed outcrop in Arches National Park, Utah. The structural and flow studies of this porous sandstone have been presented in Rotevatn et al. (2007) and (2009) respectively. This faulting process in porous rock is associated with strain localised features or deformation bands (Aydin, 1978) that reduce the porosity of the rock (e.g. Antonellini et al., 1994) and affect the permeability (Rotevatn et al., 2007 and references therein). The study of the seismic cubes at the beginning and at the end of a flow simulation provides information on how to investigate and characterise the impact of porosity reduction and water saturation in relay ramp system on seismic data.

Methodology

Our workflow is divided in several steps, taking into account the architecture and property definition of relay ramp system, fluid flow simulation and seismic investigation.
We use the well detailed geomodel of the Delicate Arch Ramp in Utah made by Rotevatn et al. (2009). Initial host rock properties of the sandstone are based on measurements from Antonellini and Aydin (1994): porosity 28%, horizontal permeability 1000mD and vertical permeability 100mD (Rotevatn et al., 2009). Based on the frequency of deformation bands within each cell of the geomodel (Rotevatn et al., 2009), these petrophysical properties are modified due to faulting, as following:

- Deformation bands are estimated to have really low porosity at their centre of 0.01% (Antonellini and Aydin, 1994). The porosity $\emptyset$ in a cell is then computed as an arithmetic average based on the volume of deformation bands and host sandstone: $\emptyset = \frac{V_{Ss}.\emptyset_{ss}+V_{DBs}.\emptyset_{DB}}{V_{total}}$
  With V_{Ss} the volume of sandstone in one cell, $\emptyset_{ss}$ the porosity of sandstone, V_{DBs} the volume of deformation bands in one cell, $\emptyset_{DB}$ the porosity of deformation bands and V_{total} the volume of one cell.
- The horizontal permeability is modified in x and y grid direction according to the relationships of Rotevatn et al. (2007 and 2009) for a median case corresponding to a permeability of 0.01mD for deformation bands.

Fluid flow simulation based on these properties is run with an injector well placed on the lowest part of the relay ramp and a producer well at the highest part. Fault transmissibility is kept constant through the simulation.
Seismic modelling is used here to assess the impact of relay ramp structure and properties and fluid saturations on the resulting seismic images. The technique applied is a PSDM simulator (Lecomte, 2008), acting as an image-processing method by distorting the input reflectivity to reproduce the effects of seismic imaging in PSDM mode. As opposed to 1D convolution, the PSDM simulator works in the prestack domain and in depth, and properly handles 3D effects in resolution and illumination as function of various parameters such as velocity model, survey geometry, wavelet, etc., including diffraction effects such as those resulting from faults or other discontinuities (Lecomte, 2008; Botter et al., 2014 a and b). A ray-based method computes point spread functions (PSFs, i.e., PSDM responses of point scatterers), which are then convolved with the initial reflectivity cubes. Simulated PSDM cubes are generated without calculating synthetic recordings and processing them, in a fast (FFT-based) and robust manner.

Example: application to Delicate Arch Ramp

The porosity based on deformation band frequency is presented in Figure 1a. We see a decrease of the porosity up to 11.5% in the model, following the close surrounding of the two soft linked faults. The presence of deformation bands ahead of the North fault impacts also the porosity even if there is no fault throw. The permeability changes for the Y direction are also displayed in Figure 1b. The permeability is more drastically impacted by deformation bands than the porosity. Fluid flow simulation for oil and water saturation is run for 12 years based on the porosity and permeability values in the model. Results are presented in Figure 1c one year after the beginning of the simulation and in Figure 1d at the end of 12 years of simulation. The water invades the model following the ramp elevation, by moving the remaining oil in direction of the producer well. Oil in the areas next to the higher throws of the faults is not efficiently produced.

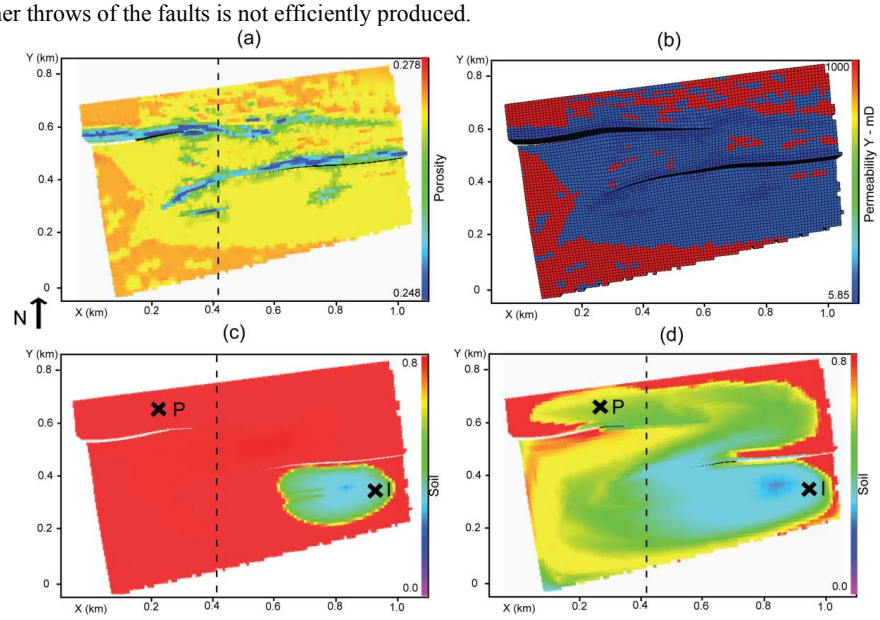

Figure 1 *3D model of the Delicate Arch (Utah) with following properties (a) Porosity calculated from deformation bands frequency, (b) Permeability in Y direction calculated from deformation bands frequency (c) Oil saturation one year after the beginning of the flow simulation and (d) Oil saturation at the end of the flow simulation (after 12 years). Producer and injector wells are displayed (P and I respectively).*

Using the porosity values of Figure 1a and the water saturation of the flow simulation results, we can compute elastic parameters based on Gassmann relations in order to obtain density, velocities and reflectivity cubes. The reflectivity grid with a 0˚ incident angle is used as an input for the PSDM simulations. We present the results of the seismic modelling at the beginning of the flow simulation and at the end in Figure 2. The impacts of oil saturation (Figure 2a) and of the P-wave velocity (Figure 2b) are used to compute the reflectivity grids (Figure 2c). The beginning case shows mostly the impact of deformation bands on the model, so stronger reflectivity values next to the faults and very few data away. The finale case is strongly impacted by the fluid saturations in the model, with higher impact next to the faults.
The model is brought at 2.0 km under the sea level. PSDM simulations are run for two types of survey illumination, one with up to 90˚ dip corresponding to a perfect survey (hence only resolution effects left), at a wave-frequency of 40Hz (Figure 2d), and one with up to 45˚ dip illuminating mostly the flat layers and parts of the non-flat structures, this for two wave frequencies, 40Hz (Figure 2e) and 20Hz (Figure 2f).

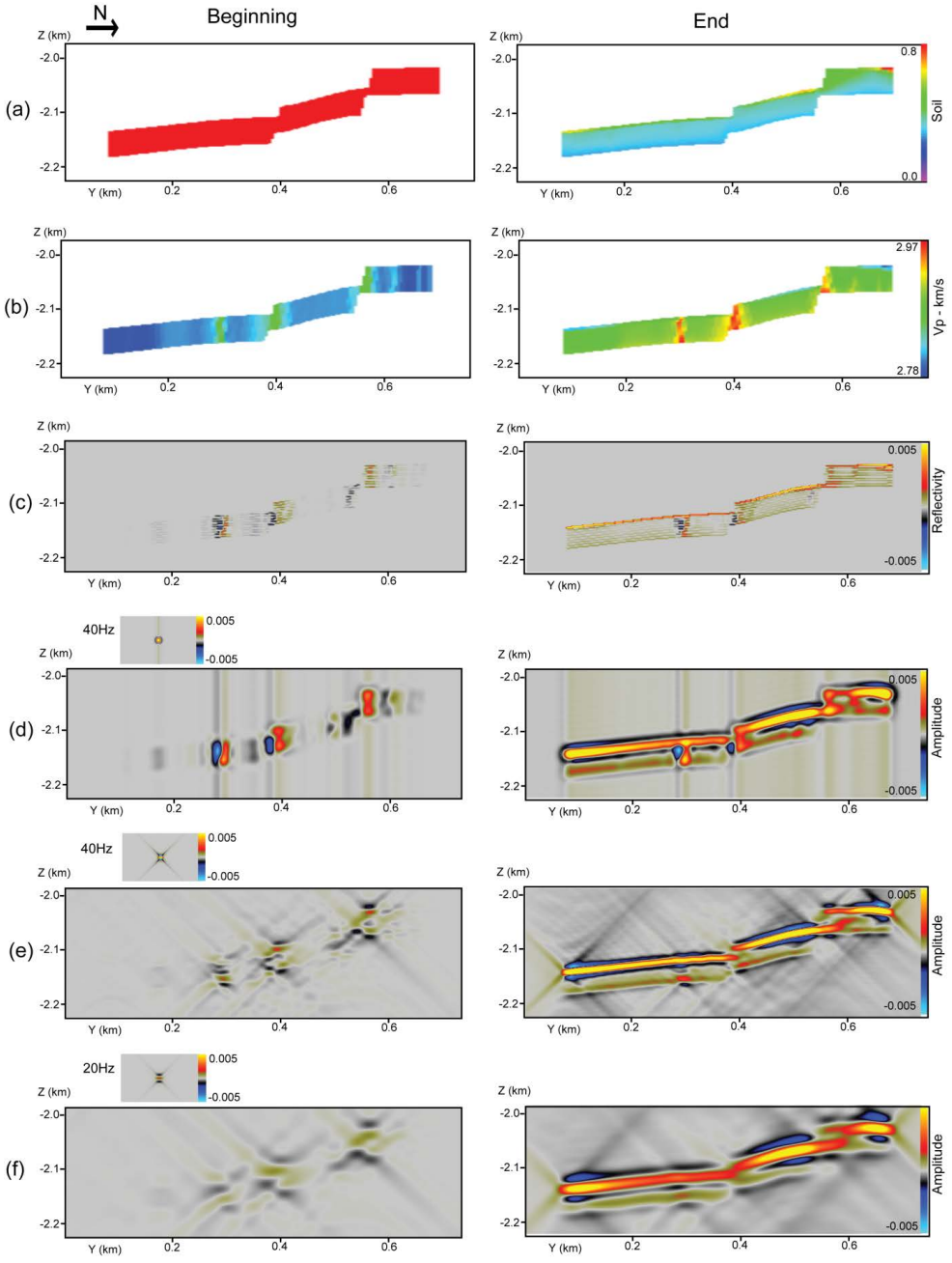

Figure 2 *Cross sections at X=415m in the model at one year after the beginning (left column) and at the end of the flow simulation for comparing the following data: (a) Oil Saturation, (b) P-wave velocity, (c) Reflectivity, (d) Seismic images corresponding to up-to 90˚ illumination (PSDM filter on the left and corresponding PSF on the right) with a 40Hz Ricker pulse, (e) Seismic images corresponding to a 45˚ analytical filter with 40Hz Ricker pulse, and (f) Seismic images corresponding to a 45˚ analytical filter with a 20Hz Ricker pulse.*

At the beginning of the flow simulation, only the areas next to the faults are visible. At 40Hz, the 90˚ dip analytic filter illuminates the footwall and hanging wall sides of the two faults, while the 45˚ dip analytic filter creates mainly diffraction for these vertical features. The 45˚ dip analytic filter at 20Hz shows also diffraction but with lower amplitude which makes the faults harder to locate and to interpret. At the end of the simulation, the thin layer of water at the top of the model is the most visible on all seismic images. The 90˚ dip analytic filter shows a perfect illumination of both the water layer and the fault throws, while the 45˚ dip analytic filters illuminates mainly the top reflector corresponding to the water layer. The faults are still visible due to diffraction at 40Hz, especially the northern one. At 20Hz, the faults are almost not identifiable even if still some fault related diffraction is visible. More advanced attribute-based interpretation techniques can be applied to the seismic images in order to better interpret the fault structures and fluid contacts.

Conclusions

The workflow presented here is a new step in the study of the impact of relay ramp systems and their fluid saturations on seismic data. Many parameters can be controlled and adjusted all along the methodology, starting by the porosity and permeability values. The fluid composition and the flow simulation influence the finale water saturation. Even if those values do not show high contrast of values (as would different lithology), the differences are still visible on the finale seismic images with low range of amplitude values. The PSDM simulator is applied for evaluating the acquisition and processing parameters required to better image the fault zone. Two parameters are investigated here, the illumination and the wave frequency. Showing first an illumination from a perfect survey highlights the area of the models we need to focus on. Using a more restrictive analytic filter at two wave frequencies shows that the faults in sandstone with low property variations have much less impact on amplitude values than the fluids contact. Additional analyses and characterisation of the seismic image will give us information on how to handle seismic data for specific fault characterisation with varying properties. This integrated methodology gives also unique insights for 4D seismic applications.

References

Antonellini, M. and Aydin, A. [1994] Effect of faulting on fluid flow in porous sandstones: petrophysical properties. *American Association of Petroleum Geologists Bulletin* **78**(3), 355-377.

Antonellini, M. A., Aydin, A. and Pollard, D. D. [1994] Microstructure of deformation bands in porous sandstones at Arches National Park, Utah. *Journal of Structural Geology* 16(7), 941-959.

Aydin, A. [1978] Small faults formed as deformation bands in sandstone. *Pure and Applied Geophysics* PAGEOPH 116(4-5), 913-930.

Botter, C., Cardozo, N., Hardy, S., Lecomte, I. and Escalona, A. [2014a] From mechanical modeling to seismic imaging of faults: A synthetic workflow to study the impact of faults on seismic. *Marine and Petroleum Geology* 57(0), 187-207.

Botter, C., Cardozo, N., Hardy, S., Lecomte, I., Escalona, A., Cooke, N. and Paton, G. [2014b] From Geomechanical Modelling to Seismic Imaging of 3D Faults. *76th EAGE Conference and Exhibition 2014*.

Lecomte, I. [2008] Resolution and illumination analyses in PSDM: A ray-based approach. *Leading Edge* (Tulsa, OK) 27(5), 650-663.

Rotevatn, A., Fossen, H., Hesthammer, J., Aas, T. E. and Howell, J. A. [2007] Are relay ramps conduits for fluid flow? Structural analysis of a relay ramp in Arches National Park, Utah. *Special Publication-Geological Society Of London*, *270*, 55

Rotevatn, A., Tveranger, J., Howell, J. A. and Fossen, H. [2009] Dynamic investigation of the effect of a relay ramp on simulated fluid flow: Geocellular modelling of the Delicate Arch Ramp, Utah. *Petroleum Geoscience* 15(1), 45-58.